UNIVERSITY OF CALIFORNIA, SAN DIEGO

Physical controls on episodic nearshore phytoplankton blooms in Southern California

A dissertation submitted in partial satisfaction of the
requirements for the degree
Doctor of Philosophy

in

Oceanography

by

Melissa Margaret Omand

Committee in charge:

Peter J.S. Franks, Co-Chair
Falk Feddersen, Co-Chair
Robert T. Guza
Stefan G. Llewellyn-Smith
Clinton D. Winant

2011

The dissertation of Melissa Margaret Omand is approved, and it is acceptable in quality and form for publication on microfilm and electronically:

_____

_____

_____

_____
Co-Chair

_____
Co-Chair

University of California, San Diego

2011

TABLE OF CONTENTS

Signature Page iii

Table of Contents iv

List of Figures vii

List of Tables xvii

Acknowledgements xviii

Vita and Publications xix

Abstract xx

Chapter 1 The Influence of Bubbles and Sand on Chlorophyll-*a* Fluorescence Measurements in the Surfzone. 1

1.1 Abstract 1

1.2 Introduction 2

1.3 Materials and Procedures 4

1.3.1 ECOTriplet Fluorometer 4

1.3.2 Laboratory Methods 4

1.3.3 Chl a_{raw} field measurements 6

1.4 Assessent 6

1.5 Discussion 13

1.6 Comments and Recommendations 19

1.7 Appendix A: The effect of Rhodamine-WT dye on Chl a_{raw} . 21

1.8 Appendix B: The effect of backscattered ambient sunlight on Chl a_{raw} 21

1.9 Appendix C: Effect of bubbles on Chl a_{raw} from a single-channel fluorometer 23

1.10 Acknowledgements 25

Chapter 2 Physical and biological processes underlying the sudden surface appearance of a red tide in the nearshore. 26

2.1 Abstract 26

2.2 Introduction 27

2.3 Methods 29

2.3.1 Jetski Surface Maps 29
2.3.2 CTD+Chl *a* Casts 31
2.3.3 Moorings 32
2.3.4 Surfzone Frames 32
2.3.5 Water Samples 33
2.3.6 Nonphotochemical Quenching Correction 33
2.4 Results 34
2.4.1 Subsurface Red Tide Observations 34
2.4.2 Surface Red Tide Observations 37
2.5 Discussion 41
2.5.1 Stage 1: Shoreward Propagation of a Supertidal Internal Wave 41
2.5.2 Stage 2: Formation of the Intense Chl *a* Patch within an Internal Wave Trough 45
2.5.3 Stage 3: Internal Wave Breaking 48
2.5.4 Stage 4: Cross-Isotherm and Vertical Spreading of the Intense Subsurface Chl *a* Patch 50
2.5.5 Stage 5: A Density Barrier to Chl *a* Entry Into the Surfzone 52
2.5.6 Summary and Synthesis 55
2.6 Appendix: Corrections for Non-Photochemical Quenching (NPQ) 57
2.7 Acknowledgements 60

Chapter 3 Episodic vertical nutrient fluxes and nearshore phytoplankton blooms in Southern California 61
3.1 Abstract 61
3.2 Introduction 62
3.3 Methods 65
3.3.1 Moored observations 66
3.3.2 Intensive small boat-based sampling 68
3.4 Background Physical Observations 69
3.4.1 The NO_3-Temperature relationship 69
3.4.2 Moored observations at M18 70
3.5 Estimating the Vertical Nitrate Flux 72
3.5.1 Vertical NO_3 flux due to vertical advection 72
3.5.2 The Vertical Turbulent NO_3 Flux 74
3.5.3 Vertical advective and turbulent NO_3 flux and relationship to Chl *a* 82

3.6 A focused investigation of Bloom 3 83
3.6.1 Phytoplankton community and bloom composition . . 83
3.6.2 The NO_3-Chl$a$ Relationship 84
3.6.3 The relationship between NO_3, Silicate, and Phosphate in the Euphotic Zone 87
3.7 Vertical $NO_3 flux_{tot}$ Nitrate-Phytoplankton Modeling 91
3.7.1 Model defintion and model parameters: growth and mortality rates 91
3.7.2 NP model-data comparison 93
3.7.3 Modeling of individual blooms 96
3.8 Discussion 98
3.8.1 Inferring bloom composition variation from uptake parameters 98
3.8.2 Mortality rates 100
3.8.3 Other factors influencing phytoplankton blooms 102
3.9 Summary 103

LIST OF FIGURES

Figure 1.1: Schematic of the 3-channel (Chl a, turbidity, dye) WET Labs ECO Triplet and four potential mechanisms for Chl a error. The dashed box represents the sample volume, located a few centimeters from the 10 cm diameter sensor head. (a) Chl a_{raw} enhancement through scattering of the 660 nm turbidity excitation into the Chl a detection window (mechanism A), and (b) Chl a_{raw} suppression through scattering of the fluoresced 685 nm light away from the Chl a detection window (mechanism B). (c) Chl a_{raw} enhancement through detection of dye fluorescence as Chl a (mechanism C), and (d) Chl a_{raw} enhancement through ambient sunlight near 685 nm scattered into the Chl a detection window (mechanism D). The Chl a detection window wavelength range overlaps with the range of emitted τ (A) and dye-fluoresced light (D). 5

Figure 1.2: (a) Measured Chl a_{raw} and (b) bubble-induced turbidity τ versus time in fresh, Chl a-free water with no ambient light. Vertical gray bars indicate times without bubbles. 7

Figure 1.3: Chl a_{raw} versus turbidity (τ) (black points) and linear best fit (gray line) in Chl a-free freshwater with no ambient light with (a) bubble-induced τ (slope = 0.008 ± 0.001 $\mu\mathrm{g\,L^{-1}\,ntu^{-1}}$, $r^2 = 0.41$, $p < 0.001$), and (b) sand (slope = 0.0046 ± 0.0005 $\mu\mathrm{g\,L^{-1}\,ntu^{-1}}$, $r^2 = 0.64$, $p < 0.001$). Chl a_{raw} with τ emission blocked versus turbidity (black points) in fresh, Chl a-free water with no ambient light, and with (c) bubble-induced ($r^2 = 0.01$, $p = 0.24$), and (d) sand-induced ($r^2 = 0.002$, p=0.63) turbidity. 8

Figure 1.4: Chl a_{raw} (black) and bubble-induced turbidity (dark gray) versus time in seawater with Chl a_{true} = 10 $\mu\mathrm{g\,L^{-1}}$. Vertical gray bars indicate times without bubbles. 9

Figure 1.5: Chl a_{raw} versus turbidity (τ) in seawater with 5 known Chl a_{true} concentrations (black asterisks on vertical axis corresponding to 10, 7, 4, 1.5 and 0.2 $\mu g L^{-1}$) for (a) bubble-induced and (b) sand-induced τ. Solid lines are linear fits with intercept set equal to Chl a_{true}. The fraction of variance described by each fit (in ascending Chl a_{true} order) is r^2 = **0.48**, hi **0.45**, **0.05**, **0.22**, **0.52** (bubbles) and r^2 = **0.10**, 0.01, 0.01, **0.46**, **0.70** (sand). The r^2 in bold type correspond to $p < 0.001$. 10

Figure 1.6: Laboratory τChl a_{raw} regression slopes γ (from Fig. 5) versus Chl a_{true} for bubble (gray) and sand (black) tests. The solid lines are linear regression fits (eq. 3) with intercepts ($\alpha = 0.008 \pm 0.001 \mu g L^{-1} ntu^{-1}$ (bubbles) and $\alpha = 0.0046 \pm 0.0005 \mu g L^{-1} ntu^{-1}$ (sand)) determined from Chl a_{true} = 0 tests. The linear best fit slopes $\beta 1$ are -0.010 $\pm$ 0.003 ntu^{-1}, r^2=0.90, p = 0.01 (bubbles), and -0.0011 $\pm$ 0.0003 ntu^{-1}, r^2 = 0.59, p = 0.12 (sand). The gray dashed line represents the best quadratic fit for bubbles ($\beta 2$ = -0.001 $L \mu g^{-1} ntu^{-1}$) with intercept (α = 0.008 $\pm$ 0.001 $\mu g L^{-1} ntu^{-1}$) determined from Chl a_{true} = 0 tests. The black dot-dashed line at γ = 0 indicates the border between τ-induced enhancement ($\gamma > 0$) and suppression ($\gamma < 0$). 12

Figure 1.7: Chl a_{raw} versus turbidity (τ) within the surfzone for a single 3-h period. Each dot is a 4 sec observation. The gray points (Chl a_{nat}) are Chl a_{raw} with $\tau < 10$ ntu , and the median Chl a_{nat} (Chl $a_{m,nat}$) approximates Chl a_{true} for this period. The black dashed line is a linear best fit (slope ((γ) = 0.0086 $\mu g L^{-1}$ntu, r^2 = 0.29, $p < 0.001$). 14

Figure 1.8: Field-derived τChl a_{raw} regression slopes γ versus Chl $a_{m,nat}$(asterisks). The solid line is the least-squares fit, r^2 = 0.48 $p < 0.001$, slope (β field) = -0.004 $\pm$ 0.002 $\mu g L^{-1} ntu^{-1}$, intercept (α_{field}) = 0.017 $\mu g L^{-1}$. The gray shaded region indicates the laboratory γ range with linear fits (n = 1) to the bubbles and sand tests, and the gray dashed line indicates the quadratic fit to the bubbles laboratory test (see Fig. 6). The black dashed line at γ = 0 indicates the border where τ-induced enhancement ($\gamma > 0$) and suppression ($\gamma < 0$) are dominant. 16

Figure 1.9: (a) Turbidity τ, (b) $Depth_{bs}$, distance instrument is below mean sea surface (dashed line is 1 m), (c) significant wave height H_{sig}, (d) unprocessed Chl a_{raw} (e) surfzone Chl a_{raw} (de-spiked, observations within 1 m of the surface removed, black) and Chl a_{corr} (red), and (f) Chl a_{raw}/Chl a_{corr}; all versus time for 48 hrs. Gray (black) lines correspond to data seaward of (within) the surfzone. 17

Figure 1.10: Probability density function of (a) de-spiked Chl a_{raw} and (b) turbidity for all field data (∼500 h) inside (black line) and outside (gray line) the surfzone. 18

Figure 1.11: Predicted Chl a_{raw}/Chl a_{true} ratio with field-derived parameters (n = 1, α_{field} and β_{field}) for ECO Triplet fluorometers over a range of Chl a_{true} and τ values with τ enhancement (A) and without τ enhancement (B) due to emitted τ interference. The white boxes represent the ranges of 90% of Chl a_{raw} and τ measurements taken within the surfzone (SZ) and seaward of the surfzone (OS) during the field experiment. 19

Figure 1.12: Chl a_{raw} with Chl a_{true} = 0.6 $\mu g L^{-1}$ versus Rhodamine-WT dye concentration (gray points). The black line is the linear fit (slope = 0.13 $\pm$ 0.01 $\mu g L^{-1} ppb^{-1}$, $r^2 < 0.9$ $p < 0.001$). 22

Figure 1.13: WETStar Chl a_{raw} versus bubble-induced turbidity (τ) in seawater with 4 known Chl a_{true} concentrations (black asterisks on vertical axis corresponding to 10, 4, 1.5 and 0.2 $\mu g L^{-1}$). Solid lines are linear fits with intercept set equal to Chl a_{true}. The fraction of variance described by each fit (in ascending Chl a_{true} order) is r^2 = **0.77, 0.35, 0.44, 0.10 respectively. The r^2 in bold type correspond to $p < 0.001$.** 24

Figure 2.1: Un-retouched photograph of a brownish alongshore-parallel band of red tide (arrow) approximately 500 m offshore, taken from the beach in early afternoon on 12 October. The small breaking surface wave in the foreground is near the beach, and the 5 m long CTD+Chl a cast boat is offshore. 29

Figure 2.2: Schematic of HB06 instrumentation: (a) plan view of bathymetry contours vs. the alongshore (y) and cross-shore (x) coordinates and (b) cross-shore transect of bathymetry (dark shading). The vertical coordinate is z, with $z = 0$ m at the tidally averaged surface and positive upward. Moored temperature strings (circles, M8 to M27) were located at total depths $H = 8$, 15, 18, and 24 m. A vertically profiling CTD+Chl$a$ wirewalker (M13) was located at $H = 13$ m. Bottom-mounted ADCPs (stars) were located near moorings M8, M13, M15, and M18. Fixed frames within the surfzone (M1.5) at $H = 1.5$ m and seaward of the surfzone (M4) at $H = 4$ m measured Chl$a$ (triangles), T (circles), wave height, and currents (*see* inset in (b)). A GPS-tracked jetski measured surface T and Chl$a$ within the black dashed box in (a) and small boat (CTD+Chl$a$) completed transects during daylight hours from $H = 5$ to 60 m (8 km offshore). The Talbert Marsh outlet is located 1 km south of the instrument transect. 30

Figure 2.3: Gantt chart indicating velocity (gray), T (black) and Chl$a$ (green) data coverage between 05 October and 16 October. Stars indicate CTD+Chl$a$ transect days and circles indicate bottle samples for phytoplankton identification. 31

Figure 2.4: Cross-shore sections (x,z) of Chl$a$ (μg L^{-1}, colors) and T (°C, black contours) obtained between 09:00 and 11:30 h on select days between 05 October and 16 October. The red circle is M13 surface location and the white triangles indicate CTD+Chl$a$ cast locations. The white line traces the 4 μg L^{-1} Chl$a$ contour. The black box (in d) indicates the nearshore red tide focus area on 12 October. 35

Figure 2.5: Time series (spanning 54 h) at M13 ($H = 13$ m) of (a) tidal excursion from mean sea level, (b) vertical proles of 15 min averaged cross-shore currents u at M13 (positive = onshore), and (c) 15 min averaged vertical profiles of Chl$a$ (μg L^{-1}, colors) and T (°C, black contours) at M13. The white curves trace the 4 μg L^{-1} Chl$a$ contour. Time zero is 00:00 h 12 October. 38

Figure 2.6: Time series (spanning 11 h of the time period in Fig. 5) of 15 min averaged vertical profiles of Chl$a$ (μg L^{-1}, colors) and T (°C, black contours) at M13 ($H = 13$ m). Time 10 hours corresponds to 10:00 h on 12 October. The hourly averaged cross-shore currents (u) are represented by arrows for $—u— \geq 0.01$ m s^{-1}and by black dots where $—u— < 0.01$ m s^{-1}. The 15 min averages shown in Fig. 5 crowded the plot blocking the Chl$a$ colors. The white line is the 4 μg L^{-1}contour. . . . 39

Figure 2.7: Sequential (top to bottom) maps of nearshore Chl a (left) and T (right) on 12 October from jetski-based horizontal (x,y) measurements and CTD+Chl a based cross-shore transect (x,z) measurements. Arrows represent the directions of the near-surface alongshore (at M1.5, M8 and M13) and near-surface ($\sim$ 2 m below mean sea level) and near-bottom ($\sim$ 2 m above the seafloor) cross-shore currents (at M8 and M13 only). The jetski required 30 min to complete the 8 cross-shore transects used for each map, and the centered-time (12:00-15:00 h) is shown to the right of each panel. Each CTD+Chl a transect consisted of 5 or 6 profiles. Black lines are temperature contours. The white line traces the 4 μg L^{-1} Chl a contour. 40

Figure 2.8: Contours of T ($^{\circ}$C) vs. time and z at (a) M27, (b) M18, (c) M15, (d) M13, (e) M8. Black stars represent an internal wave trough propagating onshore. The bold contour is a representative mid-water isotherm. The white star is the trough location at M8 predicted by linear theory. In (d) M13, Chl a (μg L^{-1}) is colored. Time zero corresponds to 00:00 h 12 October. 42

Figure 2.9: (a) Depth anomaly of mid water-column isotherms (bold contours in Fig. 8) vs. lagged time (T-Δt) at M27, M18, M15, and M13 (*see* legend), with Δt for each mooring chosen to orient the isotherm trough minimum at T = 0. (b) Observed (thick black line), theoretical phase velocity C_p (solid gray line (equation 1) and dashed gray (equation 2) and u_{max} (thin black line) above the wave trough vs. the water depth H. The observed C_p =Δx over Δt was estimated midway between neighboring moorings, with Δx the mooring separation. Error bars on observed C_p represent deviations associated with a $\pm$30 deg incident IW angle. The shaded region represents the potential C_p range from (1) based on the standard deviation of N. 44

Figure 2.10: Vertically averaged Chl a above the 17.0 $^{\circ}$C isotherm vs. isotherm depth (Δz) at 4 min intervals between 06:00 and 17:00 h (number of data points, n = 165) on 12 October 2006). The linear fit (dashed line) has slope 1.29 ± 0.03 μg L^{-1}m-1, and r^2 = 0.57, p < 0.01. 47

Figure 2.11: Chl a vs. T (at 12:00, 13:30, 14:15, and 15:00 h) based upon the CTD+Chl a surveys (between H = 5 to 13 m depth, *see* Fig. 7) horizontally averaged along 1 m isobars. 49

Figure 2.12: Timeseries of (a) depth $\langle z_{Chla} \rangle$ of the center of mass of cross-shore averaged Chl $a(z,t)$ and (b) squared half-width σ^2_{Chla} (eq. 5) of the Chl $a(z,t)$ layer from 11:30 to 15:30 h on 12 October. 53

Figure 2.13: Time series from 09:30 to 18:00 h on 12 October of (a) T (1 min averages), (b) Chl$a$ (1 min averages), and (c) dinoflagellate (solid) and diatom (dashed) conc. from M4 (H = 4 m) and M1.5 (H = 2 m), and in (a) 20 min average T, 2 m below the mean sea surface at M13 (H = 13 m) (*see* legend). The CTD+jetski sampling period (12:00 to 15:00 h, Fig. 7) is indicated by the gray bar between vertical dashed lines. 56

Figure 2.14: Schematic of nearshore ($H < 20$ m, *see* black box on Fig. 4d) summarizing the stages of the surface Chl$a$ band formation. (a) An intense Chl$a$ layer formed subsurface within 7 days preceding the surface appearance. (b) Chl$a$ in an sIW trough was locally concentrated by swimming and sIW strain as the wave propagated onshore, (c) sIW breaking in shallow water caused vertical mixing and outcropping of the 17.5 °C isotherm and upper portion of the Chl$a$ patch. On ebb tide, warm water carried by the surfzone alongshore current from the Talbert marsh, blocked Chl$a$ entry into the surfzone. 58

Figure 3.1: 24 h averaged timeseries of Chl$a$ (μg L^{-1}) conducted during the summer and fall of 2006 at Huntington Beach California. Three bloom events are identified by gray bars. Intensive bloom sampling was conducted during Bloom 3 between 27 September (day 100) and 16 October (day 120). 66

Figure 3.2: Schematic of the HB06 instrumentation: (a) plan view of bathymetry contours with the cross-shore (x) coordinate parallel to the instrument transect line and the alongshore (y) coordinate positive to the S-E, and (b) cross- shore transect of bathymetry. The vertical coordinate is z, with $z = 0$ m at the tidally averaged surface and positive upward. Moored thermistor strings (blue circles, M8 and M18) were located at tidally-averaged depths $H = 8$ and 18 m. Wind was measured slightly to the North of the main transect (black star). A vertically profiling CTD+Chl$a$ wirewalker (M13) was located at $H = 13$ m. A Chl$a$ fluorometer was also located near-bottom at $H = 15$ m. Bottom-mounted ADCPs (stars) were located near moorings M8 and M18. During an intensive bloom sampling period between 27 September and 16 October, CTD+Chl$a$ transects were conducted in a 16 ft. whaler in $H = 5$ to 60 m (yellow bar, panel a) and water samples were collected near the surface and bottom at roughly 1 km spacing (triangles, panel b, to 8 km from shore). The instrumentation shown here represent the data that is presented within this paper, and is a subset of the total instrumentation at HB06. 67

Figure 3.3: Optical (gray points) and bottle (black circles)NO_3 measurements versus temperature T, and the linear fit (thick black line) to the NO_3 bottle data versus temperature at HB06 throughout the intensive bloom sampling period. The HB06 measurements are consistent with previous fits to observations from throughout the Southern California Bight [*Dugdale et al.*, 1997; *Olivieri and Chavez*, 2000; *Lucas*, 2009]. . . . 70

Figure 3.4: Timeseries at mooring M18 of (a) current speed ($\mathrm{m\,s^{-1}}$), squared shear S ($\mathrm{s^{-2}}$), (c) temperature T (°C), (d) buoyancy frequency squared N^2 ($\mathrm{s^{-2}}$), (e) nitrate gradient $\frac{\partial \mathrm{NO_{3,T}}}{\partial z}$ ($\mathrm{mmol\,m^{-4}}$), (f) rate of isotherm displacement w ($\mathrm{m\,s^{-1}}$) at M18. Each series derived from T was vertically interpolated onto a 0.5 m grid. Contours indicate a boundary where the density difference ($\Delta\rho$) from the bottom was 0.2 $\mathrm{kg\,m^{-3}}$. 73

Figure 3.5: Timeseries at mooring M18 of (a) vertical isotherm displacement w ($\mathrm{m\,s^{-1}}$) and NO_3 at z_{eu}. (b) NO_3 flux driven by vertical advection of isotherms. 74

Figure 3.6: Timeseries at M18 of vertically averaged (a) S ($\mathrm{s^{-1}}$, gray line) and N ($\mathrm{s^{-1}}$, black line) across the bottom 5 m of the water column, and (b) estimated turbulent kinetic energy dissipation rate ($\varepsilon_{\mathrm{IW}}$) from the *Mackinnon and Gregg* [2005] parameterization. 76

Figure 3.7: An example of a logrithmic fit to the data from the four near-bed current meter bins with z_0 fixed at 1 cm for one 2 hr averaged increment (day = 47.7) of the subtidally filtered currents at M18. Correlation r^2= 0.96 ($p < 0.01$) and skill is 0.99. 78
Figure 3.8: Timeseries at mooring M18 of (a) u_* ($\mathrm{m\,s^{-1}}$) from logrithmic fits (black curve) and derived from a quadratic drag law (Eq. 3.8, gray curve) with $C_d = 1.5 \times 10^{-3}$ [*Shaw*, 1999] and (b) skill of the logarithmic fit (*e.g.,* Fig. 3.7). In (a), the two estimates of u_* are highly correlated ($r^2 = 0.99$, $p < 0.001$). In (b), 28% of the log-fit skill fell below the 0.9 cutoff limit (gray dashed line) and were removed from the analysis. 79
Figure 3.9: 24 h averaged timeseries of (a) vertical eddy diffusivity κ ($\mathrm{m^2\,s^{-1}}$) estimated from the *Mackinnon and Gregg* [2005] parameterization (black line) and the bottom boundary layer method (gray line) near z_{eu} = 14 m at M18. The two parameterizations are significantly linearly correlated, with $r^2 = 0.65$ and $p < 0.001$. (b) vertical NO_3 gradient $\partial \mathrm{NO_{3,T}}/\partial z$ ($\mathrm{mmol\,m^{-4}}$) at $z_{\mathrm{eu}} = -14$ m at M18. 81
Figure 3.10: 24 h averaged timeseries of vertically mixed (red line), vertically advected (gray line), and total (black line) vertical nutrient flux ($\mathrm{mmol\,m^{-2}\,d^{-1}}$) across z_{eu} at M18 and Chl*a* (green line) measured between z = 12 to 14 m at M15 and M13. The gray shaded region indicates where $\mathrm{NO_3 flux_{adv}}$ dominated the total flux, and the red shaded region indicates where $\mathrm{NO_3 flux_{mix}}$ dominated the total flux. The observed Chl*a* and $\mathrm{NO_3 flux_{tot}}$ have maximum lagged-correlation ($r^2 = 0.40$) at 8 days. 83
Figure 3.11: Averages (solid circles) and individual 1 m binned measurements (small dots) of optically measured NO_3 versus Chl*a* within the nearshore ($500 < x < 3000$ m) euphotic zone ($z < 14$ m) on each of the days during Bloom 3 when CTD+Chl*a*+NO_3 transects were conducted. The arrows illustrate the anticipated temporal progression during each bloom stage, beginning with the pre-bloom, pre-flux conditions, the NO_3 flux, NO_3 uptake and phytoplankton growth, and loss (mortality/sinking) from the euphotic zone. 86

Figure 3.12: Means (circles) and standard deviations (vertical bars) of dissolved inorganic NO_3 (mmol m^{-3}, red), NH4 (mmol m^{-3}, yellow), silicate (DSi, mmol m^{-3}, blue), and Chl a (μg L^{-1}, green) versus time from nearshore ($500 < x < 3000$ m) and euphotic zone ($z > z_{eu}$) bottle samples for each bloom stage (before the NO_3 flux (BF), during the NO_3 flux (NF),and during the dinoflagellate bloom (PB)). The estimated total vertical NO_3 flux (black line) and measured Chl a (green line) from Fig. 3.10 are shown for reference. 89

Figure 3.13: (a) Dissolved silicate (DSi) to NO_3 ratio versus Chl a (μg L^{-1}) from nearshore ($500 < x < 3000$ m) bottle samples averaged within the euphotic zone ($z > z_{eu}$, large white circles) for each bloom stage. DSi:NO_3 ratio versus Chl a (μg L^{-1}) below the nitracline ($NO_3 > 2.5\,\mu$, M, hollow dots) are clustered near 1 (solid line): the ratio predicted by [*Redfield*, 1958]. The mean silicate to NO_3 ratio below the euphotic zone (dashed line) is slightly higher than 1, indicating slight NO_3 limitation relative to DSi. (b) Ammonium (NH_4) to NO_3 ratio versus Chl a (μg L^{-1}) from nearshore ($500 < x < 3000$ m) bottle samples averaged within the euphotic zone ($z > z_{eu}$, large white circles) for each bloom stage. 90

Figure 3.14: Growth rate (μ, d^{-1}) versus NO_3 (mmol m^{-3}) for linear uptake (V = 0.52 m^3 d^{-1} mmol^{-1}, black line) and a Michaelis-Menten function (μ_{max} = 3.5 d^{-1}, $K_s = 3.4$ mmol m^{-3}, gray line). 89% of the non-zero observed $NO_{3,T} < K_s$ (dashed vertical line), indicating that for the majority of the observed NO_3 concentrations (and according to these parameter choices), the Michaelis-Menten curve was roughly linear. 93

Figure 3.15: Correlation coefficient (r^2, colors) and model-data skill (contours) between $P^{(m)}$ and $P^{(obs)}$ over a range of the linear uptake parameter (V, m^3 d^{-1} mmol^{-1}) and mortality rate (m d^{-1}). The asterisk indicates the optimal choice of $V = 0.52$ m^3 d^{-1} mmol^{-1} and $m = 0.55$ d^{-1} based upon the maximum correlation ($r^2 = 0.49$, $p < 0.001$) and skill (0.61). 95

Figure 3.16: Timeseries of 24 h averaged $P^{(obs)}$ (mmol m^{-3}, light green line) and $P^{(m)}$ (mmol m^{-3}, dark green line). The gray shaded regions indicate the time periods of the 3 bloom events. 97

Figure 3.17: Panels (a) to (c): Correlation coefficient (r^2, colors) and model-data skill (contours) over a range of the linear uptake parameter (V, $\mathrm{m^3\,d^{-1}\,mmol^{-1}}$) and mortality rate ($m$, $\mathrm{d^{-1}}$) for each bloom event. The asterisk indicates the parameter pair chosen for each bloom based on the maximum correlation and skill. (d) 24 h averaged timeseries of $P^{(\mathrm{obs})}$ (thick green line) and (with the optimal parameters selected in panels (a) to (c)) $P^{(\mathrm{m})}$ for each of the blooms. The maximum correlation and skill for each bloom are listed in Table. 3.2. 99
Figure 3.18: 24 h averaged timeseries of ln(Chl a) (gray line) with linear fits (black dashed lines) to the days (black points) with positive net growth ($(\mu - m) > 0$) during the three blooms. 101

LIST OF TABLES

Table 1.1: Some commercially available fluorometers for Chl *a* and/or τ measurements. 21

Table 2.1: Phytoplanktonic genera present on 12 October within the nearshore (H $<$ 20 m) and offshore (H $>$ 20 m) regions. The total number of cells counted within each region is *n*. Dinoagellates are identied in bold type. 36

Table 2.2: Separation distance (Δx), time lag maximizing r2 (Δt) and correlation coefficient (r^2) of the sIW depth contours at the midpoint (Midpt.) between adjacent moorings. The observed phase velocity C_p (obs.) = Δx/Δt. At each mooring location, theoretical C_p ($m\,s^{-1}$) from equation (1) and (2) and u_{max} ($m\,s^{-1}$, positive = onshore) above the wave trough. All correlations are significant at the 99% level. 43

Table 3.1: Percentage of cells among total counts, and r^2 with bottle measurements of Chl *a*, for dinoflagellates and diatoms, and the 4 most abundant phytoplanktonic genera (and species when possible) within each group. Percentages are given from above ($n = 7.5 \times 10^4$) and below ($n = 0.9 \times 10^4$) $z_{eu} = 14$ m. 82 bottle samples were collected between 27 September (day 100) and 16 October (day 120), with 47 bottle samples from above z_{eu} and 35 samples from below z_{eu}. Significant ($p < 0.001$) r^2 correlations are identified in bold font. 85

Table 3.2: Dates of the timeseries segments selected for bloom modeling, optimal *V* ($m^3\,d^{-1}\,mmol^{-1}$), optimal *m* (d^{-1}), r^2 and skill for the optimal *V* and *m*. The optimal parameters were selected at the maximum of the sum of the model-data r^2 and skill. 98

ACKNOWLEDGEMENTS

I am very grateful to my advisors, Peter Franks and Falk Feddersen. They have provided wonderful support and guidance, I have learned so much. I am so lucky as well to have such support and love from my family, my wonderful boyfriend Noah, and San Diego friends Lydia, Megan, Joie, Gino, Travis, Florina. The field work was a success through the collaboration of an excellent crew. Thank you to Brian Woodward, Bill Boyd, Kent Smith, Dennis Darnell, Ian Nagy, Dan Michrowski, Megan Mckenna, Meg Rippy, David Ortiz-Suslow, Heather Mcclendon, Brianna Martin, Katherine McLean and Megan Fehlberg. The observations presented in this dissertation were obtained within the framework of the larger Southern California Coastal Ocean Observing System (SCCOOS) and United States Geological Survey (USGS) programs at Huntington Beach. George Robertson, Marlene Noble, Uwe Send, Steve Weisberg and Ali Boehm are thanked for their cooperation and assistance. California Sea Grant, National Oceanic and Atmospheric Administration, California Coastal Conservancy, National Science Foundation and the Office of Navel Research supported this research. Sea Grant support was through the California Sea Grant College Program Project #R/CZ-196, through NOAA's National Sea Grant College Program, U.S. Dept. of Commerce. This research was supported in part by California Sea Grant, NOAA, California Coastal Conservancy, and ONR. Sea Grant support was through the California Sea Grant College Program Project #R/CZ-196, through NOAA's National Sea Grant College Program, U.S. Dept. of Commerce.

VITA

2003	B. Sc. (Hons) in Physics, University of Guelph, Guelph, Ont. Canada
2011	Ph. D. in Physical Oceanography, University of California, San Diego, USA

PUBLICATIONS

Omand, M. M., Leichter, J. L., Franks, P. J. S., Guza, R. T., Lucas, A. J., and Feddersen, F., "Physical and biological processes underlying the sudden surface appearance of a red tide in the nearshore', *Limnology and Oceanography*, in press (2011).

Omand, M. M, Feddersen, F., Clark, D. B., Franks, P. J. S., Leichter, J. L., and Guza, R. T., "The influence of bubbles and sand on Chlorophyll-a fluorescence measurements in the surfzone", *Limnology and Oceanography: Methods*, 7, p. 354-362, 2009.

Clark, D. B., Feddersen, F., Omand, M. M and Guza, R. T., "Measuring fluorescent dye in the bubbly and sediment laden surfzone", *Water, Soil and Air Pollution*, DOI: 10.1007/s11270-009-0030-z, 2009.

Omand, M. M, Campbell, J. L. and Maxwell, J. A., "Simulation of the relationship between element concentrations and X-ray yields in the Mars Exploration Rover's X- ray spectrometer", *Nucl. InstrumMeth. In Phys. Research* , B229, p. 123-136, 2005.

ABSTRACT OF THE DISSERTATION

Physical controls on episodic nearshore phytoplankton blooms in Southern California

by

Melissa Margaret Omand
Doctor of Philosophy in Oceanography

University of California San Diego, 2011

Peter J.S. Franks, Co-Chair

Falk Feddersen, Co-Chair

The nearshore and surfzone in Southern California are highly dynamic regions ($<$ 20 m depth), and governed by different processes than water further offshore. As such, these are also unique environments for phytoplankton; affecting the spatial and temporal distributions of chlorophyll *a* (Chl*a*, a proxy for phytoplankton biomass) and nutrient delivery. This dissertation explores the challenges of making Chl*a* measurements in the turbid surfzone, and presents data from a novel sampling platform designed for nearshore and surfzone measurements. The underlying mechanisms driving Chl*a* variability over hourly, weekly and monthly scales are investigated. The data presented here was collected during a 4-month field experiment at Huntington Beach, CA during Summer and Fall 2006. Chapter one demonstrates the data errors induced by in situ optical fluorometers within the bubbly and sandy surfzone. A method for data correction is developed, and applied to surfzone field observations. Chapter two describes the sudden appearance at the surface of an alongshore-parallel band of a redtide dominated by the regionally common dinoflagellate *Lingulodinium polyedrum* (F. Stein). The red tide band was mapped in high spatial and temporal resolution using novel instrumentation including a global positioning

system (GPS) -tracked jetski. Data from a series of moorings and CTD profiles provide insight into the sequence of events that culminated in the surface red tide appearance. And finally, Chapter three explores the drivers of episodic phytoplankton blooms over the entire four month record. Three pulses of estimated advective and turbulent vertical nitrate (NO_3) flux, are found to precede three phytoplankton blooms by approximately 8 days. Chl$a$ predicted from a very simple NP model driven only by the estimated NO_3 fluxes captured the timing, width and approximate magnitude of each of the blooms ($r^2 = 0.49$), verifying that the vertical NO_3 flux was a important control on the bloom events.

Chapter 1

The Influence of Bubbles and Sand on Chlorophyll-*a* Fluorescence Measurements in the Surfzone.

1.1 Abstract

Continuous Chlorophyll-*a* (Chl a) measurements in the surfzone (region of wave-breaking adjacent to the shoreline) would increase understanding of harmful algal blooms, food supply for intertidal invertebrates and fishes, and the fate of terrestrial run-off pollution. However, optical measurements of Chl a fluorescence in the surfzone are affected by bubbles and suspended sand. Here, errors in surfzone Chl a fluorescence measurements (using WET Labs ECO Triplet fluorometers) are estimated by comparing observed (Chl a_{raw}) with known (Chl a_{true}) Chl a concentrations in laboratory tests with controlled amounts of bubbles and suspended sand (characterized with concurrently measured optical turbidity τ). For both bubbles and sand, Chl a_{raw} and τ are linearly correlated, and the regression line slope depends on Chl a_{true}. When Chl a_{true} is low, Chl a_{raw} is biased high. In contrast, when Chl a_{true} is high, Chl a_{raw} is biased low. Fluorometers were also deployed in a natural surfzone, and for the limited range of field Chl a observed, the field and laboratory τ-Chl a relationships are largely consistent. Mechanisms responsible for these biases

are proposed, correction procedures using the observed τ-Chl$a$ relationship are developed, and applied to surfzone Chla_{raw} observations. For the moderate Chla_{true} concentrations (2 to 4 $\mu\mathrm{g\,L^{-1}}$) encountered, errors in hourly mean and instantaneous Chla_{raw} are less than 5% and 15% respectively. Larger errors are expected for Chla_{true} outside this range. Although further testing is needed, the results suggest *in situ*, optical Chla_{raw} from other turbid environments (e.g. estuaries, bays) should also be interpreted cautiously.

1.2 Introduction

Chlorophyll-a fluorescence (Chl$a$), often used as a proxy for phytoplankton biomass [*e.g.*, *Falkowski and Kiefer*, 1985], is measured by laboratory extraction from discrete water samples (Chla_{true}), or continuously with *in situ* optical fluorometers (Chla_{raw}). The fast sampling and convenience of *in situ* optical instruments are advantageous, and *in situ* Chl$a$ sampling is common in the open ocean and on continental shelves. Light scattering near the ocean surface is generated by a variety of seawater constituents, including bubbles, sand, plankton and detritus [*e.g.*, *Stramski et al.*, 2004]). The relative contributions of these constituents to the total light scattering are variable over time and space. For example, beneath open-ocean breaking waves, bubble-induced light scattering spans several orders of magnitude over time periods of minutes [*Terrill et al.*, 2001]. Optical Chl$a$ measurements are affected by scattering from particulates and so data from very near the surface and seafloor (where the concentration of scatterers is highest) are often discarded.

Continuous Chl$a$ measurements in the surfzone (region of wave-breaking adjacent to the shoreline) could aid understanding of harmful algal blooms, food supply for intertidal invertebrates and fishes, and the fate of terrestrial run-off pollution. However, owing to wave breaking and strong currents in shallow water (few m depth), sediment suspended from the sea bottom, and bubbles injected at the surface, can intermittently populate the entire water column [*e.g.*, *Deane and Stokes*, 1999a]. The relative contributions of sand and bubbles to a point measurement of surfzone light scatter is not understood, but backscat-

ter is known to depend on cross-shore location and distance above the seafloor [*Wang et al.*, 2002]. Backscattered light is known to be problematic for accurate measurement of fluorescent dye with benchtop fluomoeters [*Smart and Laidlaw*, 1977] and *in situ* in the surfzone [*Clark et al.*, 2010]. Here, the fluorometer response in turbid water is characterized, and methods are developed to correct continuously observed Chl$a$ in the surfzone and (potentially) other turbid environments.

Turbidity from a calibrated nephelometer (τ, units of nephelometric turbidity units or ntu) characterizes the water cloudiness by observing the amount of emitted light that is backscattered by particles, relative to a secondary standard of clear water. Turbidity depends on the particle concentration, size, shape, and internal index of refraction, as well as the emitted light wavelength and details of the optics [*e.g.*, *Zaneveld et al.*, 1979]. The single-frequency turbidity sensors used here provide a bulk estimate of the scattering by all particles in the sample volume.

The influence of bubbles and sand on Chla_{raw} is explored by simultaneously measuring Chla_{raw} and τ with a WET Labs ECO Triplet fluorometer. Two τrelated mechanisms can distort ECO Triplet Chla_{raw} (Fig. 1.1). Sand and bubbles can scatter light emitted from the τ channel into the Chl$a$ detector. The wavelength ranges of the τ emitter and Chl$a$ detector overlap (pers. comm. WET Labs personnel, technical specs unavailable), elevating (e.g. enhancing) Chla_{raw} (mechanism A, Fig. 1.1a). This mechanism is explored by observing Chla_{raw} with and without the τ emitter blocked. Sand and bubbles also scatter and absorb excited and fluoresced light away from the Chl$a$ emitter/detector thereby reducing Chla_{raw} (mechanism B, Fig. 1.1b). This mechanism is evaluated over a range of bubble- and sand-induced τ for a range of known Chla_{true} concentrations. Fluorometers were also deployed in a natural surfzone, and field and laboratory τ-Chl$a$ relationships are consistent within the limited range of field Chl$a$ observed. Correction procedures using the observed τ-Chl$a$ relationship are developed, and applied to surfzone Chla_{raw} observations. The effect of fluorescent dye (mechanism C, Fig. 1.1c) and sunlight (mechanism D, Fig. 1.1d) on Chla_{raw}) and the τ response of a flow-through WET Labs WETStar fluorometer are

discussed in Appendices.

1.3 Materials and Procedures

1.3.1 ECOTriplet Fluorometer

Laboratory and field tests used four 3-channel WET Labs ECO Triplet Fluorometers (www.wetlabs.com) that measure Chl$a$ (470/695 nm excitation/emission wavelengths, 0 to 150 μg L^{-1} range), Rhodamine-WT dye (540/570 nm excitation/emission wavelengths, 0.2 to 500 ppb range) and backscattered turbidity (660 nm wavelength, 0.03 - 100 nephelometric turbidity units (ntu) range). In the field, ECO Triplets internally stored the 3.8 sec average of 8 Hz samples. In the lab, 8 Hz samples were averaged for about 1 sec. Before testing, the ECO Triplets were calibrated with natural phytoplankton populations (collected from the SIO pier) to within 4% of the WET Labs-provided Chl$a$ calibration. The WET Labs-provided calibration for turbidity was used to convert the backscatter from counts to units of ntu.

1.3.2 Laboratory Methods

To reduce the effect of ambient light, laboratory tests were performed in a round 15 L (30 cm diameter) black-lined bucket with a downward pointing ECO Triplet. In fresh, Chl$a$-free water, boundary effects (significant and slight enhancement in τ and Chla_{raw} respectively) were evident only within 5 cm of the bucket wall or bottom. Elsewhere τ and Chla_{raw} were near zero, indicating minimal interference from bucket wall reflections where the tests below were performed. The effect of bubble-generated τ on Chla_{raw} was measured by injecting, into water with known Chla_{true}, controlled quantities of bubbles using a balsa wood bubbler attached to the end of an air hose. The hose air pressure was adjusted so that the bubble-induced τ range was similar to surfzone field tests (0 to 90 ntu). Nominal bubble radius ranged from 1 to 5 mm, representative of surfzone bubbles [*Deane*

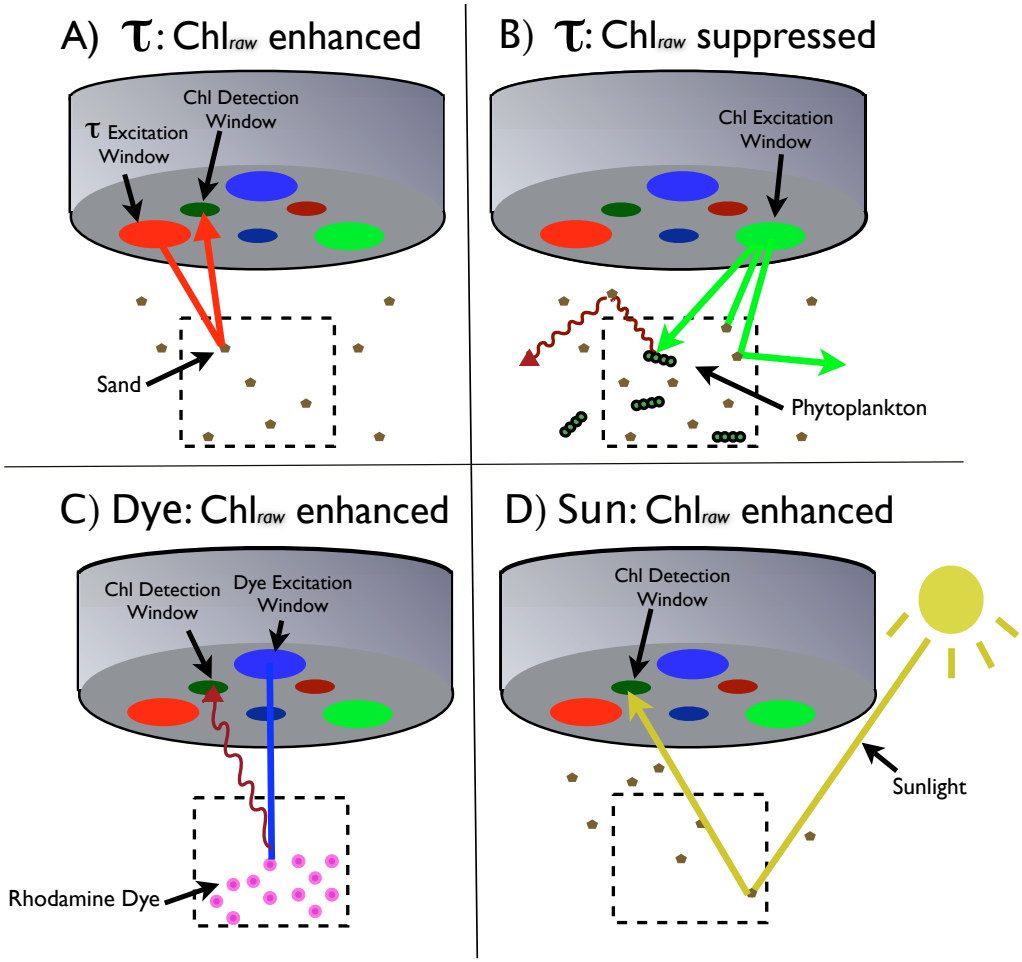

Figure 1.1: Schematic of the 3-channel (Chl *a*, turbidity, dye) WET Labs ECO Triplet and four potential mechanisms for Chl *a* error. The dashed box represents the sample volume, located a few centimeters from the 10 cm diameter sensor head. (a) Chl a_{raw} enhancement through scattering of the 660 nm turbidity excitation into the Chl *a* detection window (mechanism A), and (b) Chl a_{raw} suppression through scattering of the fluoresced 685 nm light away from the Chl *a* detection window (mechanism B). (c) Chl a_{raw} enhancement through detection of dye fluorescence as Chl *a* (mechanism C), and (d) Chl a_{raw} enhancement through ambient sunlight near 685 nm scattered into the Chl *a* detection window (mechanism D). The Chl *a* detection window wavelength range overlaps with the range of emitted τ (A) and dye-fluoresced light (D).

and Stokes, 1999b]. Similar tests were done with controlled amounts of suspended sand. Dry sand from Scripps Beach (mean diameter approximately 0.2 mm) was kept in a dry, dark container for at least one week to eliminate fluorescence from live phytoplankton attached to the grains. Sand-induced τ was generated by stirring up to 200 g of dry sand in the 15 L bucket. Laboratory sand concentrations (0 to 13 $\mathrm{g\,L^{-1}}$) were comparable to instantaneous near-bed concentrations observed in sandy beach surfzones [*e.g.*, *Yu et al.*, 1993; *Beach and Sternberg*, 1996], and the turbidity range was similar to field observations (0 to 90 ntu). Phytoplankton, obtained by towing 60 μm mesh nets from the SIO pier in La Jolla CA, were mixed with sand-filtered (Chl$a$ 0.1 $\mu\mathrm{g\,L^{-1}}$) seawater to obtain five samples (10 L each) with Chl$a$ between 0.2 and 10 $\mu\mathrm{g\,L^{-1}}$. Chla_{true} was measured by filtration of a 150 mL water sample onto 25 mm GF/F filters, extraction in 10 mL acetone, and assessed with a calibrated Turner Designs 7000 benchtop fluorometer. Three extractions at each Chl$a$ concentration indicate reproducibility to less than 0.5 $\mu\mathrm{g\,L^{-1}}$.

1.3.3 Chla_{raw} field measurements

A month-long field experiment was conducted at Huntington Beach CA in Fall 2006. Seven bottom-mounted instrumented (temperature, pressure, and current) frames were deployed on a 160 m long cross-shore transect (from 0 to 4 m depth, relative to mean sea level), that spanned the surfzone for the wave conditions encountered. Pressure sensor data was used to calculate hourly significant wave height and the tidally-varying mean sea surface. Four ECO Triplet fluorometers were repeatedly deployed for 72 h periods on different frames, facing 30deg from downward, nominally 50 cm above the seafloor.

1.4 Assessent

In undisturbed (no bubbles or sand) freshwater with Chla_{true} = 0, τ and Chla_{raw} were approximately 0 ntu and 0 $\mu\mathrm{g\,L^{-1}}$ respectively (Fig. 1.2, shaded region from 0-50 sec).

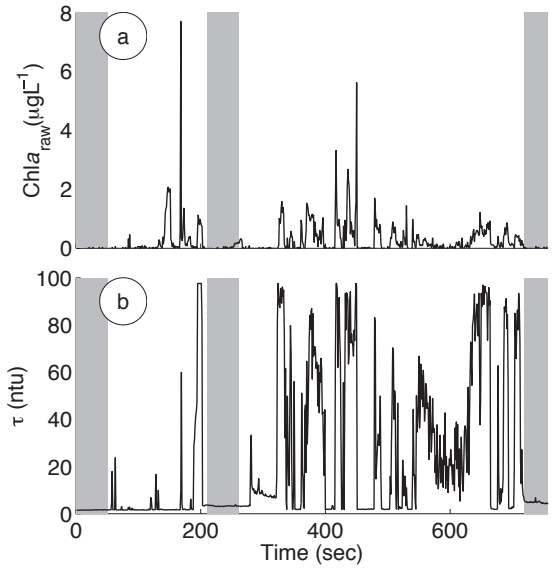

Figure 1.2: (a) Measured Chla_{raw} and (b) bubble-induced turbidity τ versus time in fresh, Chl$a$-free water with no ambient light. Vertical gray bars indicate times without bubbles.

With the addition of bubbles, τ and Chla_{raw} spiked as high as 95 ntu and 7 μg L^{-1}, respectively (Fig. 1.2, non-shaded regions). When bubbling stopped, τ and Chla_{raw} dropped to near zero (Fig. 1.2, gray-shaded region near 205 sec). Sporadic Chla_{raw} spikes occur (e.g., Chla_{raw} = 7 μg L^{-1} at time 190 sec, Fig. 1.2) and were filtered by rejecting data where the Chla_{raw} rate of change exceeded 1 μg L^{-1}s-1, a threshold selected to remove large spikes while retaining most of the data. This spike filter, applied to all laboratory Chla_{raw} data, removed between 15% and 35% of data points. After spike removal, Chla_{raw} and bubble-induced τ were significantly correlated (slope (α) = 0.008 $\pm$ 0.001 μg L^{-1} ntu^{-1}, r^2 = 0.41 $p < 0.001$, Fig. 1.3a) indicating that mechanism A (Fig. 1.1a) enhances the measured Chla_{true}. Similarly, Chla_{raw} and sand-induced τ were correlated (α = 0.0046 $\pm$ 0.0005 μg L^{-1} ntu^{-1}, r^2 = 0.64 $p < 0.001$, Fig. 1.3c). The τ-induced enhancement was reproduced in all four ECO Triplets tested.

To confirm that light from the τ channel enhances Chl$a$ (mechanism A, Fig. 1.1a),

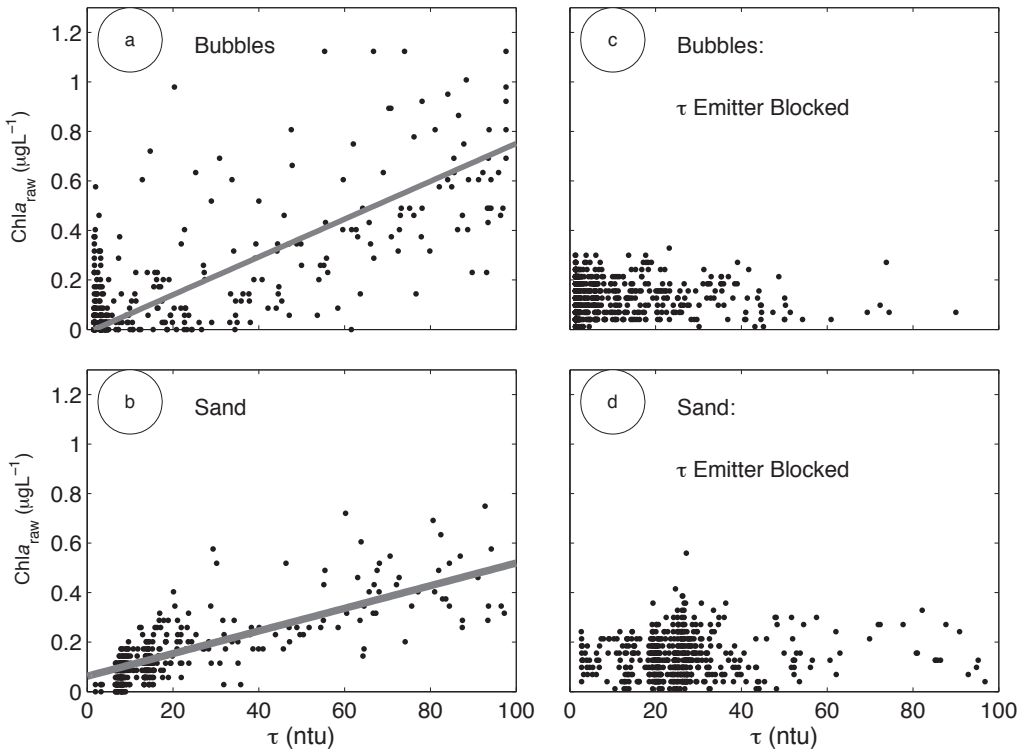

Figure 1.3: Chl a_{raw} versus turbidity (τ) (black points) and linear best fit (gray line) in Chl a-free freshwater with no ambient light with (a) bubble-induced τ (slope = 0.008 $\pm$ 0.001 μg L^{-1} ntu^{-1}, r^2 = 0.41, $p < 0.001$), and (b) sand (slope = 0.0046 $\pm$ 0.0005 μg L^{-1} ntu^{-1} , r^2 = 0.64, $p < 0.001$). Chl a_{raw} with τ emission blocked versus turbidity (black points) in fresh, Chl a-free water with no ambient light, and with (c) bubble-induced (r^2 = 0.01, p = 0.24), and (d) sand-induced (r^2 = 0.002, p=0.63) turbidity.

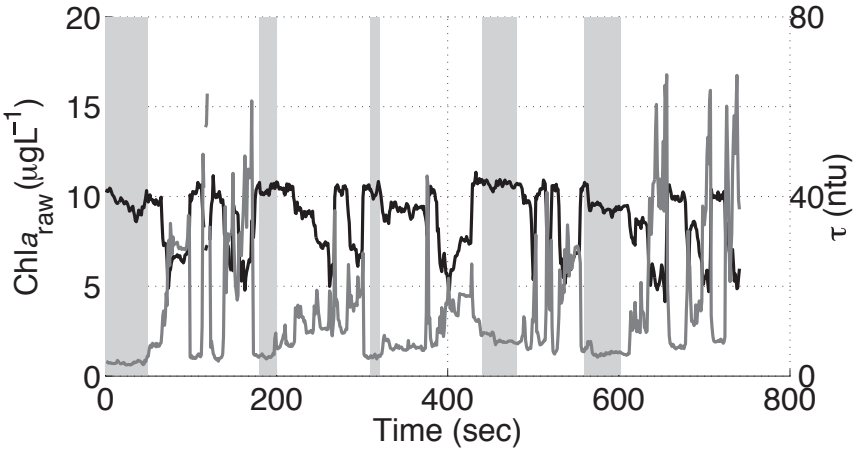

Figure 1.4: Chl a_{raw} (black) and bubble-induced turbidity (dark gray) versus time in seawater with Chl a_{true} = 10 μg L^{-1}. Vertical gray bars indicate times without bubbles.

the Chl a = 0 tests were repeated with the τ light excitation on one ECO Triplet blocked. A second, adjacent ECO Triplet measured τ. After spike-filtering, τexcitation-blocked Chl a_{raw} was near zero and uncorrelated with τ for both sand and bubbles (Fig. 1.3b,d), confirming that for these Chl a_{true} = 0 tests, the dominant noise source is enhancement from the τ channel.

In seawater with Chl a_{true} = 10 μg L^{-1} (typical of a coastal phytoplankton bloom), the τ-Chl a_{raw} relationship is opposite that for Chl a_{true} = 0 μg L^{-1} (Fig. 1.4). In undisturbed seawater, τ remained steady at 5 ntu (shaded regions in Fig. 1.4). When bubbles were added, Chl a_{raw} and τ were inversely related (unshaded regions in Fig. 1.4) with Chl a_{raw} decreasing by 40% at high τ, indicating that mechanism B (Fig. 1.1b) is dominant. When bubble injection intermittently ceased (gray-shaded regions, Fig. 1.4), τ and Chl a_{raw} returned to undisturbed levels. The observed τ and Chl a_{raw} (at fixed Chl a_{true}) are linearly related (Fig. 1.5) and may be described by the equation:

$$\text{Chl}\, a_{\text{raw}}(\tau) = \text{Chl}\, a_{\text{true}} + \gamma\tau \tag{1.1}$$

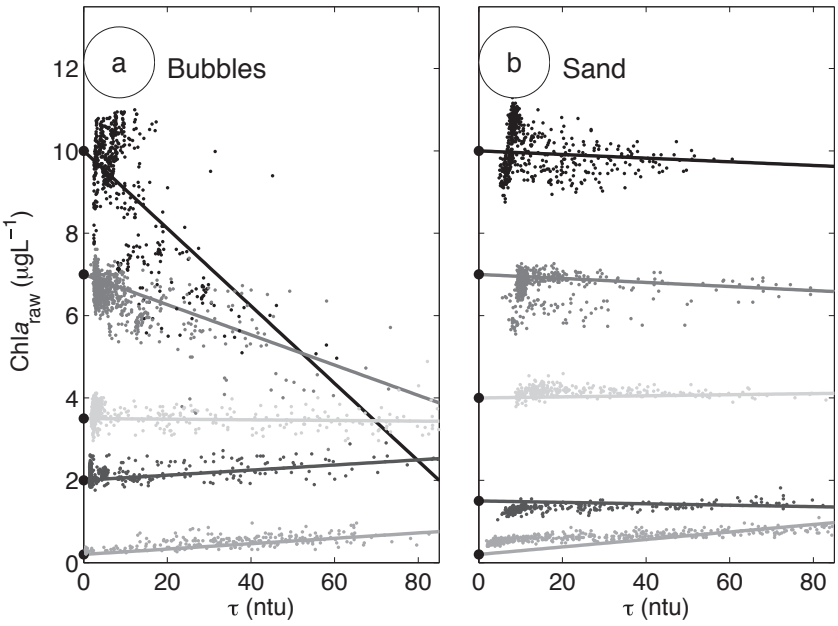

Figure 1.5: Chl a_{raw} versus turbidity (τ) in seawater with 5 known Chl a_{true} concentrations (black asterisks on vertical axis corresponding to 10, 7, 4, 1.5 and 0.2 μg L^{-1}) for (a) bubble-induced and (b) sand-induced τ. Solid lines are linear fits with intercept set equal to Chl a_{true}. The fraction of variance described by each fit (in ascending Chl a_{true} order) is r^2 = **0.48**, hi **0.45**, **0.05**, **0.22**, **0.52** (bubbles) and r^2 = **0.10**, 0.01, 0.01, **0.46**, **0.70** (sand). The r^2 in bold type correspond to $p < 0.001$.

Non-linear (quadratic and exponential) fits were also explored, but did not improve the goodness of fit (e.g., Akaike and Bayesian Information Criteria (AIC-BIC), Schwarz 1978). For bubble-induced turbidity tests (Fig. 1.5a), the slope (γ) of the τ-Chl a_{raw} fit depends on Chl a_{true}, ranging from enhancement at 0.2 μg L^{-1} (mechanism A) to strong suppression at 10 μg L^{-1} (mechanism B). Near Chl a_{true} = 4 μg L^{-1}, $\gamma \sim 0$ and the two mechanisms approximately cancel. Sand-generated τ and Chl a_{raw} show a similar, but less pronounced pattern (Fig. 1.5b).

A proposed model for the relationship between Chl a_{raw} and τ is

$$\mathrm{Chl}\,a_{\mathrm{raw}}(\tau) = \mathrm{Chl}\,a_{\mathrm{true}} + \alpha\tau + \beta_n(\mathrm{Chl}\,a_{\mathrm{true}})^n\tau, \tag{1.2}$$

where the 2nd and 3rd terms on the right hand side represent mechanisms A and B respectively, α and β are empirically determined constants and the exponent n is an integer. Using (2), the dependence of the slope γ (1) on $\mathrm{Chl}\,a_{\mathrm{true}}$ is

$$\gamma = \alpha + \beta_n(\mathrm{Chl}\,a_{\mathrm{true}})^n. \tag{1.3}$$

In agreement with (1.3), γ observed depends nearly monotonically on $\mathrm{Chl}\,a_{\mathrm{true}}$, and model fits with n= 1 and n= 2 were explored (solid and dashed curves in Fig. 1.6). For the bubbles tests, the quadratic fit (n = 2) improved the AIC-BIC over the linear fit (n = 1), however both are encompassed within the error bars on γ at $\mathrm{Chl}\,a_{\mathrm{true}} < 10\ \mu\mathrm{g\,L^{-1}}$. For the sand tests, the linear fit was most appropriate (black line in Fig. 1.6). Choice of an optimal model (linear or quadratic) likely will depend on the observed $\mathrm{Chl}\,a_{\mathrm{true}}$ range. For small ranges in $\mathrm{Chl}\,a_{\mathrm{true}}$ the quadratic approaches the linear model, whereas for a large range in $\mathrm{Chl}\,a_{\mathrm{true}}$, the relationship will be strongly dependant on the choice of n. Bubble-generated turbidity yields β_2 $\sim$0.001 $\mu\mathrm{g\,L^{-1}\,ntu^{-1}}$ for the quadratic fit, and β_1 $\sim$0.01 $\mathrm{ntu^{-1}}$ (nearly ten times larger than the β_1 $\sim$0.001 $\mathrm{ntu^{-1}}$ for sand). For single channel fluorometers (no τ channel), suppression (mechanism B) is present. Tests with a single channel WETStar fluorometer and a separate τ sensor in a flow-through package agree qualitatively with (1.2) with α = 0 (Appendix C).

The laboratory tests were conducted with either bubbles or sand only. In the surfzone, bubbles and sand are both present, in unknown amounts, so the appropriate α and β_n for field applications are unknown. The α and β_n obtained from sand only and bubble only lab tests are considered an envelope for the range in $\mathrm{Chl}\,a$ error.

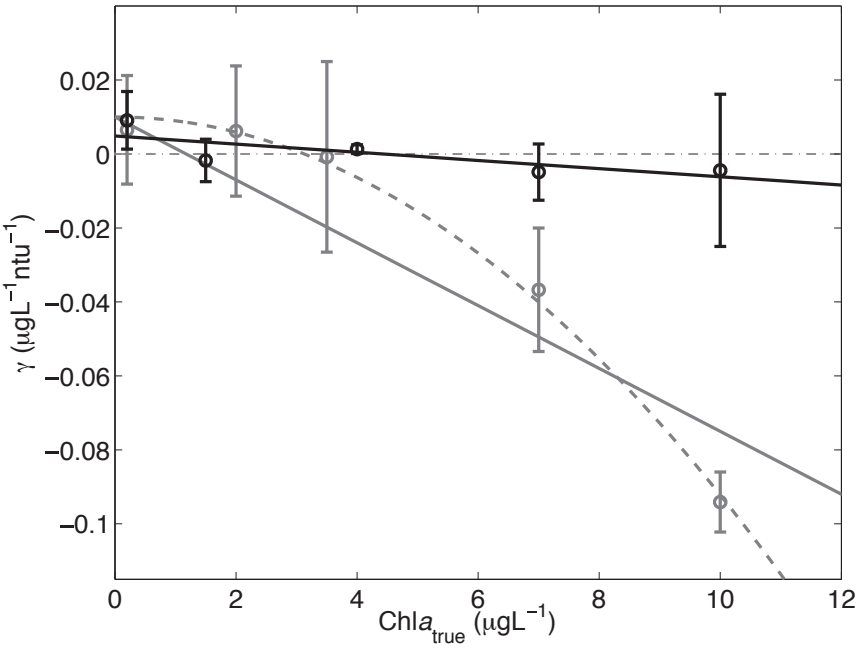

Figure 1.6: Laboratory τChla_{raw} regression slopes γ (from Fig. 5) versus Chla_{true} for bubble (gray) and sand (black) tests. The solid lines are linear regression fits (eq. 3) with intercepts (α = 0.008 $\pm$ 0.001 μg L^{-1} ntu^{-1} (bubbles) and α = 0.0046 $\pm$ 0.0005 μg L^{-1} ntu^{-1} (sand)) determined from Chla_{true} = 0 tests. The linear best fit slopes β1 are -0.010 $\pm$ 0.003 ntu^{-1}, r^2=0.90, p = 0.01 (bubbles), and -0.0011 $\pm$ 0.0003 ntu^{-1}, r^2 = 0.59, p = 0.12 (sand). The gray dashed line represents the best quadratic fit for bubbles (β2 = -0.001 Lμg^{-1} ntu^{-1}) with intercept (α = 0.008 $\pm$ 0.001 μg L^{-1} ntu^{-1}) determined from Chla_{true} = 0 tests. The black dot-dashed line at γ = 0 indicates the border between τ-induced enhancement ($\gamma > 0$) and suppression ($\gamma < 0$).

1.5 Discussion

Surfzone field observations are examined in light of the laboratory tests showing that turbidity generates Chl a_{raw} errors that depend upon Chl a_{true}. Field data was retained only if the ECO Triplet was more than 1 m below the mean free surface, thus reducing the effect of scattered sunlight (Appendix C) and excluding observations (usually at low tide) when the sensor pierced the water surface in wave troughs. The spike filter (a cut-off of 0.25 $\mu\mathrm{g\,L^{-1}}$s-1 was chosen for field data because the ECO Triplets were sampled at 0.25 Hz rather than the 1 Hz lab sample rate) removed obvious Chl a_{raw} spikes while preserving 95 % of the data.

Laboratory tests examined τ-induced errors in Chl a_{raw} with known, fixed Chl a_{true}. (Figs. 1.4, 1.5, and 1.6). Field data segments are selected for comparable analysis. Chl $a_{\mathrm{nat}}$for each 3-h segment is defined as the Chl a_{raw} values when $\tau < 10$ ntu (gray points, Fig. 1.7). Of 250 original segments, 85 were retained with 1) small Chl a_{nat}variation (standard deviation < 1 $\mu\mathrm{g\,L^{-1}}$) and 2) broad variation in τ (upper τ limit > 50 ntu). For the 85 cases, Chl a_{raw} was typically low (< 5 $\mu\mathrm{g\,L^{-1}}$), and Chl a_{raw} and τ were often significantly correlated (r^2 ranging between 0.2 and 0.6). Linear best-fits between Chl a_{raw} and τ yield γ values for each 3 h segment (Fig. 1.7) that are similar to laboratory γ with known, fixed Chl a_{true}. (Fig. 1.5). Extracted Chl a from bottle samples were not available for each of these time periods and fluorometer locations, thus the median Chl a_{nat}(Chl $a_{\mathrm{m,nat}}$) was assumed to approximate Chl a_{true}. The field γ-Chl $a_{\mathrm{m,nat}}$relationship (where τ is caused by a mix of bubbles and sand) is bounded by the results from lab tests with sand and bubbles introduced separately (shaded region of Fig. 1.8). The field Chl $a_{\mathrm{m,nat}}$range is limited between 1 and 4 $\mu\mathrm{g\,L^{-1}}$. Within this range, a quadratic relationship between γ and Chl $a_{\mathrm{m,nat}}$ did not improve the fit (according to the AIC-BIC). Therefore, for the observed Chl $a_{\mathrm{m,nat}}$ range, a linear model (n = 1) was considered most appropriate. For larger Chl a_{true} , this may not be appropriate. The γ-Chl $a_{\mathrm{m,nat}}$ relationship may differ within and seaward of the surfzone due to the different contributions of breaking-wave induced bubbles and sand to

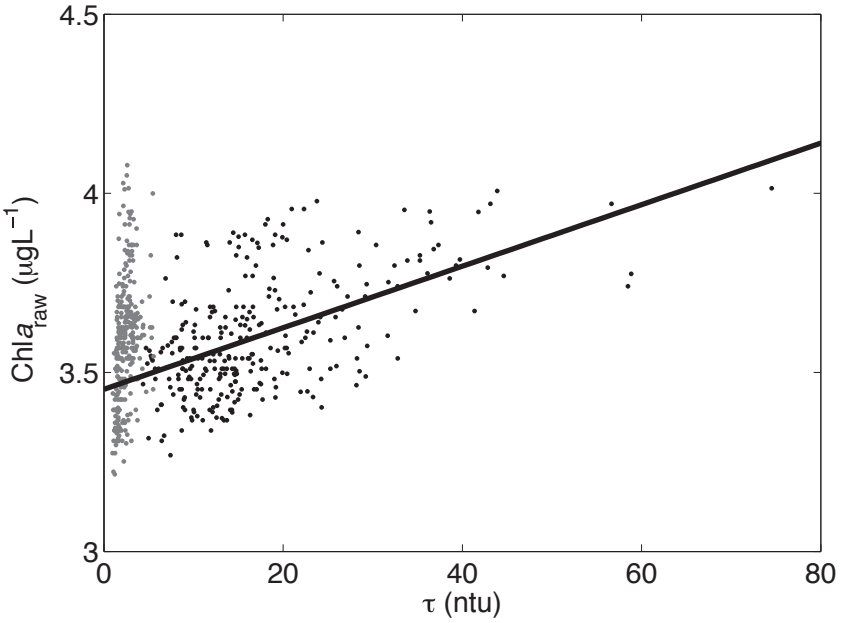

Figure 1.7: Chl a_{raw} versus turbidity (τ) within the surfzone for a single 3-h period. Each dot is a 4 sec observation. The gray points (Chl a_{nat}) are Chl a_{raw} with $\tau < 10$ ntu , and the median Chl a_{nat} (Chl $a_{\mathrm{m,nat}}$) approximates Chl a_{true} for this period. The black dashed line is a linear best fit (slope ((γ) = 0.0086 μg L^{-1}ntu, $r^2 = 0.29$, $p < 0.001$).

turbidity. However, the fit skill, intercept and within and seaward of the surfzone are not statistically different and so an α_{field} and β_{field} (representing all data) were selected. The model parameters optimizing the linear fit are β_{field} = -0.004 $\pm$ 0.002 μg L^{-1} ntu^{-1} and α_{field} = 0.017 μg L^{-1}.

Typical variations of τ, tides, waves, and Chl a are illustrated with 48 h of observations at two fixed locations, one within the surfzone, and the other further seaward (Fig. 1.9). Wave heights at the seaward location varied less than 10% from 0.55 m (Fig. 1.9c). At lower tide stages, the shallow instrument was near the surface, occasionally exposed in wave troughs, and τ and Chl a_{raw} were noisy (Figs. 1.9a and 1.9d). Data from less than 1 m below the surface were discarded, and spikes removed (black line, Fig. 1.9e). Corrections for the τ-induced errors are based on (1.2), with n = 1,

$$\mathrm{Chl}\,a_{\mathrm{corr}}(t) = \frac{\mathrm{Chl}\,a_{\mathrm{corr}}(t) + \alpha_{\mathrm{field}}\tau(t)}{1 + \beta_{\mathrm{field}}\tau(t)}, \tag{1.4}$$

where t is time. The corrected (red line, Fig. 1.9e) and raw data (black line, Fig. 1.9e) are similar for the range of $\mathrm{Chl}\,a_{\mathrm{raw}}$ encountered. The instantaneous (and hourly-mean) errors induced by τ reach 15% (5%) within the surfzone (black line, Fig. 1.9f) and are negligible seaward (gray line, Fig. 1.9f). With the modest range of observed $\mathrm{Chl}\,a_{\mathrm{raw}}$, the model (1.1) predicts that τ-generated errors in $\mathrm{Chl}\,a_{\mathrm{raw}}$ seaward of the surfzone would be limited to 1% (at 5 ntu), whereas errors within the surfzone would surpass 15% (above 30 ntu).

Turbidity depended on the cross-shore location (within or seaward of the surfzone) and decreased with depth below the surface. At the most offshore fluorometer ($\sim$ 160 m from shore), τ was below 5 ntu 90% of the time, and $\mathrm{Chl}\,a_{\mathrm{raw}}$ typically ranged between 2 and 7 $\mu\mathrm{g\,L^{-1}}$ (gray lines in Fig. 1.10). Within the surfzone ($\sim$ 20 m from shore), the τ range was larger, falling below 30 ntu 90% of the time, and the $\mathrm{Chl}\,a_{\mathrm{raw}}$ range was smaller than offshore (black lines in Fig. 1.10). Natural $\mathrm{Chl}\,a_{\mathrm{true}}$ variability may be driven by advection of horizontal and vertical phytoplankton patches, cell growth and death, phytoplankton behavior (swimming or sinking) or physiological adaptations to light. Nearshore Chl$a$ levels are often variable. For example, $\mathrm{Chl}\,a_{\mathrm{true}}$ was $< 1\ \mu\mathrm{g\,L^{-1}}$ 10.0% and $> 10\ \mu\mathrm{g\,L^{-1}}$ 7.4% of the time in bi-weekly bottle samples from the SIO pier (5 m total depth, La Jolla, CA, SCCOOS.org) between April 2005 and April 2008. During these time-periods, if τ reaches 50 ntu , bubble- and sand-induced ECO Triplet errors (assuming a linear [n = 1] relationship between γ and $\mathrm{Chl}\,a_{\mathrm{true}}$) may be on the order of 80% (low $\mathrm{Chl}\,a_{\mathrm{true}}$) and 20% (high $\mathrm{Chl}\,a_{\mathrm{true}}$) respectively (Fig. 1.11a). In single-channel fluorometers when mechanism A is not present, the ratio between $\mathrm{Chl}\,a_{\mathrm{raw}}$ and $\mathrm{Chl}\,a_{\mathrm{true}}$ would depend on τ, and under moderate surfzone conditions (30 ntu) and moderate $\mathrm{Chl}\,a_{\mathrm{true}}$, $\mathrm{Chl}\,a_{\mathrm{raw}}$ would underestimate $\mathrm{Chl}\,a_{\mathrm{true}}$ by 15% (Fig. 1.11b). In some highly productive areas, $\mathrm{Chl}\,a_{\mathrm{true}}$ frequently surpasses $10\,\mu\mathrm{g\,L^{-1}}$, and during intense blooms, may reach $> 100\,\mu\mathrm{g\,L^{-1}}$ [*e.g.*,

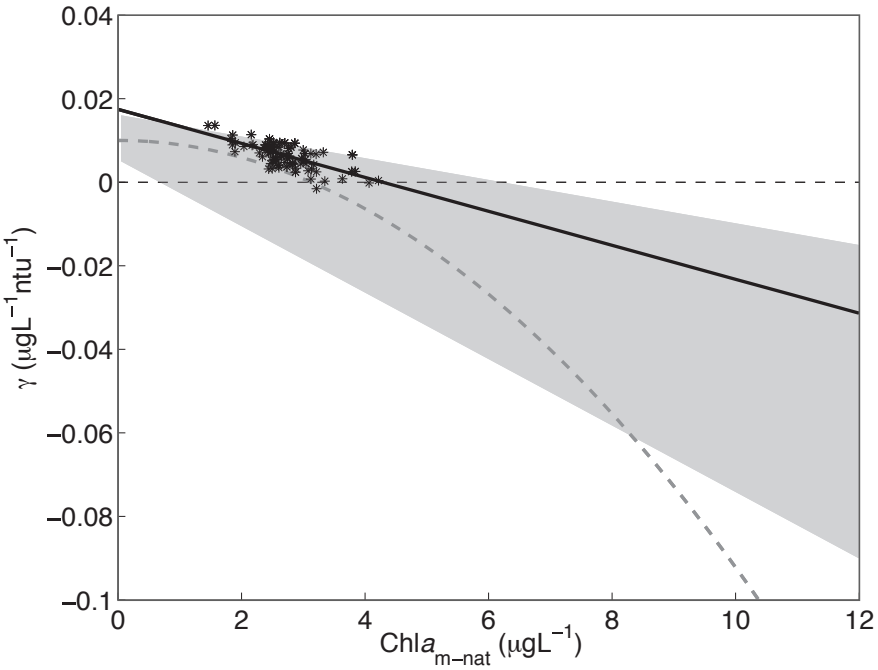

Figure 1.8: Field-derived τChla_{raw} regression slopes γ versus Chl$a_{\mathrm{m,nat}}$(asterisks). The solid line is the least-squares fit, r^2 = 0.48 $p < 0.001$, slope (β field) = -0.004 $\pm$ 0.002 μg L^{-1} ntu^{-1}, intercept (α_{field}) = 0.017 μg L^{-1}. The gray shaded region indicates the laboratory γ range with linear fits (n = 1) to the bubbles and sand tests, and the gray dashed line indicates the quadratic fit to the bubbles laboratory test (see Fig. 6). The black dashed line at $\gamma = 0$ indicates the border where τ-induced enhancement ($\gamma > 0$) and suppression ($\gamma < 0$) are dominant.

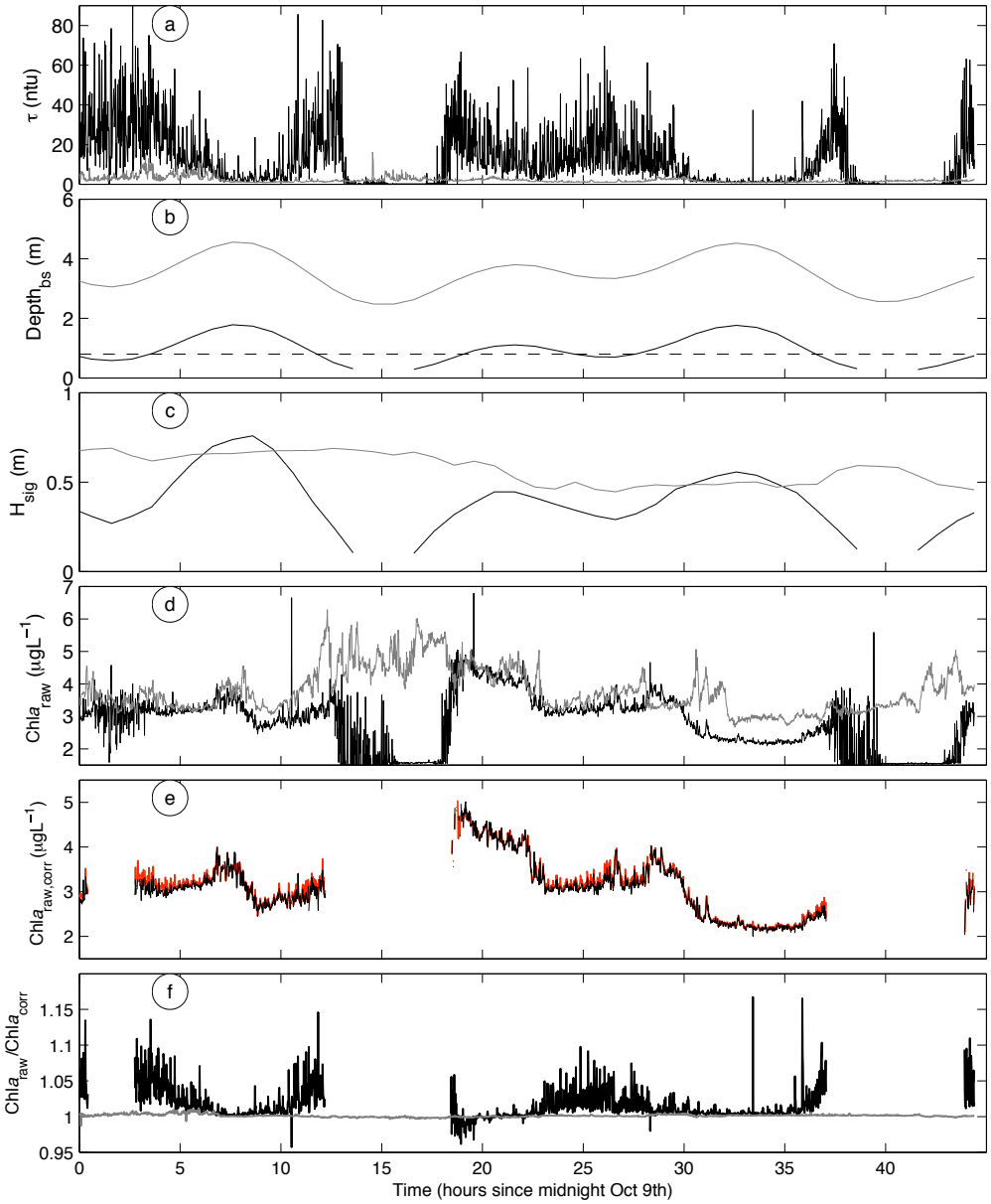

Figure 1.9: (a) Turbidity τ, (b) Depth_{bs}, distance instrument is below mean sea surface (dashed line is 1 m), (c) significant wave height H_{sig}, (d) unprocessed Chl a_{raw} (e) surfzone Chl a_{raw} (de-spiked, observations within 1 m of the surface removed, black) and Chl a_{corr} (red), and (f) Chl a_{raw}/Chl a_{corr}; all versus time for 48 hrs. Gray (black) lines correspond to data seaward of (within) the surfzone.

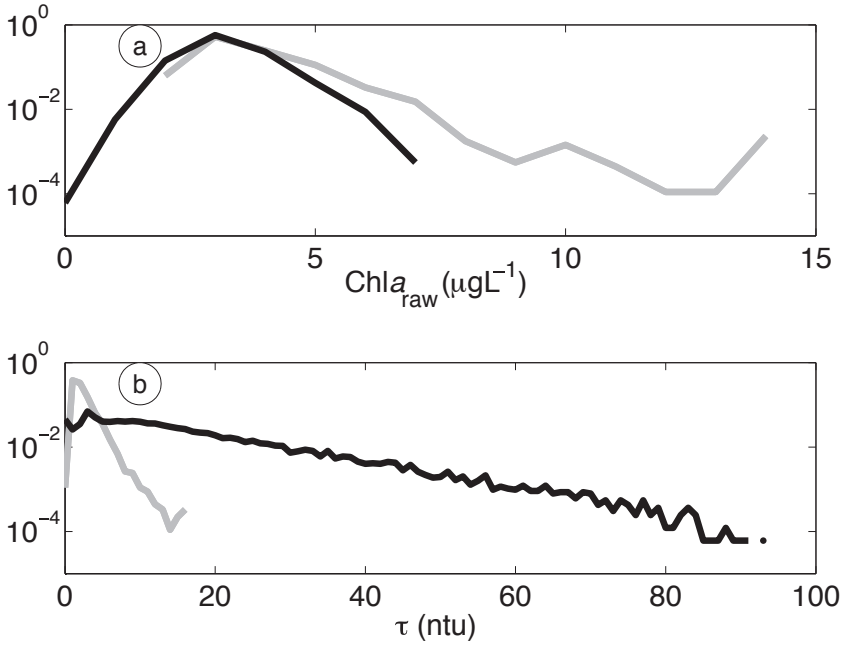

Figure 1.10: Probability density function of (a) de-spiked Chl a_{raw} and (b) turbidity for all field data (∼500 h) inside (black line) and outside (gray line) the surfzone.

Kudela and Cochlan, 2000]. Under these circumstances, a more detailed investigation of the non-linear relationship between Chl a_{true} and γ (see Fig. 1.6) is required.

Sudden, intense appearances of specific species of phytoplankton are known as harmful algal blooms (HABs) because of toxins [*e.g.*, emphPseudonitzchia spp. *Sayce and Horner*, 1996], mechanical damage [*e.g.*, *Chaetoceros* spp. *Tester and Mahoney*, 1995] or anoxia [*e.g.*, *Ceratium* spp. *Mahoney and Steml*, 1979] associated with them. The greatest ecological and economic costs incurred by HABs are observed in nearshore environments where benthic populations and aquaculture are exposed. Satellite-derived Chl *a* estimates are commonly used for HAB monitoring. *Pfister et al.* [2007] compared Chl *a* data from SEAWIFS satellite measurements and a flow-through WETStar fluorometer moored within a tide pool (1.1 m total depth) at Tatoosh Island, Washington. Despite various quality controls, remotely sensed Chl *a* and moored Chl *a* were poorly correlated. *Pfister et al.*

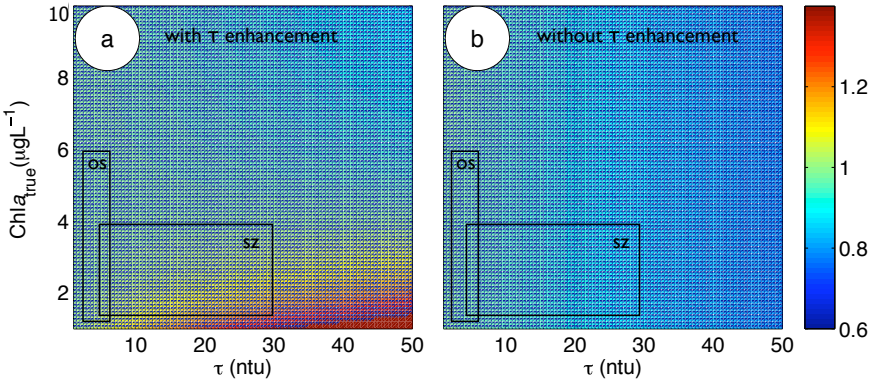

Figure 1.11: Predicted Chl a_{raw}/Chl a_{true} ratio with field-derived parameters (n = 1, α_{field} and β_{field}) for ECO Triplet fluorometers over a range of Chl a_{true} and τ values with τ enhancement (A) and without τ enhancement (B) due to emitted τ interference. The white boxes represent the ranges of 90% of Chl a_{raw} and τ measurements taken within the surfzone (SZ) and seaward of the surfzone (OS) during the field experiment.

[2007] suggested a variety of explanations that may have contributed to the poor correlation. An additional explanation for the poor correlation may be the turbidity-induced error in this shallow nearshore environment (see Appendix C for bubble-induced Chl a_{raw} error with a WETStar fluorometer). This poor correlation emphasizes the importance of extensive comparisons between satellite and *in situ*monitoring stations, and also the necessity for improved understanding of the potential instrument response in these sometimes turbid environments.

1.6 Comments and Recommendations

The effect of bubble- and sand-generated turbidity on measured Chl a fluorescence has been estimated for WET Labs ECO Triplet fluorometers using both laboratory tests and field observations. The results are summarized as follows: 1) Sporadic spikes in Chl a_{raw} (in lab and field) are common under turbid conditions and can be removed. 2) For low Chl a_{true} concentrations ($< 4\ \mu\text{g}\,\text{L}^{-1}$), turbidity enhances the Chl a_{raw} signal by scattering

a fraction of the emitted τ light into the Chl *a* detector (mechanism A, Fig. 1.1a). For Chl $a_{\text{true}} > 4\ \mu\text{g L}^{-1}$, turbidity reduces Chl a_{raw} relative to Chl a_{true} by scattering or absorbing emitted and fluoresced light before detection (mechanism B, Fig. 1.1b). Laboratory tests indicate that the presence of bubbles or sand (after de-spiking) induces a false Chl a_{raw} signal of up to 1 $\mu\text{g L}^{-1}$ in Chl *a*-free water, and Chl a_{raw} suppression of up to 40% (in water with non-zero Chl *a*) at typical surfzone turbidity levels. 3) In general, Chl a_{raw} is more affected by bubble-generated turbidity than by sand-generated turbidity for both mechanism A and mechanism B, but particularly at high Chl a_{true} when mechanism B dominates. 4) A linear (n = 1) model for the τ-Chl a_{raw} slope (γ) best represents the limited range of Chl a_{raw} observed in the field. The dependence of γ on Chl a_{true} ($\sim$ Chl $a_{\text{m,nat}}$) is consistent between lab and field observations, suggesting that the laboratory tests were representative of field surfzone conditions. Although a quadratic (n = 2) model best described the laboratory tests with bubble-induced turbidity, a linear model was the most appropriate for our limited field data set. 5) This τ-Chl a_{raw} model can be used to approximately correct data and to estimate error bounds for Chl a_{true} less than 10 $\mu\text{g L}^{-1}$. Observations over a greater range of Chl a_{true} are required before extrapolating the linear model for γ to correct high Chl a_{raw} concentrations. 6) Rhodamine-WT dye generates a strong false Chl *a* signal and therefore precludes reliable coincident measurements of Chl *a* (mechanism C, Fig. 1.1c, Appendix A). 7) Incident irradiance may enhance Chl a_{raw} less than 1 m below the surface (mechanism D, Fig. 1.1d, Appendix B). 8). Bubble-induced turbidity generated qualitatively similar suppression (mechanism B) in a single-channel, flow-through Wetstar fluorometer (Appendix C), indicating that this effect applies generally to other fluorometers, not just the ECO Triplet. Caution is recommended in interpreting *in situ* Chl a_{raw} data from turbid environments.

Table 1.1: Some commercially available fluorometers for Chl a and/or τ measurements.

Manufacturer	*Model*	*Single/Multichannel*
WET Labs	ECO FL	Single Channel
	ECO FLNTU	Multichannel
	ECO Triplet	Multichannel
Turner Designs	Cyclops-7	Single Channel
	SCUFA	Multichannel
YSI Hydrodata	Optical probe	Single Channel
	Multiparameter optical system	Multichannel

1.7 Appendix A: The effect of Rhodamine-WT dye on Chl a_{raw}

During several days of the field experiment, Rhodamine-WT dye was released in the surfzone. Lab experiments were performed to assess the effect of fluorescent dye on Chl a_{raw} (mechanism C, Fig. 1.1c), and the viability of using Chl a_{raw} fluorometer data during this time period. 15 L buckets were filled with seawater (nominal 2 μm filtered) of low Chl a_{raw} concentration (0.6 $\mu\mathrm{g\,L^{-1}}$) and varying dye concentrations (25, 55, 110 and 220 ppb). Significant errors in Chl a_{raw} occur when dye is present (Fig. 1.12). Rhodamine-WT fluoresces at a broad range of wavelengths (Wilson et al. 1986), leading to some fraction of dye fluorescence detected as Chl a_{raw} (mechanism C). Chl a_{raw} increased linearly with dye concentration giving Chl a_{raw} as large as 30 $\mu\mathrm{g\,L^{-1}}$. The regression slope between Chl a_{raw} and dye is 0.13 $\pm$ 0.01 $\mu\mathrm{g\,L^{-1}}$ppb-1 and the percent variance described.

1.8 Appendix B: The effect of backscattered ambient sunlight on Chl a_{raw}

Ambient sunlight in the water column may enhance Chl a_{raw} (mechanism D, Fig. 1.1d). On a cloudless sunny day, SCUBA divers holding downward-facing (vertical) ECO Triplet fluorometers took three measurements of Chl a_{raw} in an area of direct sunlight, and three in an adjacent (10 m distant) shady area under the Scripps pier (La Jolla, CA, USA). Chl a_{raw}

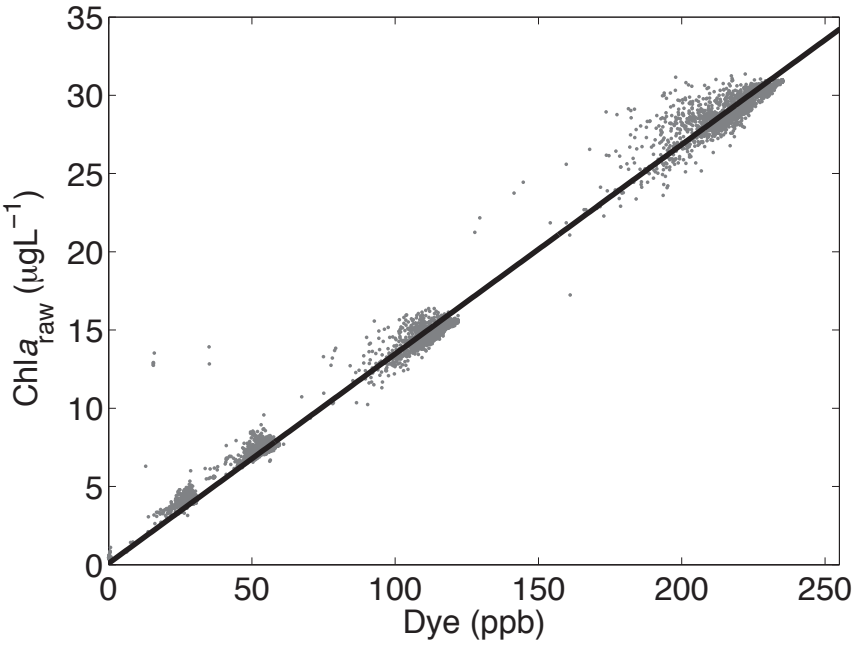

Figure 1.12: Chl a_{raw} with Chl $a_{\text{true}} = 0.6\ \mu\text{g}\,\text{L}^{-1}$ versus Rhodamine-WT dye concentration (gray points). The black line is the linear fit (slope = $0.13 \pm 0.01\ \mu\text{g}\,\text{L}^{-1}\text{ppb}^{-1}$, $r^2 < 0.9$ $p < 0.001$).

was measured at 0.2, 2, and 4 m below the surface (in 6 m total water depth). The mean and standard deviation of Chl a_{raw} was calculated at each level (Table **??**). Over a 30 min period, 3 subsurface positions were sampled at the two horizontal locations (light, shade), alternating between light and shade every two minutes.

The ratio Chl a_{raw} (sun) to Chl a_{raw} (shade) was significantly different than unity (two-tailed t-test) at 0.2 m below the surface. Here, sunlight induced a Chl a_{raw} enhancement of 21 ± 6 % over the Chl a_{raw} measured in the shade. The sun/shade bias decreased with depth below the surface as the ambient sunlight intensity, particularly red wavelengths, decayed. At 2 m and 4 m below the surface, the ratio was not significantly different than unity (two-tailed t-test). Decreases in sun-shaded fluorescence are not due to physiological adaptation to high light conditions [*e.g.*, nonphotochemical suppression, NPQ *Falkowski and Raven*, 1997; *Muller et al.*, 2001], as NPQ *increases* Chl *a* fluorescence in low irradiance. Instead, the measured surface sun/shade bias was likely created by scattered light from the broad sunlight spectrum entering the fluorescence detectors (mechanism D, Fig. 1.1d).

1.9 Appendix C: Effect of bubbles on Chl a_{raw} from a single-channel fluorometer

The effect of bubble-generated τ on Chl a_{raw} was explored in the laboratory with a single-channel WET Labs WETStar flow-through Chl *a* fluorometer (460/695 nm excitation/emission wavelengths, 0 to 150 μg L^{-1} range). Turbidity was measured by a Turner SCUFA instrument with a flow-through cap (545 nm wavelength, 0.03 to 100 ntu range, www.turnerdesigns.com). The Chl *a* sensor, enclosed in the WETStar housing, was not contaminated by the τ emitter enclosed inside the SCUFA. Turbidity and Chl a_{raw} were sampled at 5 Hz. Tests were performed with Chl a_{true} = 0.2, 1.5, 4 and 10 μg L^{-1}. As with the ECO Triplet, the WETStar Chl a_{raw} was linearly correlated with τ (Fig. 1.13), and the τ- Chl a_{raw} regression slope γ (1.1) depended linearly on Chl a_{true}, consistent with α = 0

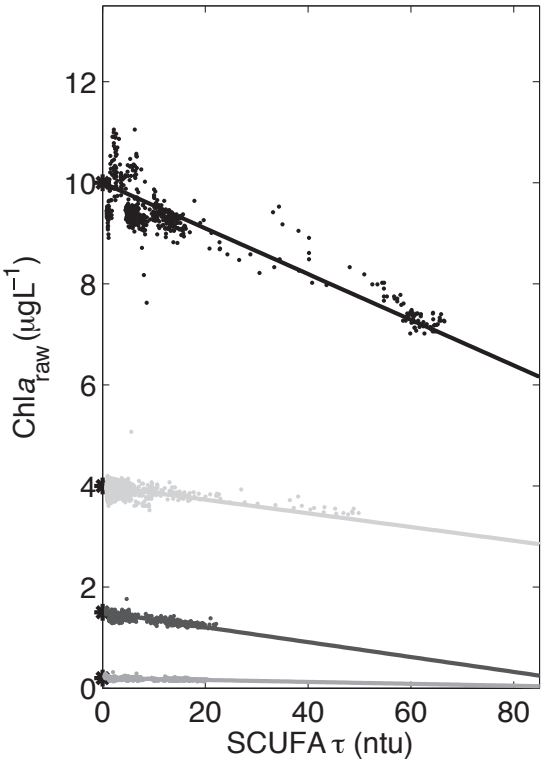

Figure 1.13: WETStar Chl a_{raw} versus bubble-induced turbidity (τ) in seawater with 4 known Chl a_{true} concentrations (black asterisks on vertical axis corresponding to 10, 4, 1.5 and 0.2 μg L^{-1}). Solid lines are linear fits with intercept set equal to Chl a_{true}. The fraction of variance described by each fit (in ascending Chl a_{true} order) is r^2 = **0.77, 0.35, 0.44, 0.10 respectively. The r^2 in bold type correspond to $p < 0.001$.**

in (1.3). The SCUFA and ECO Triplet τ sensors have different optics and thus different responses to bubbles and sand, precluding quantitative comparison of the γ-Chl a_{true} relationship (i.e, β) between the two instrument pairs. However, the results suggest that the model (1.2) may apply broadly to single-channel, multi-channel and flow-through fluorometers.

1.10 Acknowledgements

B. Woodward, B. Boyd, K. Smith, D. Darnell, I. Nagy, M. Mckenna and M. Rippy assisted in testing the fluorometers and collecting field observations. SIO Hydro Lab staff and WET Labs personnel provided advice during laboratory tests and an anonymous reviewer provided very helpful comments on the manuscript. This research was supported in part by California Sea Grant, NOAA, California Coastal Conservancy, and ONR. Sea Grant support was through the California Sea Grant College Program Project #R/CZ-196, through NOAA's National Sea Grant College Program, U.S. Dept. of Commerce. The statements, findings, conclusions and recommendations are those of the authors and do not necessarily reflect the views of California Sea Grant or the U.S. Dept. of Commerce.

Chapter 2

Physical and biological processes underlying the sudden surface appearance of a red tide in the nearshore.

2.1 Abstract

The sudden appearance at the surface of an alongshore-parallel band of red tide near Huntington Beach, California, USA is described in high spatial and temporal resolution using novel instrumentation including a global positioning system (GPS) -tracked jetski. The scale of the surface chlorophyll*a* (Chl *a*) band was small ($\sim$200 m cross-shore) and ephemeral (3 h) compared with the subsurface extent of the red tide ($\sim$2 km, $>$ 7 days). The red tide was dominated by the regionally common dinoflagellate *Lingulodinium polyedrum* (F. Stein) and had developed as a subsurface Chl *a* layer during the 7 days prior to the surface appearance. A few hours before the surface appearance, a subsurface patch of elevated Chl *a* ($> 30\ \mu g\,L^{-1}$) was observed in 13 m total depth in the trough of a shoreward-

propagating internal wave, consistent with dinoflagellate vertical swimming interacting with the internal wave-driven convergence. Internal wave-breaking induced vertical mixing in $\sim$ 8 m water depth vertically spread the Chl$a$ patch to the surface, creating the alongshore surface band approximately 500 m from shore. Both the subsurface Chl$a$ patch and the surface Chl$a$ band were prevented from entering the surfzone by a density barrier of warm water adjacent to the beach. These high-resolution observations emphasize the role of nearshore physical dynamics in controlling the duration and intensity of red tide exposure to coastal habitats.

2.2 Introduction

Intense phytoplankton blooms (red tides) and harmful algal blooms (HABs) in the nearshore ($<$ 20 m depth), cause losses of millions of dollars annually to aquaculture [*Alonso-Rodrgueza and Pez-Osuna*, 2003], threaten marine mammal and human health [*Anderson*, 1997], and inhibit beach recreation [*Backer et al.*, 2003]. An understanding of the mechanisms controlling the intensity and timing of red tides is particularly critical in the nearshore (depth $<$ 20 m) and surfzone (depth $<$ 3 m) where the often densely populated benthic habitats are vulnerable to red tide exposure. HABs often begin as thin subsurface layers ['cryptic blooms *McManus et al.*, 2008], invisible to satellites and visual inspection. Furthermore, their surface expression is often patchy in time and space, not reflecting the subsurface patterns, making effective monitoring a challenge [*Anderson*, 1997].

Interpretation of surface or near-surface data must be coupled with an understanding of the physical mechanisms that control the vertical and horizontal distributions of chlorophyll$a$ (Chl$a$) in the water column. Over time scales $<$ 1 day, changes in phytoplankton biomass due to growth are typically small: with a net growth rate $\mu \sim 0.29$ d^{-1}, the red-tide forming dinoflagellate *Lingulodinium polyedrum* would show an increase of only $\sim$ 1.3x over 1 d [*Sullivan and Swift*, 2003]. On the other hand, Chl$a$ variability driven by ad-

vection for example, tidal currents and stirring [*Cloern and Dufford*, 2005], internal tides [*Kamykowski*, 1974] or internal wave-induced circulation in combination with swimming or sinking of cells [*Lennert-Cody and Franks*, 1999, 2002] has been shown to cause increases $>$ 2x over time scales of hours or less. Mechanisms that concentrate or advect red tides over short space and timescales may carry severe consequences. For example, mussels exposed to high concentrations of HAB toxins may surpass quarantine limits within only one hour, whereas prolonged exposure to lower concentrations may not be harmful [*Bricelj et al.*, 1990].

The study described here presents high spatially and temporally resolved observations of a nearshore red tide and explores the physical dynamics underlying a sudden surface appearance of a dense red-tide band. The surface expression of the red tide was visible from the beach as a brown streak 500 m from shore and extending $>$ 1 km alongshore (Fig. 2.1). The observations were collected during the Huntington Beach experiment (HB06) in fall 2006. Within the 1 month HB06 study period, an intense subsurface layer of the dinoflagellate *L. polyedrum* developed over the 7 days before its peak on 12 October. On 12 October, the red-tide layer was mapped repeatedly using several complementary techniques. The measurements revealed that in the hours preceding the mid-day appearance of the surface Chl$a$ band, an intense subsurface Chl$a$ patch formed within a shoreward-propagating supertidal (period $<$ semidiurnal) internal wave trough. The location and intensity of the patch was consistent with concentration increases driven by depth-keeping swimming of the dinoflagellates in the internal wave-induced convergence. The surface alongshore-parallel Chl$a$ band did not form directly through the interaction of the internal wave convergence and vertical swimming [*see Kamykowski*, 1974; *Lennert-Cody and Franks*, 1999, 2002]. Instead, upon arrival in shallow water (depth $<$ 13 m), internal wave breaking spread the intense subsurface Chl$a$ patch vertically, forming the visible band of surface Chl$a$ just seaward of the surfzone. After the surface band appearance, Chl$a$ was inhibited from entering the surfzone by a warm-water plume transported from a nearby marsh by wave-driven alongshore currents.

Figure 2.1: Un-retouched photograph of a brownish alongshore-parallel band of red tide (arrow) approximately 500 m offshore, taken from the beach in early afternoon on 12 October. The small breaking surface wave in the foreground is near the beach, and the 5 m long CTD+Chl a cast boat is offshore.

2.3 Methods

The nearshore HB06 field experiment was conducted at Huntington Beach, California, USA, from 15 September to 17 October 2006, within the framework of the larger scale Southern California Coastal Ocean Observing System (SCCOOS) and United States Geological Survey (USGS) programs. Here data are presented from 5 to 16 October with a focus on the dynamics of 12 October when the red tide appeared at the surface. Observations spanned 0.5 km alongshore (y) and 4 km offshore (x) to 25 m depth (Fig. 2.2). The mean (tidally averaged) water depth is denoted as H, and the vertical coordinate z is positive upward, with $z = 0$ m at the tidally averaged surface.

2.3.1 Jetski Surface Maps

Five quasi-synoptic maps of near-surface Chl a, turbidity and temperature (T) were constructed from data acquired at 45 min intervals between 12:00 and 15:00 h with a flow-

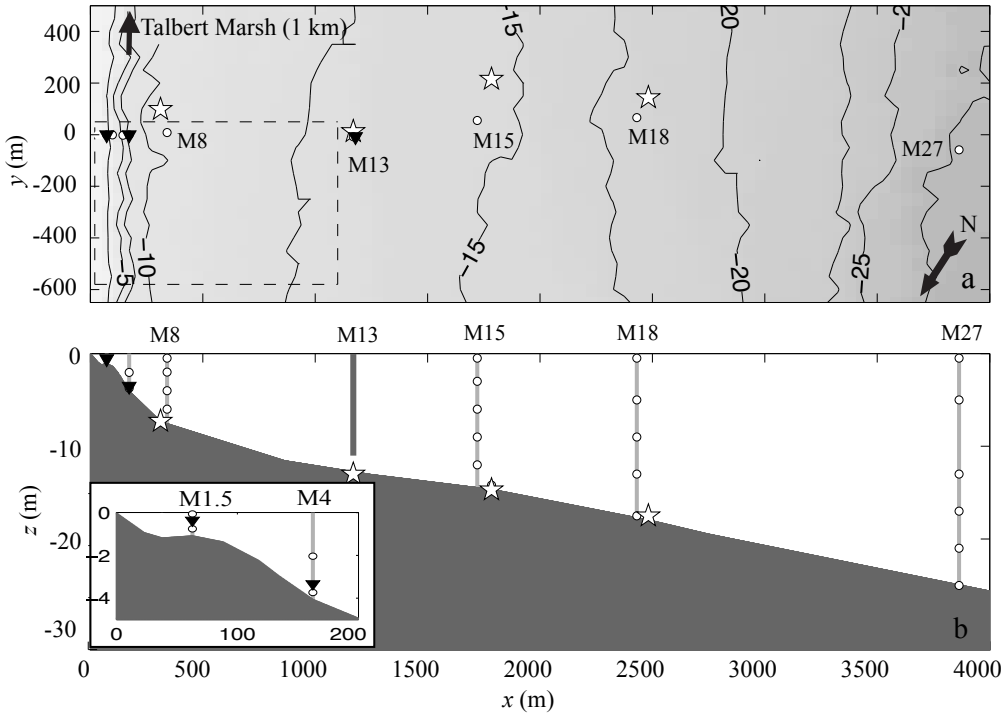

Figure 2.2: Schematic of HB06 instrumentation: (a) plan view of bathymetry contours vs. the alongshore (y) and cross-shore (x) coordinates and (b) cross-shore transect of bathymetry (dark shading). The vertical coordinate is z, with z = 0 m at the tidally averaged surface and positive upward. Moored temperature strings (circles, M8 to M27) were located at total depths H = 8, 15, 18, and 24 m. A vertically profiling CTD+Chl$a$ wirewalker (M13) was located at H = 13 m. Bottom-mounted ADCPs (stars) were located near moorings M8, M13, M15, and M18. Fixed frames within the surfzone (M1.5) at H = 1.5 m and seaward of the surfzone (M4) at H = 4 m measured Chl$a$ (triangles), T (circles), wave height, and currents (*see* inset in (b)). A GPS-tracked jetski measured surface T and Chl$a$ within the black dashed box in (a) and small boat (CTD+Chl$a$) completed transects during daylight hours from H = 5 to 60 m (8 km offshore). The Talbert Marsh outlet is located 1 km south of the instrument transect.

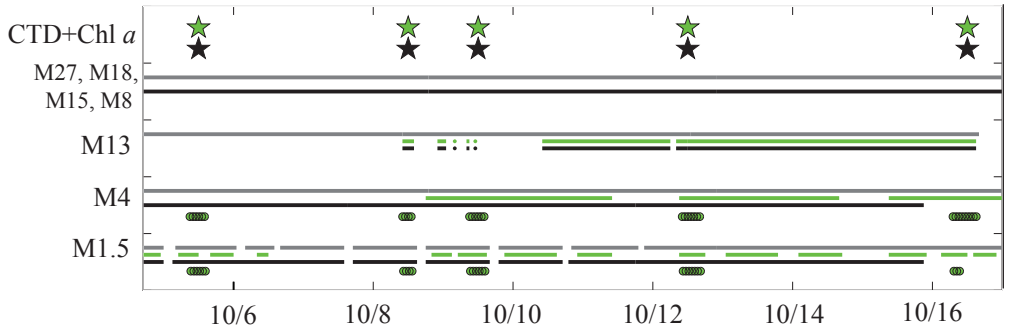

Figure 2.3: Gantt chart indicating velocity (gray), T (black) and Chl$a$ (green) data coverage between 05 October and 16 October. Stars indicate CTD+Chl$a$ transect days and circles indicate bottle samples for phytoplankton identification.

through sampling system mounted on a Global Positioning System (GPS) -tracked jetski (Clark et al. 2009). The jetski was driven on 1 km long cross-shore transects between the shoreline and $\sim$13 m depth with 8 transects distributed over 600 m alongshore (dashed box in Fig. 2.2a). Jetski data acquired on October 5 and 9 lacked concurrent CTD+Chl$a$ transects and are not discussed.

2.3.2 CTD+Chl*a* Casts

Transects of CTD (Seabird 19) and flow-through Chl$a$ fluorometer (WET Labs WET-Star) profiles (x,z) spanning 6 km cross-shore (from H = 40 m to H = 4 m) were conducted between 9:00 and 11:30 h once per day on 05, 07, 08, 12 and 16 October. In addition, on 12 October, a series of 5 short cross-shore transects spanning 1 km (H = 13 m to H = 4 m) were conducted between 12:00 and 15:00 h, concurrent with jetski surface mapping. Profile data were averaged into 1 m vertical bins. The jetski-derived surface transects (x,y) and CTD+Chl$a$-derived cross-shore transects ((x,z) were objectively mapped with a skill threshold of 0.95 and a signal-to-noise ratio of 0.9 [*Bretherton et al.*, 1976].

2.3.3 Moorings

Moorings were deployed on a 4 km long cross-shore transect at mean (tidally-averaged) water depths H = 8, 15, 18, and 27 m (moorings M8, M15, M18, M27 in Fig. 2.2) and instrumented with 4 to 6 Star-Oddi (T only) or Sea Bird MicroCAT (S and T) instruments sampling at 3 min intervals between October 05 to October 16 (Fig. 2.3). A wirewalker, a wave-driven vertically profiling platform [*Rainville and Pinkel*, 2001], was deployed at H = 13 m (M13 in Fig. 2.2ab), and instrumented with a CTD (Seabird 49, sample rate 16 Hz) and Chl$a$ fluorometer (WET Labs ECO Triplet, sample rate 16 Hz). Vertical CTD+Chl$a$ wirewalker profiles at M13 were completed approximately every 2 min; data were averaged every 0.1 m in z and interpolated onto regular 4 min intervals. The M13 wirewalker was intermittently operational, with $> 90\%$ data coverage between October 10 and October 16 (Fig. 2.3). Cross-shore (u) and alongshore (v) currents measured with Acoustic Doppler Current Profilers (ADCPs) deployed at the base of moorings M13 (600 kHz), M15 (600 kHz), and M18 (600 kHz) were averaged to 6 min intervals with 1 m vertical bins. A bottom-mounted Nortek Aquadopp at M8 (2000 kHz) sampled every 2.5 min with 0.5 m vertical bins. These current meters were consistently operational from October 5 to October 16 (Fig. 2.3).

2.3.4 Surfzone Frames

Two fixed frames with Acoustic Doppler Velocimeters, pressure, and temperature sensors (sampled at 8 Hz, 8 Hz, and 0.2 Hz, respectively) were deployed between 5 and 16 October on a cross-shore transect spanning 160 m from near the shoreline to 4 m water depth. One frame was placed just seaward of the surfzone (M4 at H = 4 m) and one within the surfzone (M1.5 at H = 1.5 m, *see* inset in Fig. 2.2). Instruments at M1.5 were nonfunctional during exposure at low tide (Fig. 2.3). WET Labs ECO Triplet fluorometers measuring Chl$a$ (sampled at 0.25 Hz) were mounted on M4 and M1.5 facing 30deg from downward, nominally 0.5 m above the seafloor. These fluorometers were repeatedly de-

ployed for 72 h periods with approx 12 h turn-around time (Fig. 2.3). A correction for the data bias induced by surfzone turbidity was applied to the ECO Triplets (Omand et al. 2009).

2.3.5 Water Samples

During most CTD+Chl*a* casts, water samples (for Chl*a* analysis and phytoplankton cell counts and identification) were collected near the bottom with a messenger-tripped Niskin bottle mounted 1 m above the CTD, and at the surface by hand. Water samples were also collected near the surface every 20 min on 12 October from 9:00 to 15:00 h near M1.5 and M4 (Fig. 2.3). Samples for taxonomic identification were preserved by transferring 100 mL of raw seawater to a glass Wheaton bottle and combining with 10 mL buffered 37% formaldehyde. The preserved samples were analyzed with the Utermöhl settling method (Utermöhl 1958) and inspected at 16$\times$ magnification using a light microscope. All visible cells (> 5 μm) were enumerated and identified to a genus or species level when possible.

2.3.6 Nonphotochemical Quenching Correction

Nonphotochemical quenching (NPQ) reduces Chl*a* fluorescence in high light conditions [*Keifer*, 1973; *Falkowski and Raven*, 1997; *Muller et al.*, 2001]. NPQ corrections, derived from continuous profiles of Chl*a* at M13 (Fig. 2.2) and surface irradiance (measured with a Davis Vantage Pro Plus cosine pyranometer), were applied to all in situ Chl*a* measurements (*see* Appendix). The NPQ correction was small and does not affect the results. The NPQ correction is generally small, smaller than 10% at the 17 $^{\circ}$C isotherm at M13, and is occasionally as large as 50% at the surface at noon. Similar results are obtained with and without the NPQ correction.

2.4 Results

2.4.1 Subsurface Red Tide Observations

The subsurface Chl$a$ distributions could be separated into two relatively distinct features: an offshore deep Chl$a$ maximum (DCM) formed mainly by diatoms, and an inshore subsurface layer formed by dinoflagellates (Table 1). Chl$a$ within the DCM increased from a maximum of 6 μg L^{-1} on 05 October to 10 μg L^{-1} on 12 October (Fig. 2.4). The DCM lay between 13 - 16 °C, and spanned at least 6500 m cross-shore. Concurrent CTD + Chl a glider surveys conducted approximately 10-30 km offshore also showed an increase of mean subsurface Chl$a$ between 05 and 12 October, but with much lower maximum concentrations (1.5 to 2.5 μg L^{-1}, Todd et al. 2009). The *L. polyedrum* red tide initially developed in a nearshore subsurface layer spanning 2 km cross-shore. The region of this layer with Chl$a > 10$ μg L^{-1} between the 16 °C and 17 °C isotherms will be referred to as the Chl$a$ layer. Nearshore Chl$a$ was generally low on 05 October (maximum 4.5 μg L^{-1}, Fig. 2.4a) increasing to 13 μg L^{-1} by 08 and 09 October (Fig. 2.4b,c), and peaking at $\sim$ 34 μg L^{-1} on 12 October. By 16 October, the Chl$a$ layer concentrations decreased to 12 μg L^{-1} (Fig. 2.4e).

Though alongshore advection of Chl$a$ gradients may have contributed to the observed increase in concentration in the Chl$a$ layer between 05 and 12 October, a net growth rate of only ~ 0.23 d^{-1} would also account for these changes. This net growth rate is quite plausible for *L. polyedrum* [*Sullivan and Swift*, 2003] and would lead to a 10-fold increase in Chl$a$ over a week, consistent with observations (Fig. 2.4). Over a day such a growth rate would lead to only a 1.3-fold increase.

Conditions on 12 October, the focus of this study, were typical of a fall day at Huntington Beach: winds were weak, blowing slightly offshore in the morning with a northwest 3 m s^{-1} breeze in the afternoon. The surface water temperature was approximately 17.5 °C, dropping to 14 °C at the base of the thermocline at $\sim$ 20 m (Fig. 2.4d). The phytoplankton taxonomic composition was strikingly different between nearshore and offshore

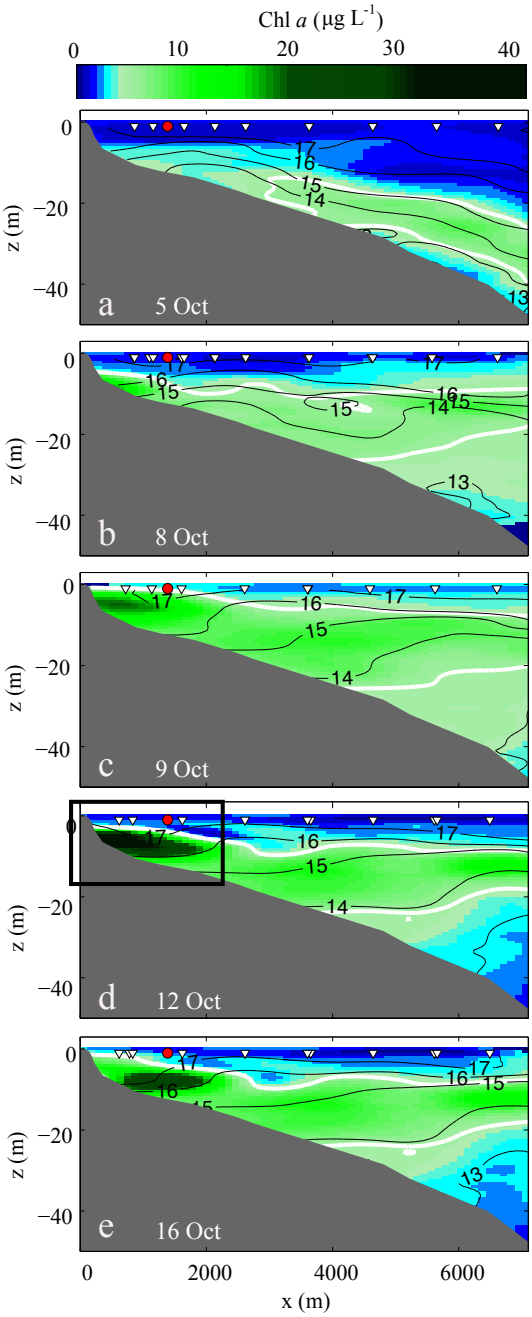

Figure 2.4: Cross-shore sections (x,z) of Chl$a$ (μg L^{-1}, colors) and T (°C, black contours) obtained between 09:00 and 11:30 h on select days between 05 October and 16 October. The red circle is M13 surface location and the white triangles indicate CTD+Chl$a$ cast locations. The white line traces the 4 μg L^{-1} Chl$a$ contour. The black box (in d) indicates the nearshore red tide focus area on 12 October.

Table 2.1: Phytoplanktonic genera present on 12 October within the nearshore (H $<$ 20 m) and offshore (H $>$ 20 m) regions. The total number of cells counted within each region is *n*. Dinoagellates are identied in bold type.

Genus	Nearshore (*n* = 11949)	Offshore (*n* = 11296)
Lingulodinium	**71.6**	**4.9**
Chaetoceros	6.4	34.8
Asterionella	6.3	32.9
Prorocentrum	**4.6**	**0.9**
Psuedonitzschia	4.3	7.1
Skeletonema	0.6	7.5
Other	6.1	11.9

(Table 1). The nearshore was dominated by a near-monoculture of dinoflagellates ($>$ 70% *Lingulodinium polyedrum*) whereas offshore waters contained a greater diversity of genera, dominated by diatoms from the genera *Asterionella* and *Chaetoceros*. Although less prevalent than on 12 October, *L. polyedrum* cells exceeded 50% in the nearshore on 08, 09, and 16 October.

Diurnal and semi-diurnal frequency fluctuations dominated the current and T variability at moorings M27 to M08 during HB06, similar to prior studies at this location [*Boehm et al.*, 2002; *Noble et al.*, 2009]. On 11 - 12 October, the tidal range was $\pm$0.9 m (Fig. 2.5a). Cross-shore currents at M13 contained both diurnal and semidiurnal baroclinic variability (Fig. 4b), and the Chl$a$ layer repeatedly shoaled from near-bottom to near-surface and back down (Fig. 2.5c). The Chl$a$ layer followed the 16.0 - 17.0 °C isotherms (black contours in Fig. 2.5c) throughout the diurnal cycle, except for a few hours after the 17.5 °C isotherm descended, leaving increased near-surface (z > -5 m) Chl$a$ concentrations ($\sim$ 5 μg L^{-1}) above the 17.5 °C isotherm (e.g., at t = -32, -8, and 14 h in Fig. 2.5c).

At M13 between 10:00 and 12:00 h on 12 October, a Chl$a$ patch (maximum 34 μg L^{-1}) was observed between 5 and 7 m below the surface, at the 17.0 °C isotherm (Fig. 2.6). The onshore currents (u $\sim$ 0.05 m s^{-1} between 10:00 and 12:00 h) between -7 $<$ z $<$ -5 m advected the Chl$a$ patch shoreward. Based on the onshore u over the 2 h M13 patch duration (Fig. 2.6), the high concentration subsurface Chl$a$ patch was estimated to

be 200 m wide across-shore. This region of very concentrated Chl$a$ (> 20 μg L^{-1}) will hereafter be referred to as the Chl$a$ patch.

2.4.2 Surface Red Tide Observations

Five CTD+Chl$a$ cross-shore transects and near-synoptic jetski surveys of surface Chl$a$ and T were conducted on 12 October at 45 min intervals between 12:00 and 15:00 h inshore of M13 (Fig. 2.2). At 12:00 h, a high Chl$a$ concentration (up to 39 μg L^{-1}) layer was located ~ 5 m below the surface (Fig. 2.7a). Surface Chl$a$ and T were spatially homogeneous at 3 μg L^{-1} and 17.7 °C, respectively (Fig. 2.7a,b). Hourly averaged cross-shore currents were ~ 0.03 m s^{-1}onshore near the surface and offshore near the seafloor. The surfzone alongshore current was 0.15 m s^{-1} northward. By 1245 h, a small (~ 10 m cross- and alongshore) patch of approximately 4 μg L^{-1} Chl$a$ appeared at the surface with slightly cooler, 17.5 °C water (Fig. 2.5c). The Chl$a$ at the surface that formed the alongshore parallel streak will be referred to as the Chl$a$ band.

At 13:30 h (Fig. 2.7e,f), the Chl$a$ band had enlarged and intensified to ~ 5 μg L^{-1} near x = 400 m in 17.5 °C water, spanning 100 m across-shore and 250 m alongshore. Near the surfzone (x $<$ 150 m), the water had warmed to 18 °C. The Chl$a$ patch was centered on the 17 °C isotherm directly below the Chl$a$ band, and had increased in thickness. At 14:15 h, the Chl$a$ band had increased to 7 μg L^{-1}, with a cross-shore span of about 200 m (Fig. 2.7g) and visually estimated alongshore length ~ 1 km.

The near-surfzone region continued to warm, and the colder (< 17 °C) surface water at x > 500 m receded offshore (Fig. 2.7h). The Chl$a$ patch continued to spread vertically into warmer 17.5 °C to 18 °C water. Later at 15:00 h, the surface Chl$a$ band had advected slightly offshore with the < 17.5 °C water (Fig. 2.7i,j).

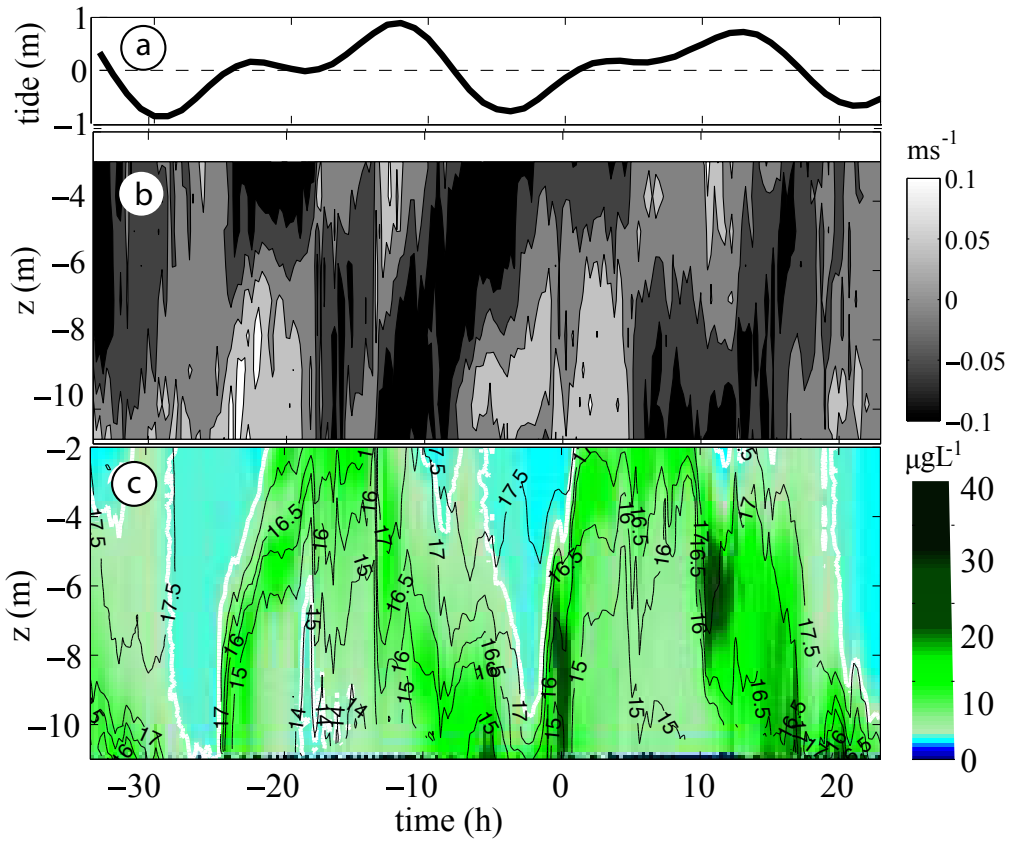

Figure 2.5: Time series (spanning 54 h) at M13 (H = 13 m) of (a) tidal excursion from mean sea level, (b) vertical proles of 15 min averaged cross-shore currents u at M13 (positive = onshore), and (c) 15 min averaged vertical profiles of Chl$a$ (μg L^{-1}, colors) and T ($^{\circ}$C, black contours) at M13. The white curves trace the 4 μg L^{-1} Chl$a$ contour. Time zero is 00:00 h 12 October.

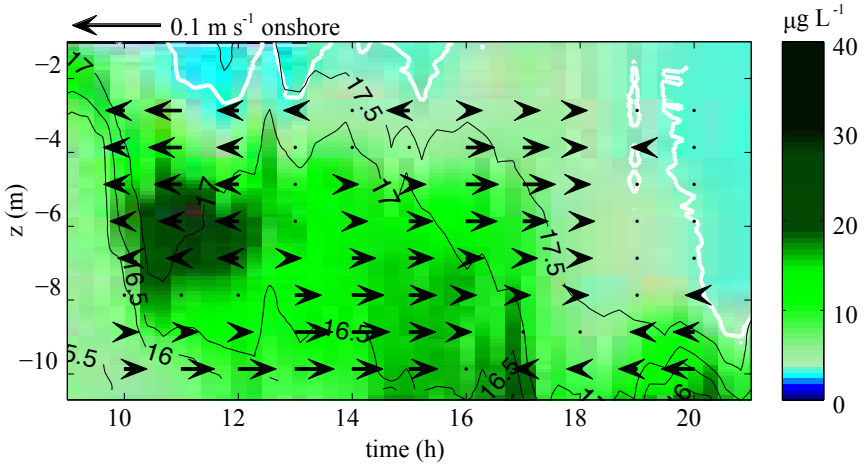

Figure 2.6: Time series (spanning 11 h of the time period in Fig. 5) of 15 min averaged vertical profiles of Chl$a$ (μg L^{-1}, colors) and T (°C, black contours) at M13 (H = 13 m). Time 10 hours corresponds to 10:00 h on 12 October. The hourly averaged cross-shore currents (u) are represented by arrows for $\text{—}u\text{—} \geq 0.01$ m s^{-1}and by black dots where $\text{—}u\text{—} < 0.01$ m s^{-1}. The 15 min averages shown in Fig. 5 crowded the plot blocking the Chl$a$ colors. The white line is the 4 μg L^{-1}contour.

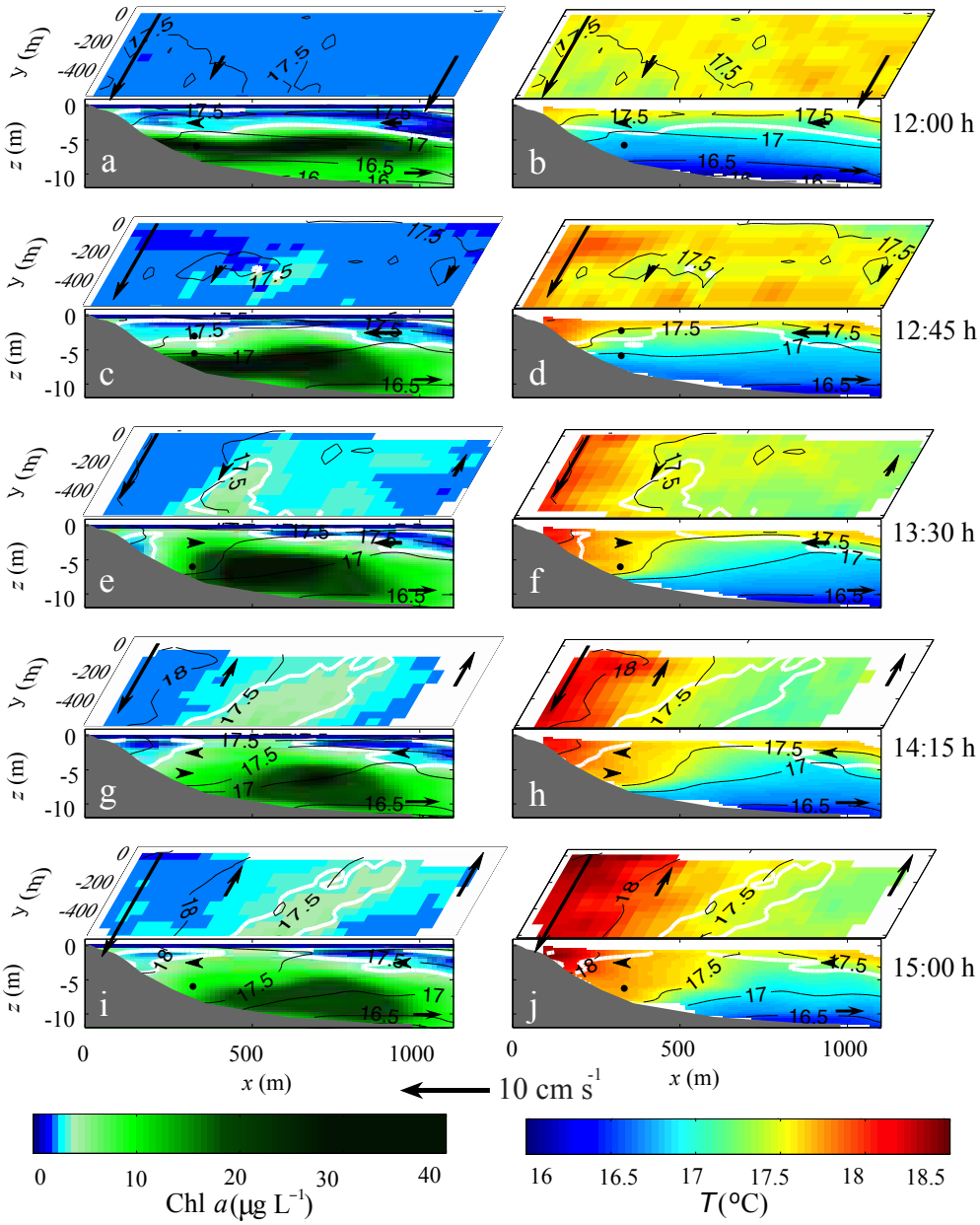

Figure 2.7: Sequential (top to bottom) maps of nearshore Chl$a$ (left) and T (right) on 12 October from jetski-based horizontal (x,y) measurements and CTD+Chl$a$ based cross-shore transect (x,z) measurements. Arrows represent the directions of the near-surface alongshore (at M1.5, M8 and M13) and near-surface ($\sim$ 2 m below mean sea level) and near-bottom ($\sim$ 2 m above the seafloor) cross-shore currents (at M8 and M13 only). The jetski required 30 min to complete the 8 cross-shore transects used for each map, and the centered-time (12:00-15:00 h) is shown to the right of each panel. Each CTD+Chl$a$ transect consisted of 5 or 6 profiles. Black lines are temperature contours. The white line traces the 4 μg L^{-1} Chl$a$ contour.

2.5 Discussion

A dense, nearshore dinoflagellate bloom developed over ~ 7 days in a subsurface layer spanning 2 km in the cross-shore. The bloom was invisible from the surface until 12 October when a small-scale (a few 100 of meters wide) elevated Chl$a$ band surfaced for a few hours about 500 m from the beach. The brief, small scale of the Chl$a$ surface band contrasts which the larger breadth and persistence of the subsurface layer, and was determined by the combination of several physical-biological processes: (1) shoreward propagation of an internal wave trough, (2) local formation of a dense Chl$a$ patch within the trough, (3) internal wave breaking in H $<$ 13 m, (4) wave breaking-induced vertical and cross-isotherm spreading of the Chl$a$ patch, and (5) a warm water density barrier to Chl$a$ entry in the surfzone. Evidence for these mechanisms, and alternate hypotheses underlying each stage are discussed in the following subsections.

2.5.1 Stage 1: Shoreward Propagation of a Supertidal Internal Wave

Estimation of the shoreward propagation speed of a supertidal (period $<$ semidiurnal) internal wave (sIW) provides a prediction of the sIW arrival time in very shallow water. On 12 October between 00:00 h (midnight) and 03:00 h, a mid-water column wave of depression with an amplitude of 5 m was observed at M27 at 05:00 h (star, Fig. 2.8a). The shoreward-propagating supertidal (period $<$ semidiurnal) internal wave (sIW) trough subsequently passed M18 and M15, reaching M13 at 11:00 h (black stars, Fig. 2.8b,c,d). There was no evidence of the sIW trough at M8 (H = 7.8 m) (Fig. 2.8e).

The wave phase speed was calculated as $C_p = \Delta x$ over Δt, where Δx is the cross-shore separation between adjacent moorings, and Δt is the sIW travel time (e.g. time lag between arrivals of the sIW trough, black stars, Fig. 2.8). The sIW travel time Δt is estimated at the lag for maximum correlation ($r^2 > 0.63$, p < 0.001, Table 2) between mid-water column isotherm depth anomalies at adjacent moorings (Lerczak 2000) over a 15 h period (from 00:00 to 15:00 h) that includes the sIW trough (Fig. 2.9a). Assuming a normally incident

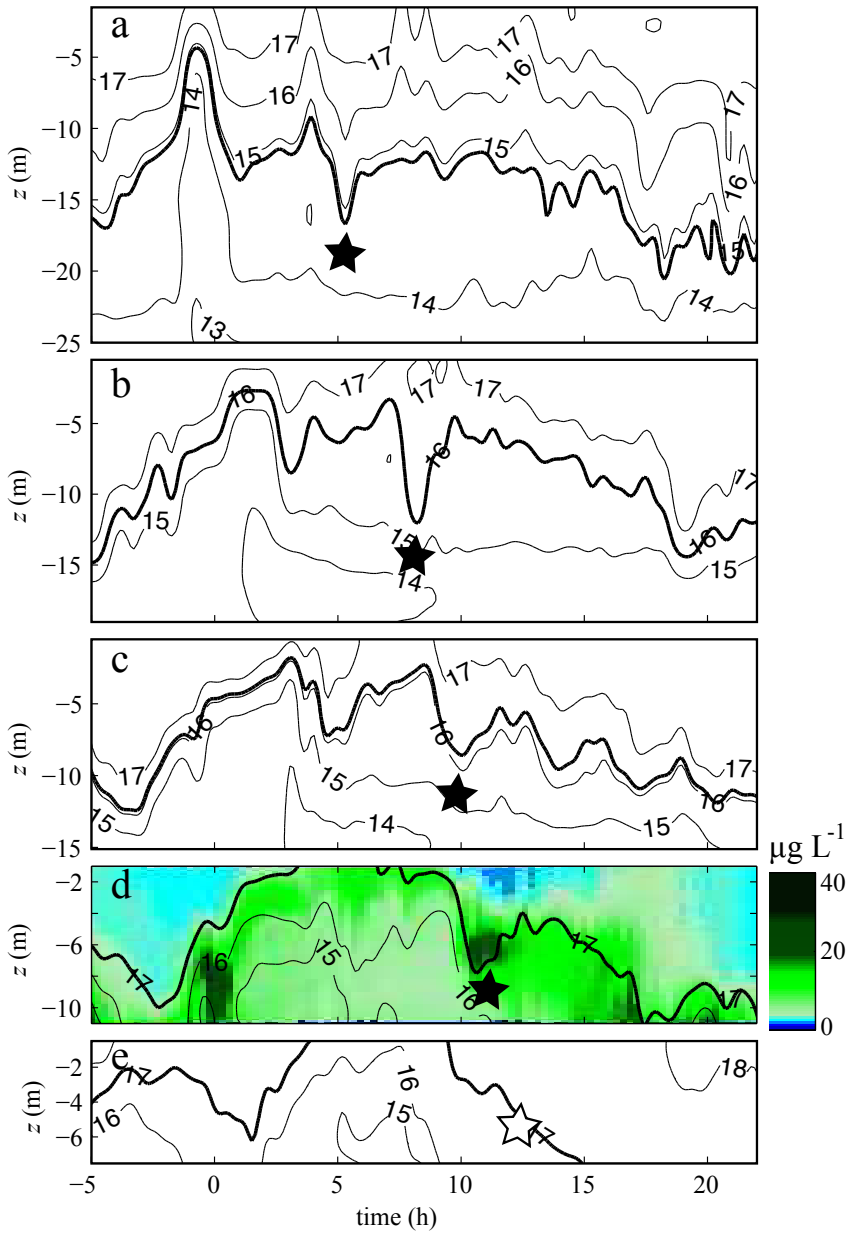

Figure 2.8: Contours of T ($^{\circ}$C) vs. time and z at (a) M27, (b) M18, (c) M15, (d) M13, (e) M8. Black stars represent an internal wave trough propagating onshore. The bold contour is a representative mid-water isotherm. The white star is the trough location at M8 predicted by linear theory. In (d) M13, Chl$a$ (μg L^{-1}) is colored. Time zero corresponds to 00:00 h 12 October.

sIW, the observed cross-shore phase velocity $C_p = \Delta x$ over Δt (where Δx is the cross-shore separation between adjacent moorings) decreased from 0.16 $m\,s^{-1}$between M27 and M18 to 0.12 $m\,s^{-1}$between M15 (black points, Fig. 2.9b). Refraction of the sIW towards normal incidence precludes large angles of incidence. Obliquity of 30 deg from shore-normal causes only a 15% underestimate in C_p (error bars, Fig. 2.9b).

Table 2.2: Separation distance (Δx), time lag maximizing r2 (Δt) and correlation coefficient (r^2) of the sIW depth contours at the midpoint (Midpt.) between adjacent moorings. The observed phase velocity C_p (obs.) = Δx/Δt. At each mooring location, theoretical C_p ($m\,s^{-1}$) from equation (1) and (2) and u_{max} ($m\,s^{-1}$, positive = onshore) above the wave trough. All correlations are significant at the 99% level.

Location	Δx (m)	Δt (h)	r^2	C_p (obs.)	C_p (1)	C_p (2)	u_{max}
M27					0.170	0.174	0.08
Midpt. (M27-M18)	1643	2.9	0.75	0.157			
M18					0.129	0.139	0.07
Midpt. (M18-M15)	715	1.6	0.63	0.120			
M15					0.116	0.116	0.06
Midpt. (M15-M13)	549	1.3	0.79	0.117			
M13					0.100	0.080	0.06

The observed cross-shore variation in C_p is similar to the theoretical dependence on water depth of C_p for linear, long (wavelength $\gg$ water depth) internal waves (IW). With constant buoyancy (N) and wave (Ω) frequencies, the theoretical phase speed (C_p) for a mode 1 cross-shore propagating internal wave *Gill* [1982]

$$C_p = \frac{H}{\pi}\sqrt{N^2 - \omega^2} \tag{2.1}$$

depends linearly on the depth H. The theoretical phase speed C_p was estimated from (1) using the vertically averaged N, calculated from dT over dz adjusted to density. A nominal wave period of 2 h was chosen based on the observed passage time of the sIW depression (*see* Fig. 2.8) to estimate Ω. The buoyancy frequency N (~ 0.02 s^{-1}) was large compared to Ω, so the theoretical C_p was insensitive to the choice of Ω (C_p varied by $< 1\%$ for wave periods between 2 and 12 h). Theoretical C_p are similar for a 2-layer

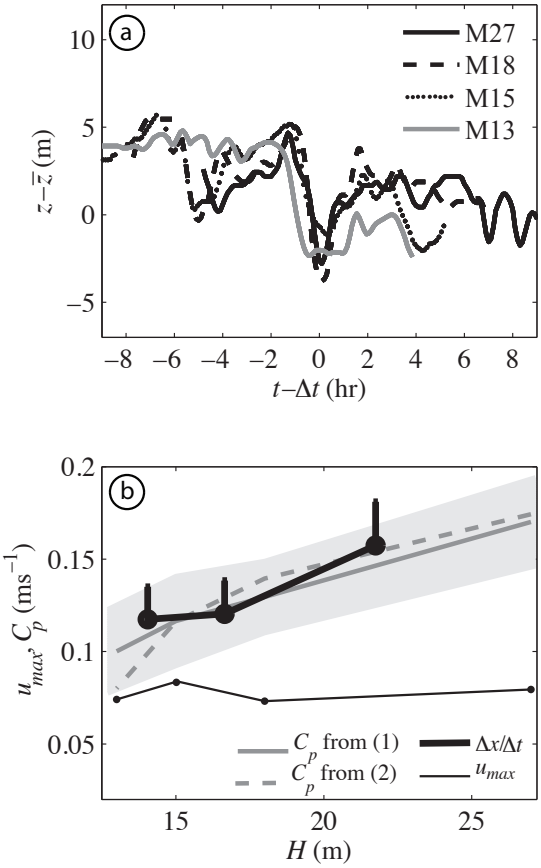

Figure 2.9: (a) Depth anomaly of mid water-column isotherms (bold contours in Fig. 8) vs. lagged time (T-Δt) at M27, M18, M15, and M13 (*see* legend), with Δt for each mooring chosen to orient the isotherm trough minimum at T = 0. (b) Observed (thick black line), theoretical phase velocity C_p (solid gray line (equation 1) and dashed gray (equation 2) and u_{max} (thin black line) above the wave trough vs. the water depth H. The observed C_p =Δx over Δt was estimated midway between neighboring moorings, with Δx the mooring separation. Error bars on observed C_p represent deviations associated with a $\pm$30 deg incident IW angle. The shaded region represents the potential C_p range from (1) based on the standard deviation of N.

IW [*Sverdrup and Johnson*, 1942]:

$$C_p = \sqrt{2g(\frac{\rho - \rho'}{\rho + \rho'})\frac{hh'}{h + h'}} \tag{2.2}$$

where ρ (ρ') and H (h$'$) are the upper (lower) layer density and thickness, respectively. The upper layer was defined as the time-averaged (over two hours preceding the passage of the IW) mean sIW isotherm depth (*see* bold isotherm contours in Fig. 2.8) and ρ (calculated from T) was vertically averaged across each layer.

The observed $C_p = \Delta x$ over Δt varied from ~ 0.12 $0.17\,\mathrm{m\,s^{-1}}$(black curves in Fig. 2.9b) and were similar to theoretical C_p (compare gray solid (1), dashed (2) curves in Fig. 2.9b) showing that the observed coherent propagation over 3 km between M27 and M13 is consistent with simple estimates for IWs. The observed C_p decrease with decreasing depth, has been observed previously for sIW on the Southern California shelf [*Winant*, 1974; *Winant and Olsen*, 1976; *Lerczak*, 2000; *Johnson and Pegau*, 2001].

2.5.2 Stage 2: Formation of the Intense Chl*a* Patch within an Internal Wave Trough

Motile dinoflagellates such as *Lingulodinium polyedrum* can maintain water column position despite negatively buoyant cell bodies [*Cox*, 1980]. The combination of swimming and convergent advection may lead to accumulation of phytoplankton at fronts [*Franks*, 1992] or above internal wave troughs [*Franks*, 1997; *Lennert-Cody and Franks*, 1999, 2002] hereafter LCF). In studies conducted $\sim$ 150 km south of Huntington Beach, CA, LCF showed that *L. polyedrum* advection by IWs in combination with depth-keeping swimming behavior locally enhanced Chl*a* above wave troughs. The LCF model suggests that the degree of Chl*a* enhancement is proportional to the separation between the isotherm and the surface Δz, for a given swimming proficiency. Similarly, systematically elevated Chl*a* within the sIW-associated isotherm trough was observed at M13, qualitatively consistent

with IW-induced convergence and phytoplankton depth-keeping swimming behavior.

As described in the previously, the sIW propagated coherently onshore, maintaining shape, with a phase speed consistent with linear theory (Fig. 2.9b). At M13 on 12 October, Chl a in the sIW trough (black star, Fig. 2.8d), was maximum (31 $\mu g L^{-1}$) and nearly triple the (vertical) mean concentration (11.5 $\mu g L^{-1}$) bordering the 17.0 °C isotherm between 06:00 and 17:00 h. During this time period, Chl a at M13 (vertically averaged between the 17.0 °C isotherm and the surface; solid black curve in Fig. 2.8d) and the isotherm depth Δz were significantly positively correlated (Fig. 2.10). The vertically averaged Chl a was maximum where the isotherms were the deepest. In contrast, T, vertically averaged between the 17.0 °C isotherm and the surface, was uncorrelated with Δz. The linear relationship between the vertically averaged Chl a and Δz, and the absence of a T-Δz relationship, do not depend on the choice of isotherm within the range 16.5 °C to 17.2 °C, associated with the sIW. This along-isotherm Chl a variation is not due to NPQ (*see* Web Appendix) as the maximum NPQ correction for Chl a on the 17.0 °C isotherm was 9%, far smaller than the observed variability. The time window of 06:00 to 17:00 h for the analysis was chosen such that the depth-averaged T was quasi-stationary (with a time-mean of 16.9 ± 0.3 °C) as required by LCF. A weaker Chl a patch (maximum = 22.3 $\mu g L^{-1}$) was also observed near 00:00 h centered over a 16 °C isotherm trough (Fig. 2.5c). Since this occurred at night, it could not have been caused by NPQ, supporting the hypothesis that the daytime patch was also largely formed by the LCF mechanism.

The significant correlation (r^2 =0.57, $p < 0.01$), observed between the vertically averaged Chl a and depth of the 17 °C isotherm Δz is consistent with the predictions and observations of LCF: Chl a (*L. polyedrum*-dominated for both LCF and at HB06) was enhanced in wave troughs where isotherms are strained away from the surface. However, the mean Chl a-Δz relationship is qualitative since the amount of Chl a enhancement depends on the phytoplankton swimming proficiency (unknown) and direction (assumed) relative to rate of the vertical movement of the isotherms.

The intensity of the patch formed through the LCF depth-keeping mechanism depends

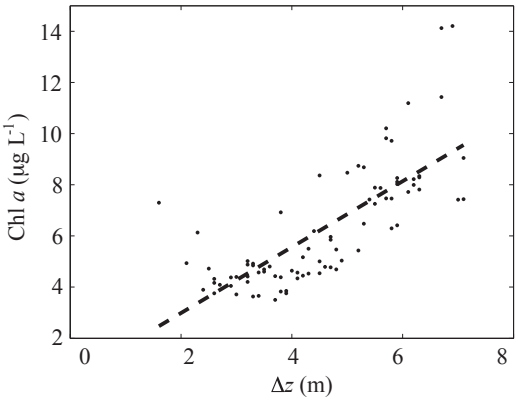

Figure 2.10: Vertically averaged Chl$a$ above the 17.0 °C isotherm vs. isotherm depth (Δz) at 4 min intervals between 06:00 and 17:00 h (number of data points, n = 165) on 12 October 2006). The linear fit (dashed line) has slope 1.29 ± 0.03 μg L^{-1}m-1, and r^2 = 0.57, p < 0.01.

on the swimming proficiency, the ratio of phytoplankton swimming speed to internal wave vertical currents. Laboratory instantaneous swimming speeds of *L. polyedrum* range between 100 and 400 μm s^{-1} [*Buskey*, 1997; *Lewis and Hallett*, 1997; *Mayali et al.*, 2008]. Vertical velocities (w) between 10:00 and 15:00 h estimated from vertical displacements of the 17.0 °C isotherm were about 300-1500 (*e.g.*, 2-9 cm min^{-1}, *see* bold isotherm displacements, Fig. 8d). The partial overlap between w and the range of *L. polyedrum* swimming speeds suggests that the dinoflagellates could have partially or completely countered the sIW-generated vertical velocities as required by LCF.

In addition to forming in the wave trough, it is possible that the Chl$a$ patch was advected from offshore ($H > 20$ m) to M13 within the sIW trough. Nonlinear internal waves of depression transport particles horizontally above the wave trough in the direction of propagation [*Lamb*, 1997a]. However, the sIW phase speed (0.12 to 0.17 m s^{-1}) was large compared to the mean Eulerian velocity above the wave trough at each mooring (0.07 to 0.05 m s^{-1} at M27 to M13, respectively), so particles may have been transported a short distance but would quickly be left behind the wave trough. Thus, though the Chl$a$ high

concentration region formed by the LCF mechanism may have moved onshore with the sIW trough, the organisms making up this patch were not advected across shore any appreciable distance [*see* also *Franks*, 1997]. These observations emphasize the potentially important role of swimming in generating Chl*a* patchiness, and show clearly that Chl*a* is not a passive tracer in this region of large amplitude, shoreward-propagating, internal waves.

2.5.3 Stage 3: Internal Wave Breaking

The sIW trough was evident at M13 (H = 13 m, black star, Fig. 2.8d), but not at M8 (H = 8 m, white star, Fig. 2.8e). To investigate the potential role of IW breaking leading to the disappearance of the sIW between M13 and M8, two theoretical criteria for IW breaking were considered. At M13, the sIW amplitude a_o was $\sim$ 5 m, based on the vertical displacement (crest to trough) of the 17 °C isotherm (thick black contour, Fig. 2.8d). Moving into shallow water, the group velocity of a shoreward-propagating internal wave decreases, and a_o increases to conserve wave energy flux, until the wave breaks [*Gill*, 1982]. For an idealized 2-layer system, breaking occurs when the undisturbed lower layer thickness h_{low} is less than h_{bp} [*Helfrich*, 1992] defined as

$$h_{bp} = \frac{a_o}{(1.6\frac{\gamma}{L} + 0.6)} \tag{2.3}$$

where Λ is the wavelength and L is the distance to the shelf break. L = 8000 m at Huntington Beach, where H = 60 m depth. For sIWs the ratio Λ:L is small, and h_{bp} depends only weakly on Λ. Using $\Lambda \sim$ 500 m (estimated from a wave period $\sim$ 2 h) an idealized sIW with a_o = 5 m would begin breaking when $h_{low} < h_{bp} \sim$ 7 m. Taking the lower layer thickness h_{low} as the mean elevation above the seafloor of the 17.0 °C isotherm where the sIW was most evident (*see* bold contour Fig. 2.8d) for 24 hours prior to the sIW passage, h_{low} was approximately 9 m at M13, and according to (3), the sIW was not breaking. At M8 (H = 8 m), h_{low} was always less than h_{bp} (Fig. 2.8d,e) supporting

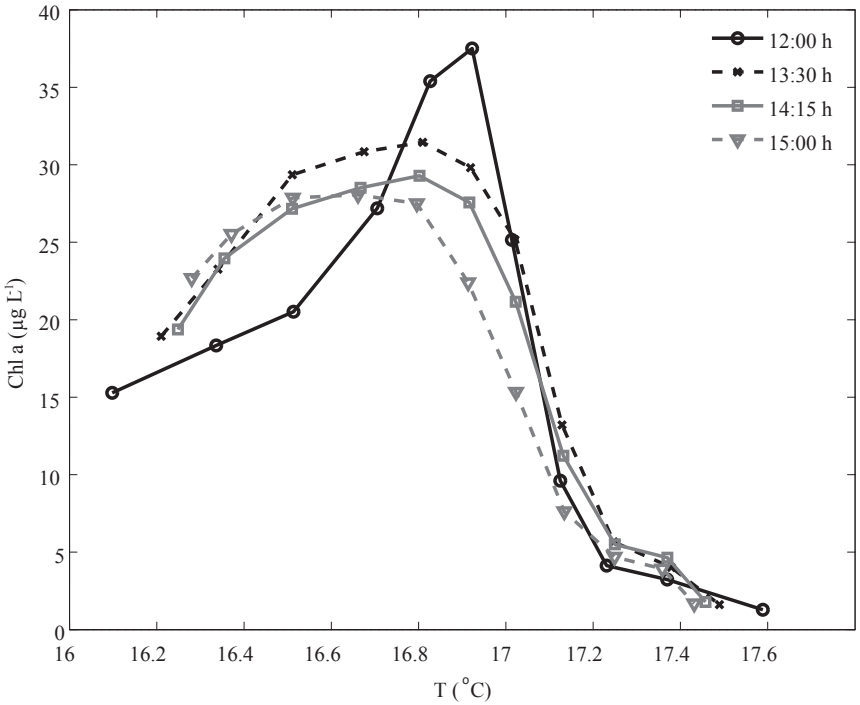

Figure 2.11: Chl*a* vs. *T* (at 12:00, 13:30, 14:15, and 15:00 h) based upon the CTD+Chl*a* surveys (between H = 5 to 13 m depth, *see* Fig. 7) horizontally averaged along 1 m isobars.

the hypothesis that wave breaking had occurred.

For shoaling solitary internal waves of depression, breaking occurs when the wave-induced near-surface horizontal currents above the wave trough (u_{max}) are equal to C_p [*Lamb*, 1997b]. At each mooring, u_{max} was estimated as the maximum cross-shore current (of the 15 minute averaged currents, *e.g.*, Fig. 2.5b) in the box defined by the top of the wave trough to 3 m below the surface, and over the timescale of the wave (roughly 1 to 2 h). The ratios u_{max}:C_p from (2) between M27 and M13 vary from 0.4 to 0.8 (compare the gray dashed line C_p and the thin black line u_{max} in Fig. 2.9b). Thus the *Lamb* [1997b] breaking criterion u_{max}:C_p = 1 suggests that the wave would not have broken by M13. This criterion was not investigated at M8 because the sIW was not evident and so an estimate

of u_{max} was not possible. The observations and theory thus support the hypothesis that the sIW broke between M13 and M8 as it propagated onshore.

2.5.4 Stage 4: Cross-Isotherm and Vertical Spreading of the Intense Subsurface Chl*a* Patch

The shoreward-propagating IW breaking (anticipated to reach $H < 13$ m at 12:30 h), may have mixed the water column vigorously enough for the subsurface Chl*a* patch to reach the surface, where it was visually apparent (Fig. 2.1) and appeared in the Jetski maps (Fig. 2.6c,e) as a 200 m-wide, surface patch onshore of M13. The surface Chl*a* band appeared around 1245 h on an isotherm warmer (T = 17.5 °C) than the isotherms associated with the subsurface patch (1617 °C, Fig. 2.5c) suggesting that cross-isotherm mixing had also occurred. Mixing induced by breaking sIW was illustrated by examining the cross-isotherm and vertical spreading of the subsurface patch. The temporal evolution of the T-z and Chl*a*-T relationships is quantified using objective maps of Chl*a* and T from 12:00 to 15:00 h, within the 750 m-wide region between H = 5 to 13 m. This region bounds the Chl*a* patch (Fig. 2.7), includes the estimated time and location of sIW breaking (white star in Fig. 2.5e), and excludes the warm shallow water region in the surfzone (emphx$<$ 200 m, h $<$ 5 m, Fig. 7). To minimize the effects of variability due to cross-shore advection on our analyses, CTD+Chl*a* cast-derived Chl*a* and T for each nearshore survey on 12 October were cross-shore-averaged (denoted $\langle \mathrm{Chl}a(\mathrm{z}) \rangle$ and $\langle \mathrm{T(z)} \rangle$), into 1 m-thick vertical bins.

The depth-average of $\langle \mathrm{Chl}a(\mathrm{z}) \rangle$ remained roughly constant (within 15%) between 12:00 and 15:00 h, consistent with small depth-integrated cross-shore Chl*a* fluxes, and small net phytoplankton growth and mortality over these 3 h. The depth-averaged $\langle \mathrm{T(z)} \rangle$ warmed slightly, from 16.9 °C to 17.1 °C. For each survey $\langle \mathrm{T(z)} \rangle$ were approximately linear with depth (not shown). The vertical temperature gradient $\mathrm{d}\langle \mathrm{T(z)} \rangle$ over dz decreased monotonically with time, and the corresponding buoyancy frequency (N) decreased from

0.018 s^{-1} at 12:00 h to 0.016 s^{-1} at 15:00 h, suggesting that vertical mixing dominated any stratifying effects of solar warming that would tend to increase N over the afternoon.

In addition to a reduction in N, cross-isotherm Chl$a$(z) mixing also was evident in the evolution of the cross-shore-averaged $\langle$Chl$a$(z)$\rangle$-$\langle$T(z)$\rangle$ relationship (Fig. 11). For all surveys, $\langle$Chl$a$(z)$\rangle$ was maximum near T = 16.9 °C. At 12:00 h, $\langle$Chl$a$(z)$\rangle$ was concentrated over a narrow range of $T(z)$, and throughout the afternoon, $\langle$Chl$a$(z)$\rangle$ spread over a larger range of $T(z)$ (e.g., compare the dashed gray with the solid black curve in Fig. 11). Although the CTD+Chl$a$ surveys exclude the top 1 m of the water column, the increased $\langle$Chl$a$(z)$\rangle$ at $\langle$T(z)$\rangle > 17.3$ °C after 12:00 h was in qualitative agreement with the surface appearance of the Chl$a$ patch associated with 17.5 °C water at the surface (e.g., Fig. 2.7e-j). To quantify the vertical spreading of the subsurface $\langle$Chl$a$(z)$\rangle$ layer, which includes cross-isotherm mixing, the $\langle$Chl$a$(z)$\rangle$ center of mass ($\langle z_{\mathrm{Chla}} \rangle$) was calculated [*Csanady*, 1973]:

$$\langle z_{\mathrm{Chla}} \rangle = \frac{\int_{-H}^{0} z \langle \mathrm{Chl}\, a(\mathrm{z}) \rangle \, dz}{\int_{-H}^{0} \langle \mathrm{Chl}\, a(\mathrm{z}) \rangle \, dz} \tag{2.4}$$

The center of mass deepened linearly from -7.1 m to -7.8 m (Fig. 2.12a) over 3 h at an average rate of 60 μm s^{-1}. The deepening of the layer peak is qualitatively evident in the CTD+Chl$a$ sections (Fig. 2.7a,c,e,g,i). The Chl$a$ layer squared half-width (σ^2_{Chla}) [*Csanady*, 1973],

$$\sigma^2{}_{\mathrm{Chla}} = \frac{\int_{-H}^{0} (z - \langle z_{\mathrm{Chla}} \rangle)^2 \langle \mathrm{Chl}\, a(\mathrm{z}) \rangle \, dz}{\int_{-H}^{0} \langle \mathrm{Chl}\, a(\mathrm{z}) \rangle \, dz} \tag{2.5}$$

increased roughly linearly with time until 14:15 h (solid line, Fig. 2.12b), as anticipated for breaking sIW turbulence. The layer width (2σ) grew from 4.2 m at 12:00 h to 4.7 m at 14:15 h, consistent with the qualitative Chl$a$ vertical spreading seen in the CTD+Chl$a$ sections (Fig. 2.7a,c,e,g,i). The slowing of the Chl$a$ vertical spreading by 15:00 h may be attributed to subsiding of the breaking sIW-generated mixing.

Although phytoplankton swimming is implicated in patch formation above the sIW trough at M13 (Fig. 2.10), swimming was unlikely to have accounted for the vertical spreading of the patch in H $<$ 13 m. Chl$a$ vertical spreading rate owing to random phytoplankton swimming (akin to a random walk) can be scaled by $\frac{1}{2}\tau\hat{u}_s^2$ where $\hat{u}_s$ is a typical swimming speed, and τ the decorrelation time of swimming direction. This is effectively a diffusivity, which can be compared to a vertical diffusivity κ_{zz} calculated from changes in the squared layer width σ^2 (Csanady 1973):

$$\kappa_{zz} = \frac{1}{2}\frac{\partial \sigma^2{}_{\mathrm{Chla}}}{\partial t} \tag{2.6}$$

The best-fit linear slope of $\sigma^2{}_{\mathrm{Chla}}$ between 12:00 and 14:15 h (dashed line, Fig. 2.12b) yields $\kappa_{zz} = 0.5 \times 10^{-4}$ m^2 s^{-1}. Assuming $\hat{u}_s \sim 200$ μm s^{-1}, τ = 40 min is required to reproduce the observed κ_{zz}. This τ is implausibly large, and would induce ballistic dispersion [*e.g.*, $\sigma^2{}_{\mathrm{Chla}} \sim t^2$ *Csanady*, 1973], instead of the observed linear (Brownian) relationship (Fig. 2.12b). The timing of the surface Chl$a$ band appearance is consistent with the expected arrival time of the sIW trough in shallow water ($\sim$12:30). The evidence supports our hypothesis that the breaking of the sIW in this region drove the vertical mixing that led to the vertical spreading of the intense Chl$a$ patch to the surface.

2.5.5 Stage 5: A Density Barrier to Chl$a$ Entry Into the Surfzone

During the jetski-CTD observation period, the high Chl$a$ surface band did not enter the surfzone region ($0 < x <$ 150 m) where the near-surface water was warmer than the near-surface offshore waters (*see* Fig. 2.7). Here, Chl$a$ and T observations from very shallow water ($H <$ 5 m) are presented, and a potential mechanism for the low surfzone Chl$a$ is discussed.

Between 10:00 and 12:00 h, near-surface T was uniform at roughly 17 °C from within the surfzone (M1.5) to M13 (Fig. 2.13a). Coincident with the M13 subsurface Chl$a$ peak (Fig. 2.4d), Chl$a$ at M4 (seaward of the surfzone) was also elevated (between 5-10 μg L^{-1}),

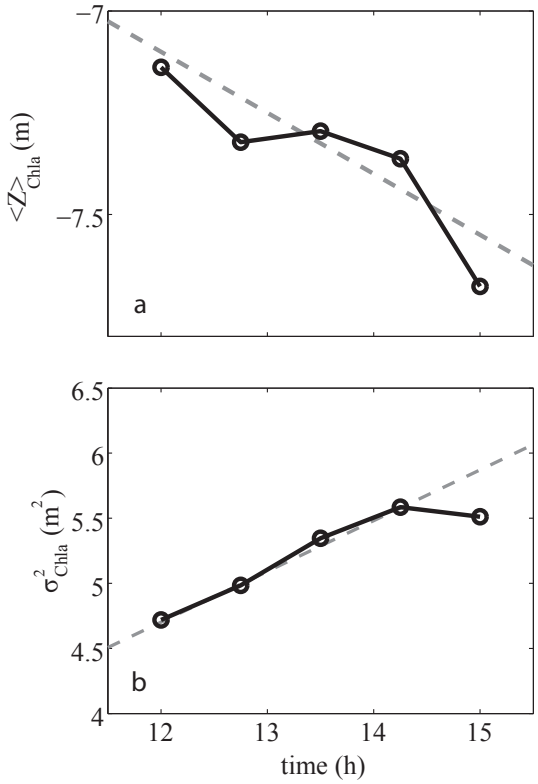

Figure 2.12: Timeseries of (a) depth $\langle z_{\mathrm{Chla}} \rangle$ of the center of mass of cross-shore averaged Chl$a(z,t)$ and (b) squared half-width $\sigma^2{}_{\mathrm{Chla}}$ (eq. 5) of the Chl$a(z,t)$ layer from 11:30 to 15:30 h on 12 October.

with the maximum Chl$a \sim 25\%$ of that at M13 (Fig. 2.6, solid black line, Fig. 2.12b). The M4 dinoflagellate (mainly *L. polyedrum*) cell concentrations also reached a maximum of 7.3×10^4 cells L^{-1} near 11:30 h (solid black line, Fig. 2.13c), while diatom abundance remained low (O(10^3) cells L^{-1}, dashed black line, Fig. 2.13c). The qualitative agreement between dinoflagellate cell concentration and Chl$a$ at M4 indicates that the Chl$a$ variation was due to variation in total dinoflagellates. Within the surfzone, Chl$a$ was lower at about 3-4 $\mu\mathrm{g}\,\mathrm{L}^{-1}$ (Fig. 2.13b), consistent with the jetski-observed Chl$a$ values in that region at 12:00 h (Fig. 7a). In the surfzone, dinoflagellate and diatom concentrations were low, usually $< 10^4$ cells L^{-1}, and relatively constant throughout the sample period (Fig. 2.13c).

At 11:30 h, the M4 Chl$a$ began dropping and by 12:30 h reached the level at M1.5 (3 $\mu\mathrm{g}\,\mathrm{L}^{-1}$). M1.5 and M4 Chl$a$ remained constant throughout the afternoon as T at both locations rose (Fig. 2.13). During mid-day, the near-surface T at M13 also increased slightly (thin curve in Fig. 2.13a). By 15:00 h, a cross-shore temperature gradient (with ΔT 1 °C) had developed between the warm surfzone water at M1.5 and the near-surface water M13, consistent with surface T maps (Fig. 7j). A strong afternoon T gradient was also maintained between M1.5 and M4 over only 80 m in the cross-shore.

The rapid and large T increase at M1.5 over 4 h cannot be explained by solar heating of the water column, and was much larger than the daily heating cycle normally observed near-surface at M13. The warm > 18 °C surfzone water present at M1.5 and M4 after 13:00 h likely originated from the Talbert Marsh, located 1 km South (+y) of the fixed instrument array (*see* Fig. 2.2). This water created a density barrier to Chl$a$ entry into the surfzone from offshore. Before 12:00 h, the flood tide (Fig. 5a) raised the marsh water level. Over the morning and early afternoon, the shallow marsh water ($H \sim 2$ m) was strongly solar heated relative to near-surface waters at M13. Based on the marsh area [10^5 m^3 *Grant et al.*, 2001], tidal prism [2.35×10^5 m^3 *Jeong et al.*, 42] and the solar insolation, the marsh water would have heated 0.8 °C. With the ebb tide at 12:00 h, the warmed marsh water began draining into the surfzone. The 0.15 $\mathrm{m}\,\mathrm{s}^{-1}$ northward surfzone alongshore current (*see* Fig. 2.7), driven by obliquely incident breaking surface gravity

waves [*Longuet-Higgins*, 1970], transported this water to the study region. The predicted increase of 0.8 °C is roughly consistent with the near-surface T gradient that developed between M1.5 and M13, and coincided with the reduction of Chl a at M4 (Fig. 2.13). If the warm water had not been present, the intense Chl a patch might have entered the surfzone.

2.5.6 Summary and Synthesis

The surface Chl a appeared on 12 October through local vertical mixing of a subsurface red tide layer (dominated by Lingulodinium polyedrum) that had developed in the study region over the 7 d prior (Fig. 2.14a). The kilometer-long shore-parallel surface Chl a band (maximum Chl a = 7 μg L^{-1}) persisted for approximately 3 h at depths H = 6-8 m with a cross-shore width of 200 m. At M13, an elevated Chl a patch was observed in the trough of a supertidal internal wave (sIW) that propagated coherently across the mooring array (Fig. 2.14b). The elevated Chl a in the sIW trough is consistent with formation by phytoplankton swimming interacting with a IW-induced convergent flow. Based on the estimated phase speed, the sIW arrived in shallow water ($<$ 13 m) around 12:30 h, where wave breaking occurred. Turbulence from the breaking sIW led to vertical mixing and the appearance of the subsurface Chl a patch at the surface. The wave arrival time (12:30 h), the approximate patch width (200 m), and depth of anticipated wave breaking (H $\sim$ 7 m) were all consistent with the appearance and dimensions of the surface Chl a band (Fig. 2.7). Finally, warm water exiting the Talbert marsh created a density gradient that inhibited the Chl a patch from entering the surfzone (Fig. 2.14c).

The high spatially- and temporally-resolved observations of a 2 km-wide subsurface red tide layer and the brief surface appearance of the red tide in a narrow (200 m), along-shore parallel band, highlight the challenges of red tide monitoring. The spatial and temporal scales of surface Chl a were roughly an order of magnitude smaller and shorter than those of the subsurface layer. However, a detailed analysis of the physical mechanisms underlying the surface band appearance provided a means of connecting it to the subsurface

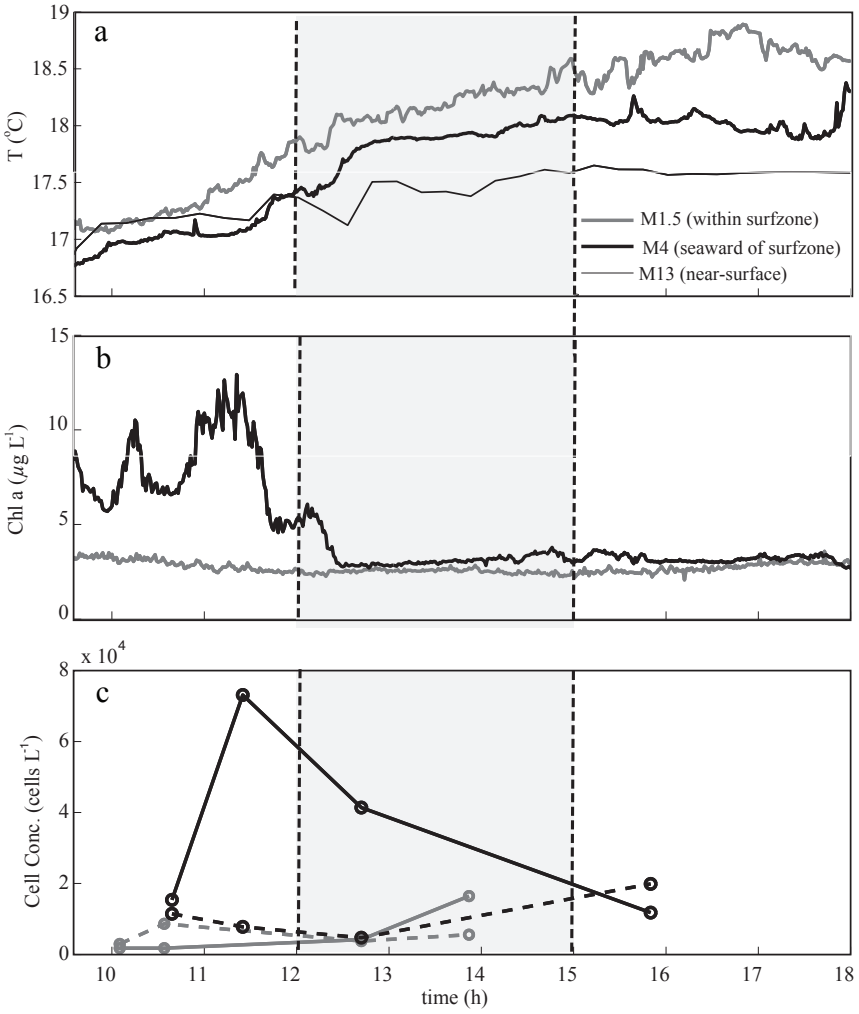

Figure 2.13: Time series from 09:30 to 18:00 h on 12 October of (a) T (1 min averages), (b) Chl$a$ (1 min averages), and (c) dinoflagellate (solid) and diatom (dashed) conc. from M4 (H = 4 m) and M1.5 (H = 2 m), and in (a) 20 min average T, 2 m below the mean sea surface at M13 (H = 13 m) (*see* legend). The CTD+jetski sampling period (12:00 to 15:00 h, Fig. 7) is indicated by the gray bar between vertical dashed lines.

Chl*a* field and offered insight into some drivers of short, small scale nearshore Chl*a* variability. The highly-resolved sampling across a number of different platforms - unique to this field study - was necessary to capture this broad range of nearshore Chl*a* patchiness.

The mechanisms underlying the surface band formation demonstrate that the drivers of Chl*a* distributions in the nearshore are complex. The interaction between motile phytoplankton and propagating internal waves, breaking internal waves, and surface wave-driven surfzone currents may create striking spatial and temporal changes in Chl*a* patchiness and community structure over O(100) meters and hourly timescales. Similar dynamics may be anticipated in a broad range of nearshore systems: where motile phytoplankton are present, where the stratification is sufficient to support internal waves, and where depth-limited internal wave breaking occurs. These mechanisms that rapidly concentrate, advect, and mix nearshore phytoplankton change the intensity and duration of shoreline exposure to red tide organisms, and may have large consequences for nearshore ecology.

2.6 Appendix: Corrections for Non-Photochemical Quenching (NPQ)

Chl*a* concentration is linearly related to Chl*a* fluorescence under most oceanic conditions (Lorenzen 1966). However, in situ Chl*a* fluorescence measurements can be biased low due to a phytoplanktonic physiological adaptation called nonphotochemical quenching [NPQ: *Keifer*, 1973; *Falkowski and Raven*, 1997; *Muller et al.*, 2001]. NPQ protects cells from high light conditions near the surface. To prevent cell damage from light absorption beyond the saturated capacity for photosynthesis, a fraction of the excess light energy is converted by the cell to heat, rather than fluorescence. The result is reduced fluorescence capacity per cell, leading to underestimation of fluorescence-derived near-surface daylight Chl*a* concentration.

Here, NPQ correction of fluorescence-derived Chl*a* was based upon the cells esti-

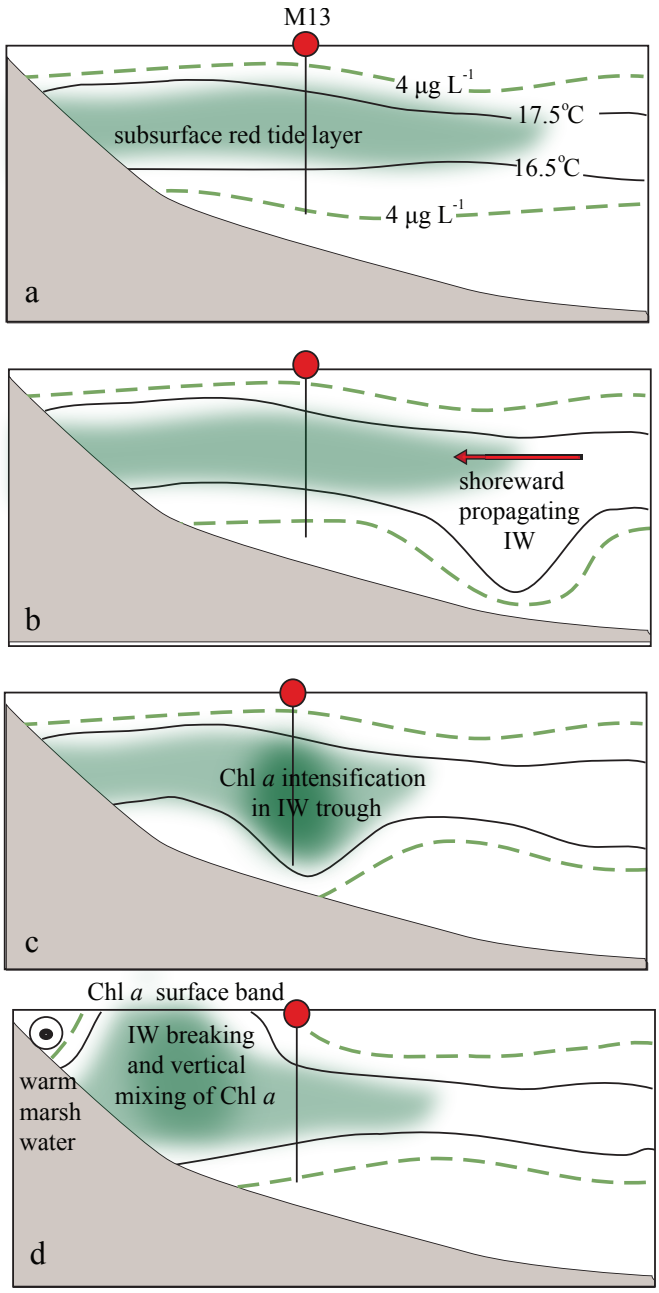

Figure 2.14: Schematic of nearshore ($H < 20$ m, *see* black box on Fig. 4d) summarizing the stages of the surface Chl*a* band formation. (a) An intense Chl*a* layer formed subsurface within 7 days preceding the surface appearance. (b) Chl*a* in an sIW trough was locally concentrated by swimming and sIW strain as the wave propagated onshore, (c) sIW breaking in shallow water caused vertical mixing and outcropping of the 17.5 °C isotherm and upper portion of the Chl*a* patch. On ebb tide, warm water carried by the surfzone alongshore current from the Talbert marsh, blocked Chl*a* entry into the surfzone.

mated local light environment (following Hodges 2006). A similar approach presented in *Todd et al.* [2009] with a correction based on local irradiance, produced a nearly identical result (maximum 6.9% difference) to the Chl a correction presented below. The 'corrected' Chl $a(z,t)$ (in the absence of NPQ) is a function of the fluorescence measured Chl a, Chl $a_m(z,t)$, and a quenching function $Q(z,t)$, i.e.,

$$\text{Chl}\, a_{\text{raw}}(\tau) = \text{Chl}\, a_{\text{true}} + \gamma\tau \tag{2.7}$$

where $Q(z,t)$ is a function of local irradiance $\phi(z,t)$. *Hodges* [2006] suggests a functional form for $Q(z,t)$,

$$\text{Chl}\, a_{\text{raw}}(\tau) = \text{Chl}\, a_{\text{true}} + \gamma\tau \tag{2.8}$$

where k is a constant, and $\phi\star(z,t)$ is the normalized local irradiance. The downward surface (z = 0) irradiance $\phi_o(t)$ was measured for 24 h near the field site on 16 October 2006, 4 days after the red tide observations (12 October). Both 12 October and 16 October were sunny, cloudless days, thus 16 October $\phi_o(t)$ was assumed representative of surface irradiance conditions during similar days at HB06. Surface irradiance was normalized by the maximum surface irradiance, i.e., $\phi_o\star(t) = \phi_o(t)$ over $\phi_{o,max}$. Irradiance was assumed to decrease exponentially with depth according to $\phi(\text{z},\text{t}) = \phi_{\text{o}}(\text{t})\text{e}^{\frac{\text{z}}{\gamma}}$ where γ is the unknown decay scale estimated from the vertical length scale of the covariation of Chl $a_m(z,t)$ with $\phi_o\star(t)$. The red tide time period (05 October through 16 October) was not used due to the intense subsurface Chl a layer with large vertical excursions over a 24 hr period (*see* Fig. 5c) that would complicate the estimation of γ. Instead, the time period from 20-25 September 2006, when M13 Chl $a_m(z,t)$ was low (1 - 4 $\mu\text{g}\,\text{L}^{-1}$) with no subsurface maxima, was used for the covariation analysis. Chl $a_m(z,t)$ covaried with $\phi_o\star(t)$ at the surface (r^2 = 0.50, $p < 0.01$). The correlation diminished with depth over an e-folding scale γ = 9.7 m. This γ is comparable to prior estimates ($\gamma \sim 5$ 11 m) from coastal waters in the Southern California Bight [*Holmes*, 1970; *Conversi and McGowan*, 39].

In (A2), the optimal k= 1.6 was chosen to minimize the correlation between Chl$a(z,t)$ and $Q(z,t)$, resulting in $Q(z,t)$ ranging between 0.615 and 1. Under maximum irradiance [i.e., $\phi\star(12:00\ h)=1$], near-surface Chl$a$ was enhanced by 56% relative to Chl$a$m, similar to *Hodges* [2006] finding that the maximum near-surface correction was roughly 100% Chla_m. The NPQ correction derived in (A1) and (A2) was applied to all in situ Chla_m measurements (CTD+Chl$a$, M13, M1.5, M4, *see* Fig. 2.1) presented here. Although the NPQ correction modified Chl$a$ concentrations as much as $2\times$ near the surface, the patterns described here were also present in uncorrected data. For example, along the 17°C isotherm the maximum NPQ correction imposed a 9% change from the raw measurement, insufficient to explain the $3\times$ Chl$a$ increase observed in the sIW trough.

2.7 Acknowledgements

B. Woodward, B. Boyd, K. Smith, D. Darnell, I. Nagy, D. Clark, M. Rippy, M. McKenna, and D. Michrowski assisted in collecting field observations. H. Mcclendon counted and identified the phytoplankton samples. The Golden West College Observatory collected surface irradiance data. These observations were obtained within the framework of the larger Southern California Coastal Ocean Observing System (SCCOOS) and United States Geological Survey (USGS) programs at Huntington Beach. George Robertson, Marlene Noble, Uwe Send, and Steve Weisberg are thanked for their cooperation and assistance. California Sea Grant, National Oceanic ad Atmospheric Administration, California Coastal Conservancy, National Science Foundation and the Office of Navel Research supported this research. Sea Grant support was through the California Sea Grant College Program Project R/CZ-196, through NOAA's National Sea Grant College Program, U.S. Dept. of Commerce. The statements, findings, conclusions and recommendations are those of the authors and do not necessarily reflect the views of California Sea Grant or the U.S. Dept. of Commerce.

Chapter 3

Episodic vertical nutrient fluxes and nearshore phytoplankton blooms in Southern California

3.1 Abstract

In Southern Californa, the nearshore ($<$ 20 m depth) is a unique environment for phytoplankton growth, and the underlying causes of intense nearshore blooms (particularly during summer and fall) are poorly understood. Phytoplankton growth is limited by nitrate (NO_3) flux into the euphotic zone. Due to the stable NO_3-temperature relationship below the nitracline, chlorophyll *a* Chl*a* is often correlated with temperature (T) during upwelling-driven NO_3 fluxes. However, nearshore Chl*a* is uncorrelated with sea surface temperature, wind or climate indices, indicating that non-upwelling processes may be be important controls on NO_3 flux. Here, we estimate both the advective and turbulent vertical NO_3 fluxes in 18 m depth at Huntington Beach CA, during summer and fall, 2006. We find that over the 4 month record, there are a series of three pulses of NO_3 flux lasting roughly 4 to 10 days each. The first NO_3 pulse in June, is mainly due to vertical advection

of NO_3, whereas the following two (in August and October) are both driven by a turbulent NO_3 flux generated during enhanced periods of water column shear. Each of the pulses in NO_3 flux was followed by a phytoplankton bloom (from near-bottom Chl$a$ in 15 m depth). The NO_3 and Chl$a$ were significantly correlated over a lag of 6 to 10 days, with a maximum $r^2 = 0.40$ at 8 days. Chl$a$ predicted from a very simple NP model driven only by the NO_3 fluxes captured the timing, width and approximate magnitude of each of the blooms ($r^2 = 0.49$), verifying that the vertical NO_3 flux was a primary control on the bloom events.

3.2 Introduction

In the Southern California Bight, the mean coastal (within 50 km of the shore) chlorophyll a (Chl$a$, a proxy for phytoplankton biomass) is roughly $10\times$ higher than offshore. This cross-shore gradient is consistent over decades both at the surface [*Eppley et al.*, 1979; *Haury and Shulenberger*, 1998; *Legaard and Thomas*, 2006] and subsurface [$\sim$ 100 m depth, *Kim et al.*, 2009]. In general, the enhanced Chl$a$ within the coastal zone is associated with higher phytoplankton productivity due to the upwelling of deep nutrient rich water. During springtime upwelling, there is a correlation observed between cooler surface temperature and elevated Chl$a$ [*Legaard and Thomas*, 2007; *Hayward and Venrick*, 1998], and an inverse relationship between vertically-integrated Chl$a$ and the thermocline depth [*Eppley et al.*, 1979].

The nearshore (depth $<$ 20 m) appears to be a unique environment for phytoplankton growth, particularly during the summer and fall [*Santoro et al.*, 2010], and the drivers of nearshore Chl$a$ means and variability are not yet well understood. For example, in a 20 yr record of Chla from the Scripps pier in La Jolla CA, there is no correlation observed between monthly averaged nearshore Chl$a$ and temperature, wind, or climate indices [*Kim et al.*, 2009].

The variability in Southern California monthly averaged [*Kim et al.*, 2009] and in-

traseasonal [*Legaard and Thomas*, 2007] nearshore Chl$a$ also appears to be up to 10$\times$ greater than offshore. This enhanced variability may in part be due to the occurrence of nearshore blooms or red tides. In general, there is a seasonal phytoplankton cycle, with a large spring bloom, followed by a series of shorter blooms, throughout the rest of the year [*Kim et al.*, 2009]. Dense bloom events (red tides) appear in the nearshore episodically, may appear and decline within days, and are challenging to monitor and predict [*Anderson*, 1997; *Horner et al.*, 1997]. Coastlines throughout North America are occasionally affected by harmful algal bloom species (HABs) that produce biotoxins, induce fish gill damage or anoxia [*Smayda*, 1997]. Harmful algal blooms that occur in the nearshore are particularly damaging due to the enhanced exposure to coastal and benthic habitats. An understanding of the drivers of these nearshore HABs and red tides is critical for improved management of aquaculture industries and other coastal resources [*Anderson*, 1997].

At depth, phytoplankton growth is limited by the light available for photosynthesis. Phytoplankton's ability to utilize light depends on the recent cell history and on evolutionary adaptations to light intensity and variability [*Dubinsky et al.*, 1984]. Most phytoplankton cannot grow below the euphotic depth (z_{eu}) where the light intensity is less than 1% of the incident irradiance. In the nearshore, z_{eu} is typically 15-20 m [*Holmes*, 1970].

In most areas of the Ocean, and the Southern California Bight in particular, seawater has nearly undetectable nitrate concentrations (NO_3) above z_{eu}. The local growth capacity of autotrophic phytoplankton (including red tide species and HABS) is limited by the available NO_3 relative to other macronutrients. The NO_3 concentration remains near zero with depth to an abrupt gradient (the nitracline). This sharp gradient is maintained by a balance of NO_3 uptake within the euphotic zone and vertical flux from below, and is stable with the density structure of the water column over time periods longer than phytoplankton uptake and growth timescales [*Cullen et al.*, 1983]. Vertical flux of deep nitrate into the euphotic zone is widely believed to be a critical control on phytoplankton growth [*Eppley et al.*, 1979].

Vertical NO_3 flux into the euphotic zone may be advective ($NO_3\mathrm{flux}_{\mathrm{adv}}$) or turbulent

($NO_3 flux_{mix}$). $NO_3 flux_{adv}$ occurs if the nitracline - following the isopycnals - is raised above z_{eu} by mechanisms such as upwelling [*Huyer*, 1983; *Denman and Powell*, 1984; *Traganza et al.*, 1987], or coastally trapped waves [*Chavez*, 1996]. $NO_3 flux_{adv}$ is the product of the local NO_3 concentration and the local vertical velocity, and because NO_3 is related to T, $NO_3 flux_{adv}$ is also expected to be proportional to T. This prediction is supported by the observed offshore correlation during spring upwelling between Chl$a$ and T [*Cullen et al.*, 1983].

$NO_3 flux_{mix}$ may be generated by IW breaking [*e.g.*, *Sharples et al.*, 2001], or friction in the surface and bottom boundary layers [*e.g.*, *Souza and Pineda*, 2001]. The current variability from these mechanisms is often too small for an ADCP to resolve, and so direct observations of turbulence requires microstructure measurements [*e.g., Dewey and Crawford*, 1987]. However, parameterizations from coarsely-spaced (meters to 10s of meters) bulk averages of currents, shear and stratification may provide useful estimates when microstructure measurements are unavailable [*Mackinnon and Gregg*, 2005]. In the nearshore, the euphotic zone intersects the bottom boundary layer and a region of depth-limited, or shear-induced, IW breaking. The importance of nearshore $NO_3 flux_{mix}$ may be enhanced relative to offshore. $NO_3 flux_{mix}$ is related to the local NO_3 gradient and the vertical eddy diffusivity at z_{eu}. The vertical NO_3 gradient is not linearly related to T, and so an explicit correlation between $NO_3 flux_{mix}$ and T is not anticipated.

In this paper, we focus upon the separate roles of vertical $NO_3 flux_{adv}$ and $NO_3 flux_{mix}$ in in delivering brief (> 2 week) pulses of NO_3 to the nearshore euphotic zone. The NO_3 fluxes are estimated in 18 m water depth, and compared with an adjacent Chl$a$ timeseries collected between mid-June and mid-October 2006, at Huntington Beach, CA (Fig. 3.1). This Chl$a$ record chronicles the rapid growth and demise of three distinct phytoplankton blooms, one of which was a red tide of the dinoflagellate *Lingulodinium polyedrum* (F. Stein). Over longer timescales, these short vertical nutrient pulses are likely superimposed upon other flux mechanisms that may operate over longer timescales, and determine seasonal Chl$a$ dynamics. For example, during summer and fall, although rainfall and riverine

outflow is small [*Reeves et al.*, 2004], nutrients stored in groundwater may lead to elevated nearshore Chl$a$ during summers that follow rainy winters [*Santoro et al.*, 2010]. In addition, nearshore Chl$a$ may be persistently enhanced by a thermocline tilt across the narrow continental shelf, and along-isotherm fluxes of NO_3 into the euphotic zone [*Lucas et al.*, 2011].

Despite these other mechanisms, brief, vertical NO_3 fluxes driven by advection and turbulent mixing appear to control the basic dynamics of episodic phytoplankton blooms. This hypothesis is tested through a lagged correlation analysis between Chl$a$ and the vertical flux, and also with a Nutrient-Phytoplankton (NP) model. Compartmental planktonic ecosystem models (ie. NP, NPZ, NPZD etc.) are commonly-used research tools that range in complexity [*Franks*, 2009]. Here, we choose an extremely simple formulation, and assuming a basic uptake function, drive the modeled phytoplankton (P) with the estimated NO_3 fluxes across z_{eu}. We will 1) present background physical observations of currents and temperature, 2) estimate the vertical NO_3 flux due to both advection and turbulence, and investigate the relative importance and temporal variability of vertical eddy diffusivity, vertical isotherm displacement rate, local nitrate and nitrate gradient, 3) explore the phytoplankton and nutrient composition during the third bloom in detail, both above and below z_{eu}, and 4) compare measurements of Chl$a$ to the NP model ouput which is driven by the NO_3 flux estimates. A range of growth and mortality parameters will be explored for the whole 4-month timeseries and for each of the blooms independently.

3.3 Methods

Nearshore observations were collected at Huntington Beach, California, USA, between 18 June and 25 October 2006, within the framework of the larger scale Southern California Coastal Ocean Observing System (SCCOOS) and United States Geological Survey (USGS) programs. Data are presented from a subset of moorings that span the 4 month record, and from a small boat-based sampling program between 27 September and 16 Oc-

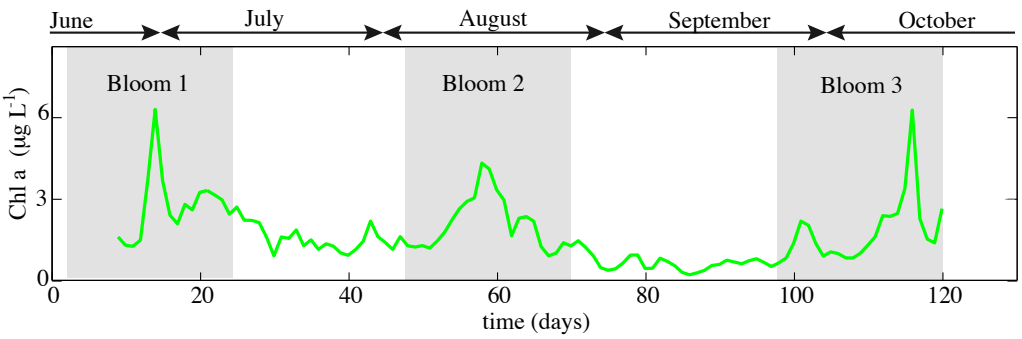

Figure 3.1: 24 h averaged timeseries of Chl a (μg L^{-1}) conducted during the summer and fall of 2006 at Huntington Beach California. Three bloom events are identified by gray bars. Intensive bloom sampling was conducted during Bloom 3 between 27 September (day 100) and 16 October (day 120).

tober. Observations spanned 0.5 km alongshore (y) and 4 km offshore (x) to 25 m depth (Fig. 3.2). The mean (tidally averaged) water depth is denoted as H, and the vertical coordinate z is positive upward, with $z = 0$ m at the tidally averaged surface.

3.3.1 Moored observations

A cross-shore transect of moorings, paired with bottom or surface-mounted current meters spanning $H = 8$ m to 59 m were deployed during HB06 [see *Omand et al.*, 2011]. Here, the focus is upon data from a subset of these instruments. Moorings in H = 8 and 18 m (M8 and M18 in Fig. 3.2) were instrumented with 4 (M8) and 5 (M18) Star- Oddi (T only) or Sea Bird MicroCAT (S and T) instruments sampling at 3 min intervals (blue circles, Fig. 3.2). Cross-shore (u) and alongshore (v) currents were measured with an RDI Acoustic Doppler Current Profiler (ADCP, 600 kHz) deployed at the base of M18 from June to October. This series was appended to the timeseries from an RDI ADCP (600 kHz) deployed at a similar location throughout October. The ADCP data was averaged to 6 min intervals with 1 m vertical bins. A bottom-mounted Nortek Aquadopp at M8 (2000 kHz) sampled every 2.5 min with 0.5 m vertical bins.

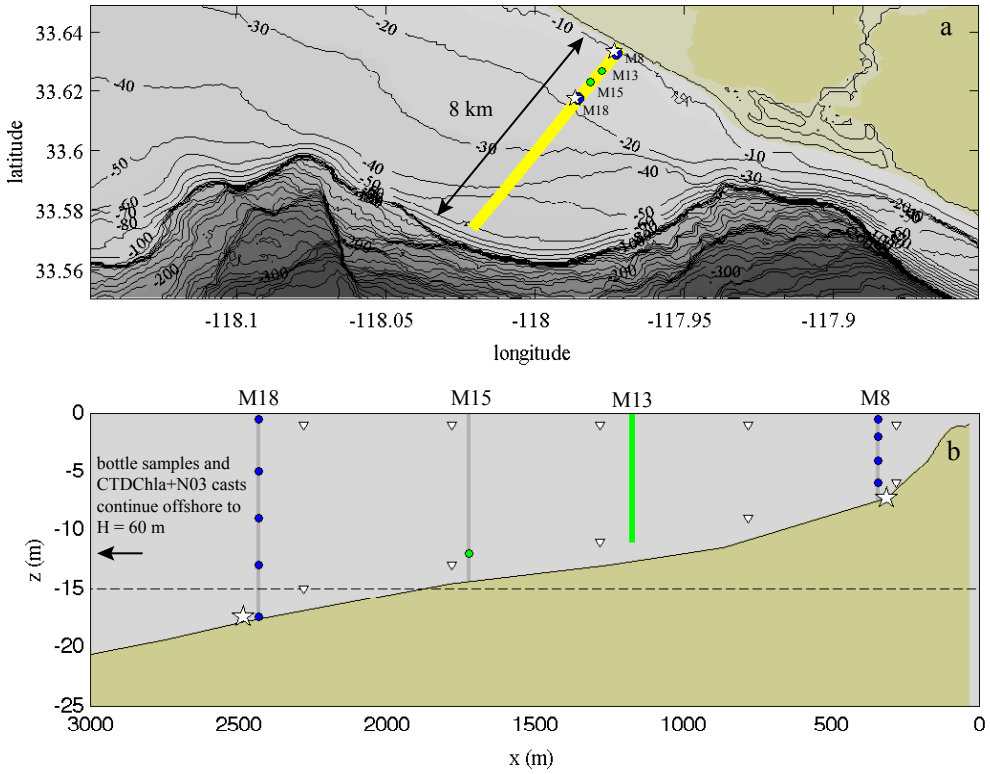

Figure 3.2: Schematic of the HB06 instrumentation: (a) plan view of bathymetry contours with the cross-shore (x) coordinate parallel to the instrument transect line and the along-shore (y) coordinate positive to the S-E, and (b) cross- shore transect of bathymetry. The vertical coordinate is z, with $z = 0$ m at the tidally averaged surface and positive upward. Moored thermistor strings (blue circles, M8 and M18) were located at tidally-averaged depths $H = 8$ and 18 m. Wind was measured slightly to the North of the main transect (black star). A vertically profiling CTD+Chl a wirewalker (M13) was located at $H = 13$ m. A Chl a fluorometer was also located near-bottom at $H = 15$ m. Bottom-mounted ADCPs (stars) were located near moorings M8 and M18. During an intensive bloom sampling period between 27 September and 16 October, CTD+Chl a transects were conducted in a 16 ft. whaler in $H = 5$ to 60 m (yellow bar, panel a) and water samples were collected near the surface and bottom at roughly 1 km spacing (triangles, panel b, to 8 km from shore). The instrumentation shown here represent the data that is presented within this paper, and is a subset of the total instrumentation at HB06.

At mooring M15, a Chl a fluorometer (WET Labs) was deployed at $z = -14$ m between 28 June and 17 September (green circle at M15, Fig. 3.2). The Chl a data was sampled at 0.25 Hz and averaged to 6 min intervals. A wirewalker, a wave-driven vertically profiling platform [*Rainville and Pinkel*, 2001], was deployed at H = 13 m (green line at M13 in Fig. 3.2b) between 17 September and 18 October. The wirewalker was instrumented with a CTD (Seabird 49, sample rate 16 Hz) and Chl a fluorometer (WET Labs ECO Triplet, sample rate 16 Hz). Vertical CTD+Chl a wirewalker profiles at M13 were completed approximately every 2 min; data were averaged into 0.1 m vertical bins and interpolated onto regular 4 min intervals. The M13 wirewalker was intermittently non-operational, with occasional data gaps up to 4 hrs. Nonphotochemical quenching corrections, derived from continuous profiles of Chl a at M13 and surface irradiance (measured with a Davis Vantage Pro Plus cosine pyranometer), were applied to all in situ Chl a measurements [see *Omand et al.*, 2011]. The maximum near-bottom Chl a correction at both M15 and M13 was less than 5% during peak daylight hours. The M15 Chl a timeseries from $z = -14$ m, and the lowest 2 m portion of the wirewalker Chl a timeseries were merged and averaged to 24 hour intervals resulting in a single 4-month long nearshore Chl a timeseries (Fig. 3.1).

3.3.2 Intensive small boat-based sampling

Densely-spaced vertical profiles and bottle samples were collected using a small boat on 8 days during the final month of the 4 month-long program. Cross-shore transects of CTD (Seabird 19), optical nitrate (Satlantic ISUS V3) and flow-through Chl a fluorometer (WET Labs WETStar) profiles spanning 6 km cross-shore (from H = 40 m to H = 5 m) were conducted between 9:00 and 11:30 h once per day on 27 September and 01, 04, 05, 07, 08, 12 and 16 October. CTD+Chl a+NO_3 data were post-processed with Seabird Electronics standard filters and averaged to 1 m depth bins. The top 5 m of optical nitrate data was excluded from the analysis due to increased data noise near-surface. A total of 131 total water samples were collected near the bottom with a messenger-tripped Niskin bottle

mounted 1 m above the CTD, and at the surface by hand during most CTD+Chl$a$+NO_3 casts (triangles, Fig. 3.2b). Water samples were kept dark on ice on the boat until returning to shore when triplicates water samples of 150 mL were filtered (Whatman GF/F) and analyzed for Chl$a$, and frozen for subsequent analysis of dissolved inorganic nitrate, phosphate, ammonium, and silicate concentrations using a QuikChem 8000 flow injection analyzer. The in situ sampling was used to verify or calibrate the Chl$a$ and NO_3 from the optical instruments. In addition, 82 of the water samples were preserved for phytoplankton taxonomic identification by transferring 100 mL of seawater to a glass Wheaton bottle and combining with 10 mL buffered 37% formaldehyde. The preserved samples were analyzed with the Utermöhl settling method (Utermöhl 1958) and inspected at 16$\times$ magnification using a light microscope. All visible cells (> 5 μm) were enumerated and identified to a genus or species level when possible.

3.4 Background Physical Observations

3.4.1 The NO_3-Temperature relationship

In order to understand the phytoplankton (and thus Chl$a$) dynamics over this 4 month period, estimates of the nitrate flux into the euphotic zone are required. Although nitrate was not measured continuously throughout the 4 month experiment, the stable NO_3-density relationship allows for estimation of NO_3 from density. The salinity effects on density were small at the Huntington Beach shelf, and the density (ρ) was strongly controlled by T. Therefore, the relationship between NO_3 and T is expected to be stable. Bottle and optical NO_3 decreases with T until 14.5 $^\circ$C where NO_3 approaches zero (Fig. 3.3). The HB06 NO_3-T relationship is independent of the day and cross-shore location, and is consistent with prior observations from coastal Southern California [*Dugdale et al.*, 1997; *Olivieri and Chavez*, 2000; *Lucas*, 2009]. Therefore, a temperature-derived nitrate proxy, defined as $NO_{3,T}$, is used over the entire 4 month record. Based upon linear best-fits be-

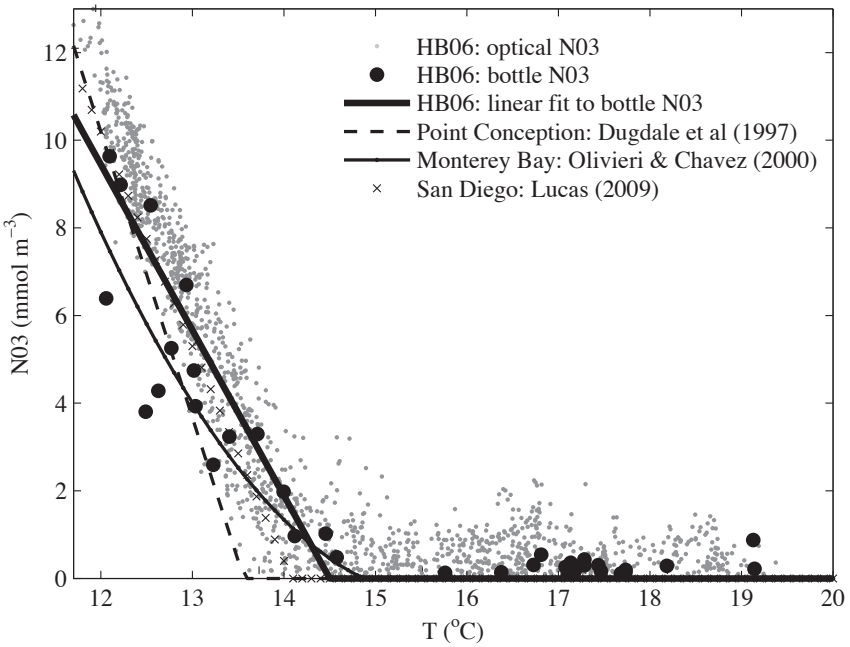

Figure 3.3: Optical (gray points) and bottle (black circles)NO_3 measurements versus temperature T, and the linear fit (thick black line) to the NO_3 bottle data versus temperature at HB06 throughout the intensive bloom sampling period. The HB06 measurements are consistent with previous fits to observations from throughout the Southern California Bight [*Dugdale et al.*, 1997; *Olivieri and Chavez*, 2000; *Lucas*, 2009].

tween bottle sampled NO_3 and T below $T = 14.5$ °C, the $NO_{3,T}$ (mmol m^{-3}) is modeled according to a linear relationship

$$NO_{3,T} = \begin{cases} -3.8T + 54.8, & \text{for } T \leq 14.5 \text{ °C} \\ 0, & \text{for } T > 14.5 \text{ °C} \end{cases}$$

3.4.2 Moored observations at M18

Over the four month long M18 record, temperature T generally ranged between 15 and 20 °C, with variability over subtidal and tidal scales (Fig. 3.4a). Cool water ($\leq$ 15 °C)

appeared periodically, remaining for intervals of 5 to 20 days. For example, a strong cooling event occurred between days 5 and 15, centered at day 10, where near-bottom T dropped below 10 °C. At M18, stratification (N^2) was calculated from the first difference of the low-pass filtered T (with a filter cut-off at ω = 0.3 cph) at each of the 5 thermistors spanning the water column. N^2 varied between 0 and 0.003 s^{-2} and was strongest during between days 1 to 70 (mid-June to September, Fig. 3.4b). The maximum stratification was typically mid-column, indicating that a sharp thermocline was present at M18 during most of the experiment. The temperature-inferred $\mathrm{NO}_{3,\mathrm{T}}$ was typically low (< 0.5 mmol m^{-3}, Fig. 3.4c), except during the strong cooling event centered at day 10, when $\mathrm{NO}_{3,\mathrm{T}}$ reached 13 mmol m^{-3}. The vertical nitrate gradient ($\partial \mathrm{NO}_{3,\mathrm{T}}/\partial z$) also tended to be low, (ranging between 0 and 0.5 mmol m^{-4}, Fig. 3.4d) with non-zero values concentrated near the seafloor, except for during the cooling event centered at day 10. During this period, $\partial \mathrm{NO}_{3,\mathrm{T}}/\partial z$ reached 2 mmol m^{-4} near the 14.5 °C isotherm in $z \geq -10$ m.

The vertical velocity $w = \mathrm{d}z_{\mathrm{iso}}/\mathrm{d}t$ was estimated from the vertical displacements (z_{iso}) of the isotherms at each depth and averaged over a 24 h, to exclude vertical advection too rapid for *in situ* phytoplankton growth or swimming responses. The estimated w reflect low-frequency vertical advection and varied between $\pm 5 \times 10^{-5}$ m s^{-1} (Fig. 3.4e). Upward advection (warm colors in Fig. 3.4e) preceded the cooling events and downward advection (cool colors in Fig. 3.4e) followed them.

The current variability was dominated by subtidal alongshelf currents that were strongest at the surface and decreased towards the seafloor. The remainder (15%) of the current variability was due to baroclinic mode 1 tidal variability. During some periods, the diurnal currents may have been enhanced by a resonance with the diurnal sea breeze [*Lerczak et al.*, 2001; *Nam and Send*, 2011]. The horizontal current speed $U = \sqrt{u^2 + v^2}$ varied between 0 and 0.6 m s^{-1} (Fig. 3.4f). The vertical shear of the cross- ($\partial u/\partial z$) and alongshore ($\partial v/\partial z$) velocity were estimated [following *Mackinnon and Gregg*, 2003] from the first 3 and 2 EOFs (corresponding to 90% and 99% of the variance) of the low-frequency (cut-off frequency 0.3 cph) u and v, respectively. The low-frequency EOF-estimated squared shear

($S^2 = (\partial u/\partial z)^2 + (\partial v/\partial z)^2$) varied between near 0 and 0.002 s^{-2} (Fig. 3.4f). The 5-15 day periods of enhanced shear centered at days 17, 60 and 110 corresponded with periods of enhanced near-surface current speed. The maximum shear however, occurred subsurface, either at mid-column (as would be anticipated for baroclinic modes, see days 53 to 68) or near the bottom (as would be anticipated for a logarithmic bottom boundary layer, see days 17, 29, 117). The fluctuation between mid-column and near-bottom shear indicates that neither low-mode baroclinic IW mixing nor bottom boundary layer mixing can be excluded from consideration in driving turbulent vertical nitrate flux.

3.5 Estimating the Vertical Nitrate Flux

3.5.1 Vertical NO_3 flux due to vertical advection

The vertical advective NO_3 flux into the euphotic zone is the product of the NO_3 concentration and the vertical velocity (w) at the euphotic depth z_{eu}, *i.e.,*

$$NO_3 \text{flux}_{adv} = w NO_3|_{z=z_{eu}}. \tag{3.1}$$

The precise z_{eu} location will vary with incident light intensity and water turbidity. Here, a fixed euphotic depth at $z_{eu} = -14$ m is used, which is chosen so that it is above the seafloor at M18 and below 10 m depth (the shallowest euphotic depth observed with a sechhi disk in $H \approx 20$ m at Imperial Beach, CA). The bottom boundary layer (BBL) thickness defined by the 0.2 kg m^{-3} density difference from the bottom (see black contour, Fig. 3.4) indicates that z_{eu} is periodically within the BBL. At z_{eu}, $NO_{3,T}$ and w vary most during the first 40 days of the observation period (Fig. 3.5a). In particular, $NO_{3,T}$ drops after day 40, and remains low (< 0.5 mmol m^{-3}) until briefly peaking above 2 mmol m^{-3} on day 80 and 109. The $NO_3 \text{flux}_{adv}$, estimated from (3.1), has a similar temporal structure; remaining near zero during most of the record with a large positive peak (upward NO_3 flux) centered at day 10, and smaller positive peaks at days 21 and 108. These positive peaks are followed

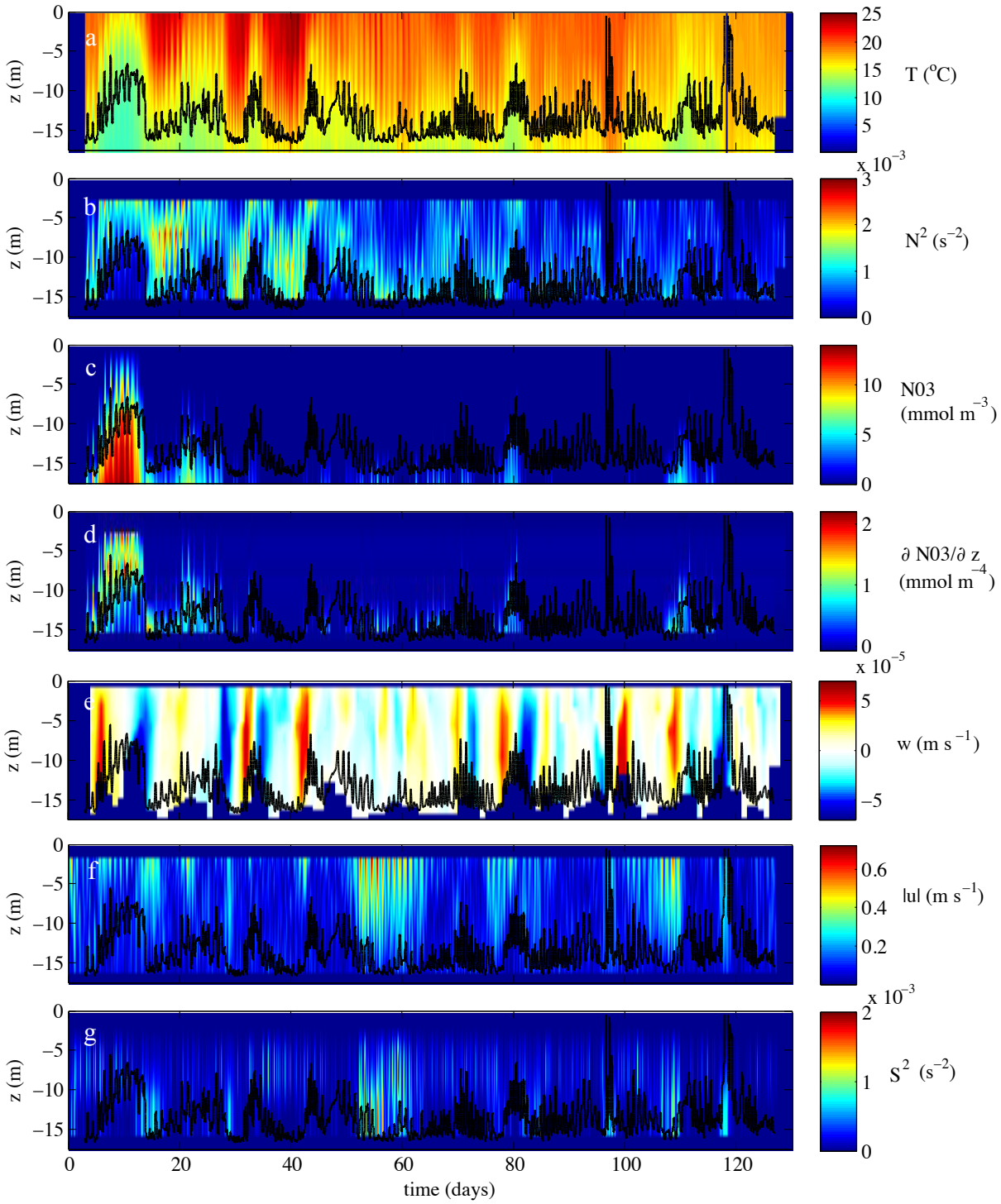

Figure 3.4: Timeseries at mooring M18 of (a) current speed ($\mathrm{m\,s^{-1}}$), squared shear S ($\mathrm{s^{-2}}$), (c) temperature T (°C), (d) buoyancy frequency squared N^2 ($\mathrm{s^{-2}}$), (e) nitrate gradient $\frac{\partial NO_{3,T}}{\partial z}$ ($\mathrm{mmol\,m^{-4}}$), (f) rate of isotherm displacement w ($\mathrm{m\,s^{-1}}$) at M18. Each series derived from T was vertically interpolated onto a 0.5 m grid. Contours indicate a boundary where the density difference ($\Delta\rho$) from the bottom was 0.2 $\mathrm{kg\,m^{-3}}$

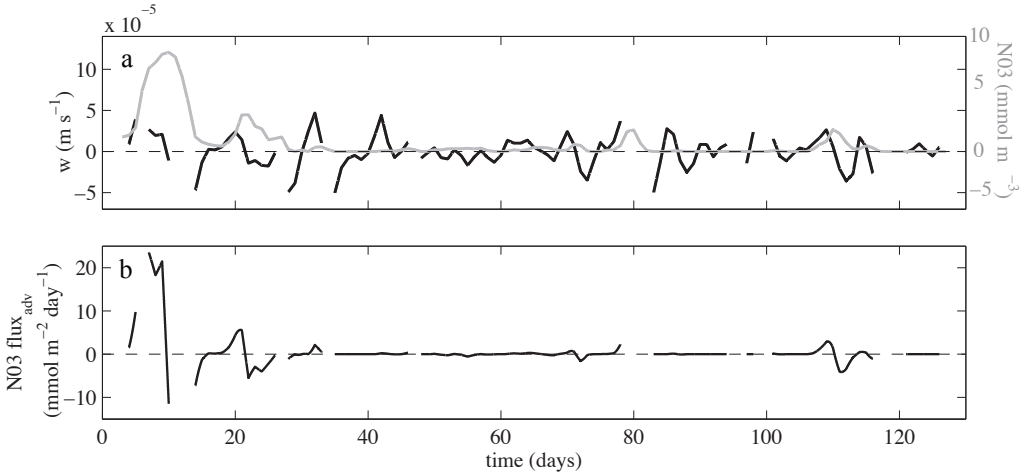

Figure 3.5: Timeseries at mooring M18 of (a) vertical isotherm displacement w ($\mathrm{m\,s^{-1}}$) and NO_3 at z_{eu}. (b) NO_3 flux driven by vertical advection of isotherms.

by a negative (downward) flux. The $NO_{3,T}$ advected upwards generally remained in the euphotic zone for > 1 day.

3.5.2 The Vertical Turbulent NO_3 Flux

The vertical turbulent nitrate flux is estimated from the product of the vertical eddy diffusivity (κ) and the vertical NO_3 gradient ($\partial NO_{3,T}/\partial z$) across the euphotic depth according to

$$NO_3 \mathrm{flux}_{\mathrm{mix}} = -\kappa \frac{\partial NO_{3,T}}{\partial z}\bigg|_{z=z_{eu}} \tag{3.2}$$

where $\partial NO_{3,T}/\partial z$ is estimated from the temperature-derived $NO_{3,T}$ (see Fig. 3.4d). The vertical eddy diffusivity κ has contributions from various turbulence sources, including shear-induced BBL mixing, and internal wave (IW) shear-induced mixing. Here the IW and BBL induced diffusivities are investigated separately to estimate the turbulent vertical nitrate flux (3.2). Surface generated mixing due to wind mixing [*e.g., Csanady*, 1984] or white-capping wave breaking [*e.g., Agrawal et al.*, 1992] is not considered because winds

were rather weak and the euphotic depth is much closer to the seabed than the sea-surface.

IW breaking-induced diffusivity

Most internal wave-based turbulence parameterizations are based upon the observed spectral properties of open ocean internal wave fields [*Henhey et al.*, 1986; *Gregg*, 1989], and may be inappropriate for the nearshore where the surface and bottom boundary layers can intersect and vertical wavenumbers are depth-limited. *Mackinnon and Gregg* [2005] developed a parameterization for the internal-wave shear driven turbulent dissipation rate ($\varepsilon_{\mathrm{IW}}$) in subcritical Richardson number ($\mathrm{Ri} = S^2/N^2$) flows on coastal shelves. The $\varepsilon_{\mathrm{IW}}$ is the product of the low-mode, low-frequency shear (S) and stratification (N), according to

$$\varepsilon_{\mathrm{IW}} = \varepsilon_o \frac{S}{S_o}\frac{N}{N_o}, \tag{3.3}$$

where ε_o, S_o and N_o are reference values, selected to best match the microstructure-derived ε [*Mackinnon and Gregg*, 2005]. Based upon empirical observations of the relationship between shear production and buoyancy flux in IW-induced turbulence, the vertical eddy diffusivity diffusivity (κ_{IW}) is given by the relation [*e.g., Osborn*, 1980]

$$\kappa_{\mathrm{IW}} = \Gamma \frac{\varepsilon_{\mathrm{IW}}}{N^2} \tag{3.4}$$

where Γ is a mixing efficiency (≈ 0.2). Note that this implies that $\kappa_{\mathrm{IW}} \propto S/N$ or $\propto \mathrm{Ri}^{-1/2}$

The low-pass (with cutoff at 0.3 cph) filtered shear (S, Fig. 3.4f) and buoyancy frequency (N, Fig. 3.4d) were vertically averaged between $z = -13$ m and -17.5 m (Fig. 3.6a). The buoyancy frequency N varied between 0.035 and 0.01 s^{-1} with the majority of the variability dominated by the trend towards lower N (reduced stratification) throughout the study period (black curve in Fig. 3.6a). The shear S generally varies between 0.05 to 0.02 s^{-1}, except for the 10 day time period centered around day 55 where S increased significantly, varying between 0.02-0.035 s^{-1} (gray curve in Fig. 3.6a). The $\varepsilon_{\mathrm{IW}}$ is calculated

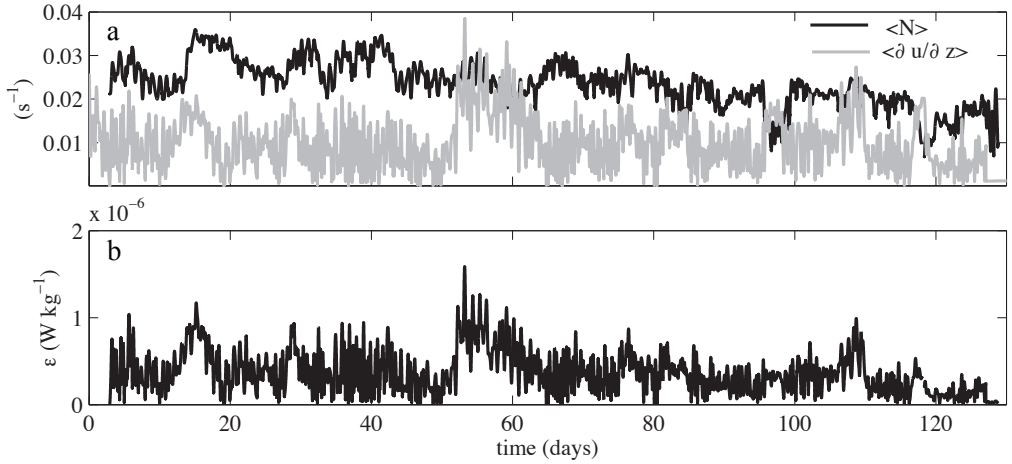

Figure 3.6: Timeseries at M18 of vertically averaged (a) S (s^{-1}, gray line) and N (s^{-1}, black line) across the bottom 5 m of the water column, and (b) estimated turbulent kinetic energy dissipation rate (ε_{IW}) from the *Mackinnon and Gregg* [2005] parameterization.

from (3.3) with $S_o = N_o = 3$ cph and $\varepsilon_o = 1.1 \times 10^{-9}$ W kg^{-1} (Fig. 3.6b). The r^2 between ε_{IW} and S is = 0.82 ($p < 0.001$), whereas r^2 between ε_{IW} and N is 0.17 ($p < 0.001$). Although use of the New England shelf parameters (ε_0, S_0, and N_0) may not be appropriate in the shallower waters here, the observed ε_{IW} range was roughly consistent with that observed in prior studies [*Lucas*, 2009] and is also consistent with the dissipation of IW-energy derived [following *Lerczak et al.*, 2001] from the gradient of IW energy flux between moorings M18 and M8, The κ_{IW} is calculated from (3.4) and is discussed below.

Bottom boundary layer friction-induced diffusivity

In the nearshore, where the water depth is close to the euphotic depth, the euphotic depth may be within the bottom boundary layer (BBL) and turbulent mixing within the BBL produced by frictional shear can drive a vertical nitrate flux. Within the BBL, where stratification is minimal, the turbulent shear stress (τ) is roughly constant, and may be written in terms of a characteristic velocity scale u_* (friction velocity) and fluid density (ρ) as $u_* = \sqrt{\tau/\rho}$. The vertical eddy diffusivity within the BBL (κ_{BBL}) depends upon the

scale of the eddies at each point in the flow, and may be estimated by the product of u_* and the height above the bed z according to

$$\kappa_{\mathrm{BBL}} = k u_* z_b, \tag{3.5}$$

where $k = 0.35$ is Von Karmans constant and z_b is the height above the seabed. Assuming that the turbulent shear stress is proportional to the vertical gradient in the mean currents $\mathrm{d}|u|/\mathrm{d}z$ (analogous to laminar flows), then ${u_*}^2 = \kappa_{\mathrm{BBL}} \mathrm{d}|u|/\mathrm{d}z$, and the velocity gradient can be written as

$$\frac{\mathrm{d}|\mathrm{u}|}{\mathrm{dz}} = \frac{u_*}{k z_b}. \tag{3.6}$$

Vertically-integrating (3.6), results in the classic [*e.g., Tennekes and Lumley*, 1972] BBL logarithmic velocity profile,

$$|u| = \frac{u_*}{k} \log\left(\frac{z_\mathrm{b}}{z_0}\right). \tag{3.7}$$

where z_0, the "apparent" bed roughness, is the height where $|u| = 0$, which in combined wave-current flows can be a function of the currents, waves, and bed-roughness [*Grant and Madsen*, 1979].

A u_* time-series is derived by fitting (*i.e.,* log-fits) the velocity in the lowest four ADCP bins (spanning z_b = 2 to 5 m, see Fig. 3.7) to $\log(z_\mathrm{b})$ at 2 hr time increment. The subtidally filtered (33-hr cutoff) currents were used in the logarithmic fits, as it is for these longer time-scales that the BBL has been adjusted. For the fits, z_0 was fixed at 1 cm, which is typical of muddy bottom coastal shelf flows [*Grant et al.*, 1984] similar to that observed at M18. The u_* obtained from this method ranged between 0.05 and 0.9 $\mathrm{cm\,s^{-1}}$ (black line, Fig. 3.8a) similar to the results of *Grant et al.* [1984], who found a u_* range of 0.5 to 1 $\mathrm{cm\,s^{-1}}$ on a muddy bottom over the same $|u|$ range. The velocity profiles were typically very consistent with a logarithmic profile with (least-squares) fit skill usually > 0.9 (Fig. 3.8b).

This method to estimate u_* requires that stratification is weak and does not suppress

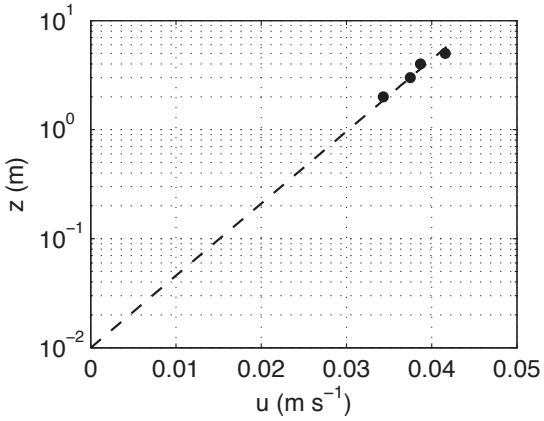

Figure 3.7: An example of a logrithmic fit to the data from the four near-bed current meter bins with z_0 fixed at 1 cm for one 2 hr averaged increment (day = 47.7) of the subtidally filtered currents at M18. Correlation r^2= 0.96 ($p < 0.01$) and skill is 0.99.

the vertical length-scale of the eddies. Thus during times of stronger stratification, u_* may be overestimated. Friction velocity u_* can also be derived from a quadratic drag law, *i.e.,*

$$u_*{}^2 = C_d|u|^2. \tag{3.8}$$

where C_d is a drag coefficient. On the New England shelf in 70 m water depth, direct stress observations observations indicated that at a height 1.1 m above the bed $C_d = 1.5 \times 10^{-3}$ [*Shaw*, 1999]. The u_* estimated with (3.8) using $C_d = 1.5 \times 10^{-3}$ were consistent with the log-fit u_* (compare gray and black curves in Fig. 3.8a). The agreement between the two u_* indicates that the stress estimate is reasonable. The κ_{BBL} is then estimated from (3.5) using the log-fit u_* and $z_b = H + z_{\mathrm{eu}} = 4$ m.

Comparison of the IW-induced and BBL-induced κ parameterizations

In the nearshore at the euphotic depth, the turbulent vertical NO_3 flux is governed by both IW and BBL processes. These components cannot be neatly separated, particularly

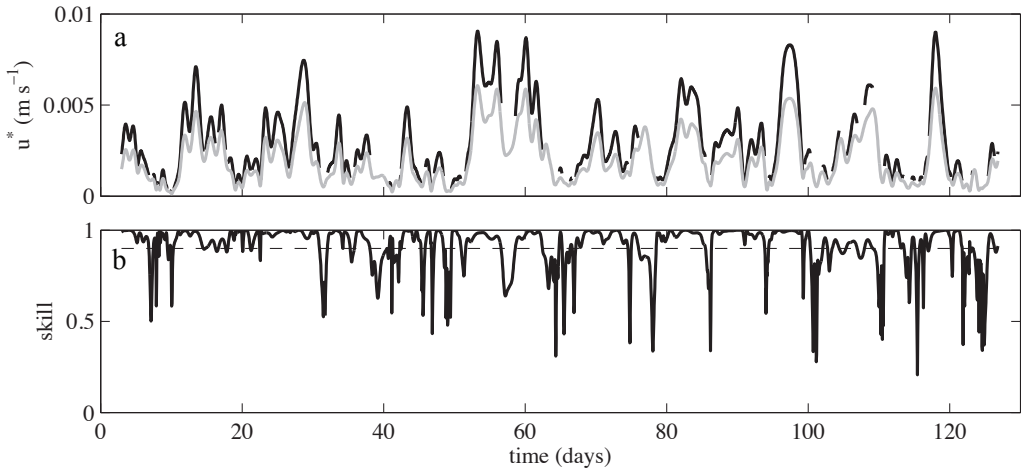

Figure 3.8: Timeseries at mooring M18 of (a) u_* ($\mathrm{m\,s^{-1}}$) from logrithmic fits (black curve) and derived from a quadratic drag law (Eq. 3.8, gray curve) with $C_d = 1.5 \times 10^{-3}$ [*Shaw*, 1999] and (b) skill of the logarithmic fit (*e.g.,* Fig. 3.7). In (a), the two estimates of u_* are highly correlated ($r^2 = 0.99$, $p < 0.001$). In (b), 28% of the log-fit skill fell below the 0.9 cutoff limit (gray dashed line) and were removed from the analysis.

with the limited observations available. In addition, the analysis here may only be appropriate under very specific conditions. BBL theory applies within the constant stress layer where stratification is weak. The BBL width is often < 2 m (black curve in Fig. 3.4), and below the euphotic depth. Similarly, below the The *Mackinnon and Gregg* [2005] $\varepsilon_{\mathrm{IW}}$ scaling requires depths that are much larger than one vertical wavelength of the high-frequency test waves. However, both of the κ parameterizations are similar in that they are proportional to the water column shear S. Note that $\kappa_{\mathrm{IW}} \propto S/N$ and is correlated with S ($r^2 = 0.72,\ p < 0.001$) and not with N ($r^2 = 0.12$), and (with some re-arrangement) $\kappa_{\mathrm{BBL}} = k^2 z_b^2 S$.

The κ_{IW} and κ_{BBL} estimates are correlated ($r^2 = 0.65$ ($p < 0.001$). However the κ_{BBL} estimates are generally $3\times$ larger than the κ_{IW} estimates (Fig. 3.9a). The κ_{IW} vary between $0.05 - 0.4 (\times 10^{-3})$ $\mathrm{m^2\,s^{-1}}$, and is roughly consistent with a Chl$\,a$ vertical spreading-derived $\kappa = 0.5 \times 10^{-4}$ $\mathrm{m^2\,s^{-1}}$ from a study of IW breaking and vertical mixing that occurred on day 116 (12 October, 2006) at HB06 [*Omand et al.*, 2011]. It is also consistent with the range of diffusivities $0.05 - 0.5$ ($\times 10^{-3}$ *msqs*) found by *Eppley et al.* [1979] in nearshore Southern California. As the BBL log-fit method may overestimate κ_{BBL} due to neglect of stratification, the more conservative IW-based κ_{IW} is used for the subsequent estimate of the turbulent vertical NO_3 flux.

The (T-derived) subtidally averaged (33 hr cutoff) vertical nitrate gradient $\partial \mathrm{NO_{3,T}}/\partial z$ at z_{eu} varied between 0 and 1.2 $\mathrm{mmol\,m^{-4}}$ (red curve in Fig. 3.9a) and was strongest during days 0–30, during the period of the first Chl$\,a$ bloom. The $\partial \mathrm{NO_{3,T}}/\partial z$ was also elevated to 1 $\mathrm{mmol\,m^{-4}}$ around day 100, preceding the 3rd bloom. During the time period of the second bloom (days 50–70), $\partial \mathrm{NO_{3,T}}/\partial z$ was only moderately elevated. The estimates of $\mathrm{NO_3 flux_{mix}}$ ($= \kappa_{\mathrm{IW}} \partial \mathrm{NO_{3,T}}/\partial z$) varied between 0 and 25 $\mathrm{mmol\,m^{-2}\,d^{-1}}$ (Fig. 3.9b) and generally was elevated at three distinct time periods: days 0–30, days 50–80, and days 105–115. Note that the $\mathrm{NO_{3,T}}$ flux near day 50 was driven more by increased turbulence (κ_{IW}) than by vertical $\mathrm{NO_{3,T}}$ gradient.

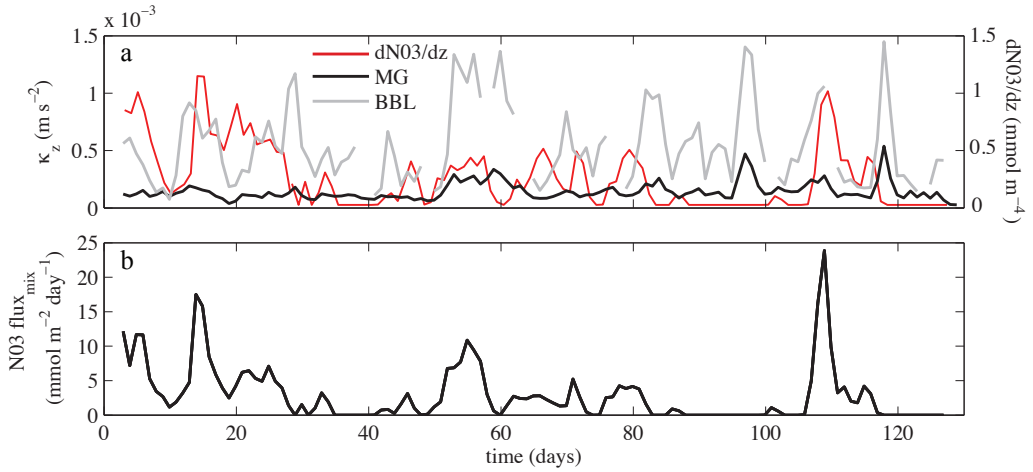

Figure 3.9: 24 h averaged timeseries of (a) vertical eddy diffusivity κ ($m^2\,s^{-1}$) estimated from the *Mackinnon and Gregg* [2005] parameterization (black line) and the bottom boundary layer method (gray line) near z_{eu} = 14 m at M18. The two parameterizations are significantly linearly correlated, with $r^2 = 0.65$ and $p < 0.001$. (b) vertical NO_3 gradient $\partial NO_{3,T}/\partial z$ (mmol m^{-4}) at $z_{eu} = -14$ m at M18.

3.5.3 Vertical advective and turbulent NO_3 flux and relationship to Chl*a*

The 24 hr averaged vertical $NO_3 flux_{adv}$ (gray line, Fig. 3.10) and $NO_3 flux_{mix}$ (red line, Fig. 3.10) at $z_{eu} = -14$ m were obtained from Eq. 3.1 and Eq. 3.2 respectively. The total vertical nitrate flux (black line, Fig. 3.10),

$$NO_3 flux_{tot} = NO_3 flux_{adv} + NO_3 flux_{mix} \tag{3.9}$$

varied between zero and 27 mmol m^{-2} d^{-1} and had three distinct NO_3 flux events (Fig. 3.10). The estimated NO_3 flux range was similar to observations of internal tide-driven turbulent vertical fluxes of NO_3 on the New Zealand shelf [12 mmol m^{-2} d^{-1} *Sharples et al.*, 2001]. The first NO_3 flux event occurred from days 0–30 (gray shaded region in Fig. 3.10). The total flux $NO_3 flux_{tot}$ has a significant contribution from both the advective and turbulent flux components (compare red and gray curves in the gray shaded region in Fig. 3.10). The second (day 50–80) and third (days 105–115) NO_3 flux event were dominated by $NO_3 flux_{mix}$ (red curve matches black curve in the pink shaded region of Fig. 3.10). The reduced importance of $NO_3 flux_{adv}$ during this later period is consistent with the trend towards reduced stratification throughout the record (*e.g.,* Fig. 3.6a).

Each $NO_3 flux_{tot}$ events preceded an elevated Chl*a* event or bloom. Bloom 1 was centered on day 14, bloom 2 on day 58 and bloom 3 on day 116 (green curve in Fig. 3.10). A lagged correlation analysis indicates that Chl*a* is significantly correlated ($p < 0.001$) with $NO_3 flux_{tot}$ at Chl*a* lags of 6 to 10 days after the $NO_3 flux_{tot}$ events, with a maximum correlation $r^2 = 0.40$ at an 8 day lag. The time-lagged correlation between the three Chl*a* blooms and the three NO_3 flux events supports the hypothesis that the vertical $NO_3 flux_{tot}$ was an important factor in the appearance of each of the blooms (see Fig. 3.1).

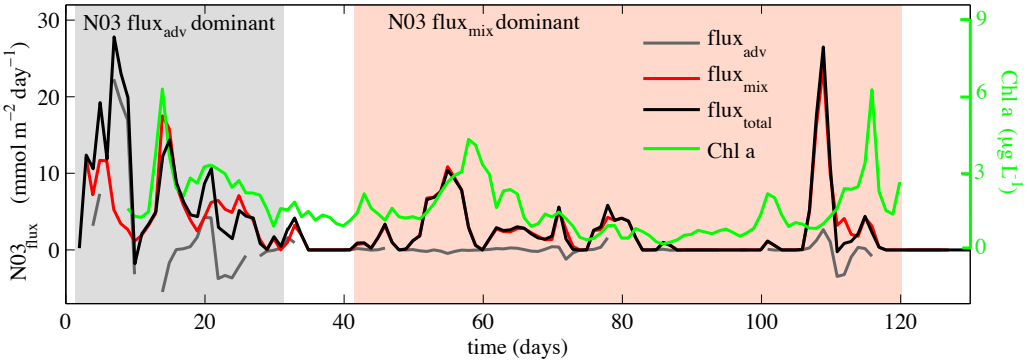

Figure 3.10: 24 h averaged timeseries of vertically mixed (red line), vertically advected (gray line), and total (black line) vertical nutrient flux (mmol m^{-2} d^{-1}) across z_{eu} at M18 and Chl a (green line) measured between z = 12 to 14 m at M15 and M13. The gray shaded region indicates where $NO_3 flux_{adv}$ dominated the total flux, and the red shaded region indicates where $NO_3 flux_{mix}$ dominated the total flux. The observed Chl a and $NO_3 flux_{tot}$ have maximum lagged-correlation ($r^2 = 0.40$) at 8 days.

3.6 A focused investigation of Bloom 3

Bloom 3 occurred during an intensive boat-based sampling program, providing an opportunity to investigate the phytoplankton species and nutrient dynamics in detail. Between 27 September (day 100) and 16 October (day 120), the time period prior to and spanning bloom 3, 131 bottle samples were collected and analyzed for Chl a, NO_3, dissolved silicate (DSi), NH_4 and PO_4. Of the 131 bottle samples, 82 bottle samples were analyzed for phytoplankton cell counts and species composition. In addition, cross-shore CTD transects provided vertical measurements of optical NO_3 (independent of $NO_{3,T}$), T and fluorometer-derived Chl a measurements.

3.6.1 Phytoplankton community and bloom composition

Diatom and dinoflagellate cells dominated the phytoplankton cell composition, representing 89% of the cells visible under light microscopy. Among the diatoms and di-

noflagellates, there were roughly equal cell numbers between each group, *Lingulodinium polyedrum* appears to control the Chl$a$ (Table 3.1). Dinoflagellates were predominantly composed of this single species, *Lingulodinium polyedrum* (*L. polyedrum*), whereas the diatoms were more diverse, and dominated by a range of *Chaetoceros*, *Asterionella* and *Psuedonitzschia* species. Normalizing for the unequal number of bottle samples collected in each region, the samples above the euphotic depth ($z > z_{\mathrm{eu}}$) contained 5.9$\times$ higher cell concentrations than those below the euphotic depth ($z < z_{\mathrm{eu}}$). Below the euphotic depth, although cell counts were much reduced, *L. polyedrum* was 6$\times$ more abundant than diatoms (Table 3.1). The low concentrations of non-swimming diatoms in the deeper samples supports the assumption that $z_{\mathrm{eu}} \sim$14 m.

On 12 October (day 116), the 24 hr averaged Chl$a$ at M13 peaked at $\approx 7\ \mu\mathrm{g\,L^{-1}}$ (Fig. 3.1). However, instantaneous measurements of Chl$a$ from the CTD+Chl$a$+NO_3 casts indicate that Chl$a$ reached 39 $\mu\mathrm{g\,L^{-1}}$ in $H \sim$10 m. Water samples coinciding with this high Chl$a$ were composed of a near mono-culture of *L. polyedrum*, and were found only within 3 km from the shoreline [for further details, see *Omand et al.*, 2011]. The nearshore bottle-sampled Chl$a$ was highly correlated with the *L. polyedrum* cells counts ($r^2 = 0.94$, $p < 0.001$) and also correlated with *Prorocentrum micans* ($r^2 = 0.62$, $p < 0.001$). However, because significantly more *L. polyedrum* were observed than *P. micans*, we conclude that the observed Chl$a$ variation during bloom 3 (Fig. 3.1) was driven by variation (due to growth, mortality, advection, and behavior) of *L. polyedrum*.

3.6.2 The NO_3-Chl$a$ Relationship

Nearshore observations ($500 < x < 3000$ m, where *L. polyedrum* was predominant) were separated into those collected above ($z > z_{\mathrm{eu}}$) and below ($z < z_{\mathrm{eu}}$) the euphotic depth. Within the nearshore euphotic zone, a phase diagram of optical NO_3 versus Chl$a$ supports the hypothesis that the elevated Chl$a$ at day 116 was driven by NO_3 flux into the euphotic zone (Fig. 3.11). Prior to the Chl$a$ bloom and NO_3 flux events (on day 100), the

Table 3.1: Percentage of cells among total counts, and r^2 with bottle measurements of Chl$a$, for dinoflagellates and diatoms, and the 4 most abundant phytoplanktonic genera (and species when possible) within each group. Percentages are given from above (n = 7.5×10^4) and below ($n = 0.9 \times 10^4$) $z_{eu} = 14$ m. 82 bottle samples were collected between 27 September (day 100) and 16 October (day 120), with 47 bottle samples from above z_{eu} and 35 samples from below z_{eu}. Significant (p< 0.001) r^2 correlations are identified in bold font.

Genus	$z > z_{eu}$	$z < z_{eu}$	r^2 with Chl$a$
Total Dinoflagellates	40.1	4.3	**0.10**
Lingulodinium polyedrum	30.0	3.5	**0.94**
Alexandrium sp.	4.30	0.1	0.02
Prorocentrum micans	3.6	0.3	**0.62**
Scrippsiella sp.	0.71	0.1	0.04
Total Diatoms	43.9	0.7	0.002
Chaetoceros sp.	15.7	1.6	0.001
Asterionella sp.	12.7	2.3	0.0001
Psuedonitzschia sp.	5.3	0.6	0.18
Skeletonema costatum sp.	2.1	0.03	0.001

average NO_3 and Chl$a$ were low, with $NO_3 < 0.1$ mmol m^{-3} and Chl$a \approx 3 \mu$g L^{-1} (red dots and circle marked 100, Fig. 3.11). On day 109, NO_3 was elevated with a mean of 0.32 mmol m^{-3} and a maximum near 0.65 mmol m^{-3}, as Chl$a$ remained low (green dots and circle in Fig. 3.11). This transition and maximum observed NO_3 coincided with the timing of the estimated $NO_3 flux_{tot}$ event (Fig. 3.10). Over the following week (through days 112 and 113, dark and light blue in Fig. 3.11), euphotic NO_3 decreased and Chl$a$ increased, consistent with NO_3 uptake and phytoplankton growth. By day 116, NO_3 was near zero and Chl$a$ had reached a maximum of ≈ 9 μg L^{-1} (magenta dots and circle in Fig. 3.11). Finally, on day 120, NO_3 remained low (< 0.1mmol m^{-3}), and Chl$a$ had declined to ≈ 6.5 μg L^{-1} as the bloom dissipated (gray dots and circle in Fig. 3.11).

If the change in NO_3 concentration due to the vertical NO_3 flux was well captured by the optical NO_3 measurements, and 100% of the NO_3 was converted to phytoplankton biomass, then the slope of NO_3 vs. Chl$a$ would reflect the cellular Nitrate:Chl$a$ ratio of the

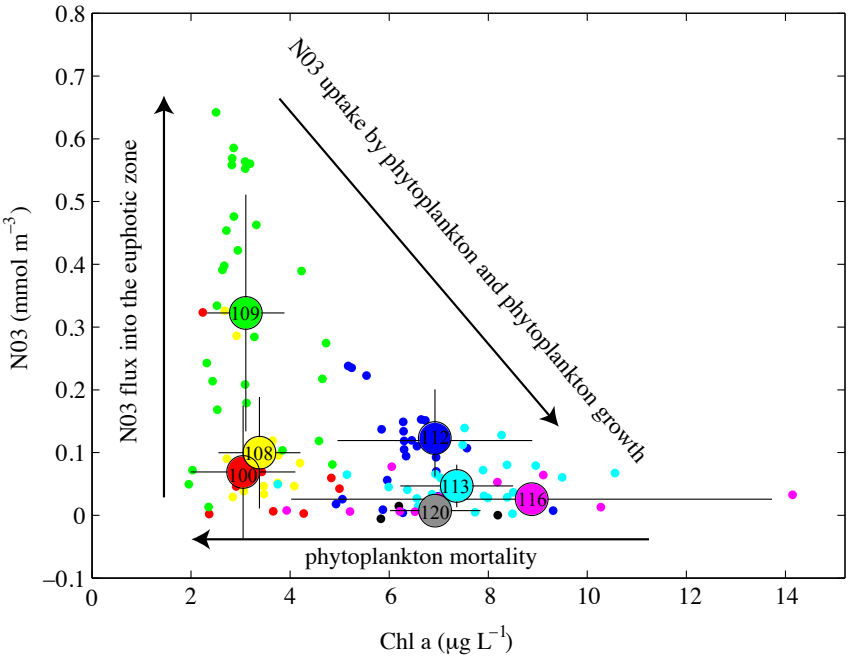

Figure 3.11: Averages (solid circles) and individual 1 m binned measurements (small dots) of optically measured NO_3 versus Chl$a$ within the nearshore ($500 < x < 3000$ m) euphotic zone ($z < 14$ m) on each of the days during Bloom 3 when CTD+Chl$a$+NO_3 transects were conducted. The arrows illustrate the anticipated temporal progression during each bloom stage, beginning with the pre-bloom, pre-flux conditions, the NO_3 flux, NO_3 uptake and phytoplankton growth, and loss (mortality/sinking) from the euphotic zone.

community. This ratio for *Lingulodinium polyedrum* may be estimated from Redfield ratio of Nitrogen:Carbon, the atomic weight of carbon and the Carbon:Chl$a$ ratio (θ) according to

$$\text{Nitrate} : \text{Chl}a \left[\frac{\text{mmol N}}{\text{mg Chl}a}\right] = \frac{16}{106}\left[\frac{\text{mmol N}}{\text{mmol C}}\right] \times \frac{1}{12}\left[\frac{\text{mmol C}}{\text{mg C}}\right] \times \theta\left[\frac{\text{mg C}}{\text{mg Chl}a}\right]. \quad (3.10)$$

The Carbon:Chl$a$ ratio (θ) varies depending on cell size, species, ambient light and nutrients, and here an intermediate $\theta = 30\ \frac{\text{mg C}}{\text{mg Chla}}$ [*Cloern et al.*, 1995] is used. Eq. 3.10 therefore suggests that a typical Nitrate:Chl$a$ relationship is 0.378 $\frac{\text{mmol NO}_3}{\text{mg Chla}}$. The slope of NO_3 vs. Chl$a$ between day 109 and day 116 is estimated to be 0.06 $\frac{\text{mmol NO}_3}{\text{mg Chla}}$, far less than that predicted by Eq. 3.10, indicating that more Chl$a$ was observed than would be predicted by uptake of the observed mean NO_3 on day 109. Some potential issues to explian this discrepancy are: The observations are spatially and temporally aliased, the NO_3 is likely under-detected due to rapid uptake, and horizontal advection and other nitrogen sources may affect the relationship. However, despite these potential error sources, the temporal evolution of the *directly observed* NO_3-Chl$a$ relationship reflect the transitions anticipated during each bloom stage and highlight the role of NO_3 in controlling the Chl$a$ response.

3.6.3 The relationship between NO_3, Silicate, and Phosphate in the Euphotic Zone

Below the nitracline, NO_3, dissolved silicate (DSi) and phosphate (PO_4) are often linearly correlated according to the ubiquitous stoichiometric N:Si:P ratio of 16:16:1 [*Redfield*, 1958]. The nitracline boundary is defined here as the depth where $NO_3 = 2.5\ \text{mmol m}^{-3}$ and ranged between between ≈ -12 m and -25 m). The NO_3-DSi are highly correlated ($r^2 = 0.96$, $n = 23$, $p < 0.001$) with a best-fit slope (1.09) consistent with Redfield and an intercept of 0.78 mmol m^{-3} DSi at NO_3=0. The NO_3-PO_4 also are highly correlated ($r^2 = 0.94$, $n = 23$, $p < 0.001$) with a best-fit slope of 16.0, consistent with Redfield and an

intercept of 0.19 mmol m^{-3} PO_4 at NO_3=0. The non-zero DSi and PO_4 intercepts indicate that above the nitracline, NO_3 is the limiting nutrient. The monotonic relationships with NO_3 indicate that the mechanisms resulting in the (advective and turbulent) vertical NO_3 flux will also result in vertical fluxes of DSi and PO_4.

Due to the large scatter in the bottle-sample nutrients (collected at slightly different times and locations), the nearshore samples ($500 < x < 3000$ m) were averaged over the euphotic zone and into three distinct time periods corresponding to three stages of the Chl *a* bloom, defined as 'before flux' (BF) stage, the 'NO_3 flux' (NF) stage, and the 'phytoplankton bloom' (PB) stage. The BF NO_3, DSi and Chl *a* were initially low, with NO_3 near 0.2 mmol m^{-3} and DSi near 1.7 mmol m^{-3} (PO_4 is not shown). During NF, both NO_3 and DSi increased, and both declined during PB (red and blue points, Fig. 3.12) when Chl *a* was at a maximum (green points, Fig. 3.12). The mean NO_3 and DSi during each bloom stage were visibly different. NH_4 on the other hand, stayed relatively constant through each bloom stage (yellow points, Fig. 3.12). Insight into the bloom 3 dynamics can be gained through exploration of the nutrient ratios within the euphotic zone, and through comparison with Chl *a* and the sub-nitracline ratios.

As discussed, below the nitracline the ratios PO_4:NO_3 and DSi:NO_3 are stable and constant, consistent with *Redfield* [1958]. Within the euphotic zone, these relationships are more dynamic and depend upon the nutritional requirements and preferences of their consumers. The ratio DSi:NO_3 during each of the three bloom stages (see Fig. 3.12) were much higher (means between 5–8) than below the nitracline and the Redfield ratio of 1 [*Redfield*, 1958], indicating strong NO_3 limitation (compare large white circles with hollow circles, Fig. 3.13a). The DSi:NO_3 increased with increasing Chl *a* between BF and PB, consistent with the nutrient requirements of *L. polyedrum* and other dinoflagellates. Marine diatoms require DSi to form an external frustule, and their growth may be occasionally DSi-limited [*Turner et al.*, 1998]. However, dinoflagellates do not build silicate-based shells and thus do not deplete DSi. Elevated surface silicate is observed during dinoflagellate red tides, and may be a better indicator of previous deep-water nutrient

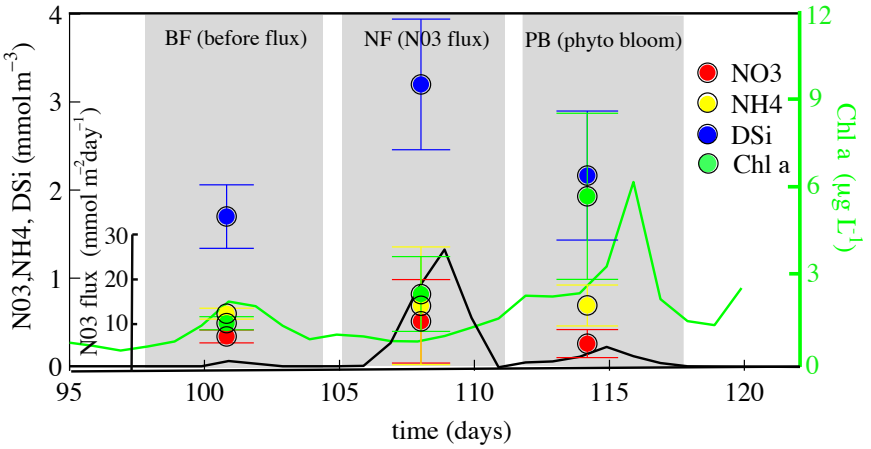

Figure 3.12: Means (circles) and standard deviations (vertical bars) of dissolved inorganic NO_3 (mmol m^{-3}, red), NH4 (mmol m^{-3}, yellow), silicate (DSi, mmol m^{-3}, blue), and Chl *a* (μg L^{-1}, green) versus time from nearshore ($500 < x < 3000$ m) and euphotic zone ($z > z_{eu}$) bottle samples for each bloom stage (before the NO_3 flux (BF), during the NO_3 flux (NF),and during the dinoflagellate bloom (PB)). The estimated total vertical NO_3 flux (black line) and measured Chl a (green line) from Fig. 3.10 are shown for reference.

enrichment than rapidly consumed NO_3 [*Armstrong and Strickland*, 1965].

Variations in the NH_4:NO_3 ratio in the euphotic zone may provide insight into the bloom dynamics. New production is phytoplankton growth that is supported by "new" nutrients, usually in an oxidized form such as NO_3, delivered into the euphotic zone [*Eppley and Petersen*, 1979]. Recycled nutrients such as ammonia (NH_4) are produced through cell lysis or zooplankton excretion are in a reduced form. Either NH_4 or NO_3 can fulfill a cell's nitrogen requirements, and euphotic zone phytoplankton growth is partly supported by recycled nutrients (*e.g.,* NH_4). NH_4 provides an energetic advantage for phytoplankton and is preferred over NO_3 [*Eppley et al.*, 1969a]. In addition, NH_4 may inhibit NO_3 uptake at NH_4 concentrations > 1 mmol m^{-3} [*Dortch*, 1990]. Throughout bloom 3, NH_4 concentrations were < 1 mmol m^{-3} (yellow points, Fig. 3.12), thus NO_3 uptake was unlikely to be inhibited.

Unlike DSi and PO_4, sub-nitracline NH_4 was uncorrelated with sub-nitracline NO_3.

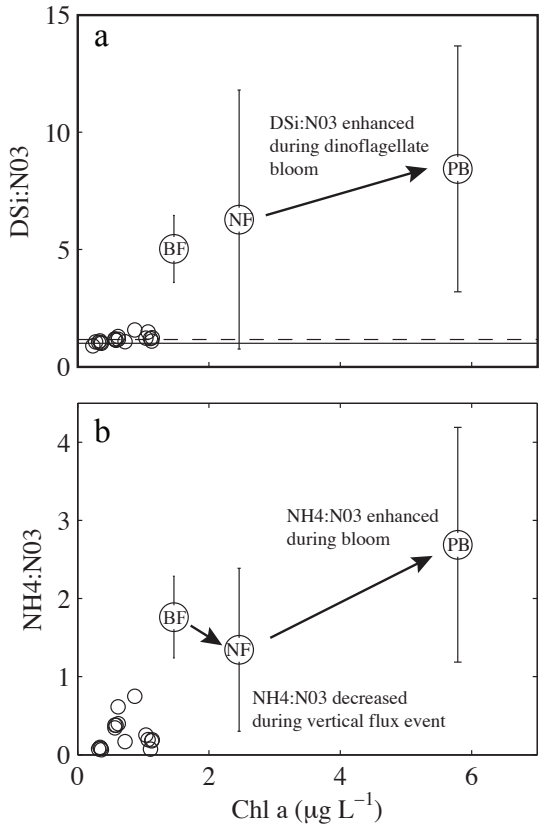

Figure 3.13: (a) Dissolved silicate (DSi) to NO_3 ratio versus Chl$a$ (μg L^{-1}) from nearshore ($500 < x < 3000$ m) bottle samples averaged within the euphotic zone ($z > z_{eu}$, large white circles) for each bloom stage. DSi:NO_3 ratio versus Chl$a$ (μg L^{-1}) below the nitracline ($NO_3 > 2.5$ μ, M, hollow dots) are clustered near 1 (solid line): the ratio predicted by [*Redfield*, 1958]. The mean silicate to NO_3 ratio below the euphotic zone (dashed line) is slightly higher than 1, indicating slight NO_3 limitation relative to DSi. (b) Ammonium (NH_4) to NO_3 ratio versus Chl$a$ (μg L^{-1}) from nearshore ($500 < x < 3000$ m) bottle samples averaged within the euphotic zone ($z > z_{eu}$, large white circles) for each bloom stage.

However, the sub-nitracline ratio $NH_4 : NO_3 < 1$ and was markedly lower than the euphotic-zone ratio that varied between 1.3–2.8 (compare large white circles with hollow circles, Fig. 3.13b). During BF, The NH_4:NO_3 ratio was near 2 during BF, was reduced during NF as NO_3 was supplied from below. During PB, NH_4:NO_3 increased to near 3, potentially due to NH_4 biological enhancement during the bloom, depletion of NO_3, or a combination of both.

Each of the nutrient observations provides evidence that the dinoflagellate-dominated bloom 3 was fueled by delivery of new nutrients (specifically NO_3). The correspondence of DSi and PO_4 with NO_3 implies that the nutrient source was below the nitracline where they are linearly related. That NH_4 did not change significantly preceding bloom 3, suggests that the nitrogen was not from an NH_4-enhanced terrestrial or sewage-related source. Finally, DSi is not depleted as intensely as NO_3 during PB, consistent with the *Armstrong and Strickland* [1965] prediction that for dinoflagellate blooms, DSi may be an indicator of a past sub-euphotic, nutrient enrichment.

3.7 Vertical $NO_3 flux_{tot}$ Nitrate-Phytoplankton Modeling

3.7.1 Model defintion and model parameters: growth and mortality rates

The estimated $NO_3 flux_{tot}$ and observed Chl$a$ were linearly correlated ($r^2 = 0.40$) with a time lag of 8 days (Fig. 3.10). Investigation of a simple nitrate-phytoplankton (NP) model allows the connection between $NO_3 flux_{tot}$ and the Chl$a$ to be explored in greater detail. In NP models, the phytoplankton variable (P) is the Chl$a$ concentration scaled by the N : Chl$a$ ratio $\alpha = 0.378$ mmol/mg (see Eq. 3.10), *i.e.,*

$$P = \alpha \text{Chl}a \tag{3.11}$$

so that NO_3 and P have the same units ($\mathrm{mmol\,m^{-3}}$) The basic model formulation for the euphotic-zone averaged nitrate and phytoplankton evolution is

$$\frac{dP}{dt} = (\mu - m)P \tag{3.12}$$

$$\frac{dNO_3}{dt} = -\mu P + \frac{NO_3 flux_{tot}}{z_{eu}} \tag{3.13}$$

where m ($\mathrm{d^{-1}}$) is the phytoplankton mortality rate, and the growth rate μ ($\mathrm{d^{-1}}$) is a function of the NO_3 concentration. The model NO_3 is forced by the observed vertical nitrate flux $NO_3 flux_{tot}$, which is assumed to deliver nutrients over the entire euphotic depth z_{eu}. The model neglects advection and has no depth-dependence.

A Michaelis-Menten equation [*Michaelis and Menten*, 1913] for the growth rate μ_{MM} is used in most NP models, where μ_{MM} is defined by two variables: a half-saturation constant K_s ($\mathrm{mmol\,m^{-3}}$) and a maximum NO_3 uptake rate μ_{max} ($\mathrm{d^{-1}}$) such that

$$\mu_{MM} = \frac{\mu_{max} NO_3}{K_s + NO_3}. \tag{3.14}$$

The μ_{max} and K_s have been estimated for a variety of phytoplankton [*e.g., Eppley et al.*, 1969b]. The parameters μ_{max} and K_s are highly variable between phytoplankton groups, and may span an order of magnitude under similar environmental (*i.e.,* temperature, salinity, depth) conditions [*Smayda*, 1997]. A typical range for μ_{max} is between 0.5 and 3.5 $\mathrm{d^{-1}}$, and K_s between 0.5 and 8 $\mathrm{mmol\,m^{-3}}$, with diatoms generally exhibiting a lower K_s than dinoflagellates [*e.g., Parsons et al.*, 1978; *Smayda*, 1997].

Depending on the phytoplankton community composition and the intensity and range of local NO_3 concentration, the Michaelis-Menten growth rate function (3.14) may be simplified [*Franks*, 2009]. If $NO_3 < K_s$ or if the the phytoplankton community is very diverse, then a linear uptake function (μ_V) may be equally useful for predicting μ, where μ_V is defined as

$$\mu_V = V NO_{3,mod} \tag{3.15}$$

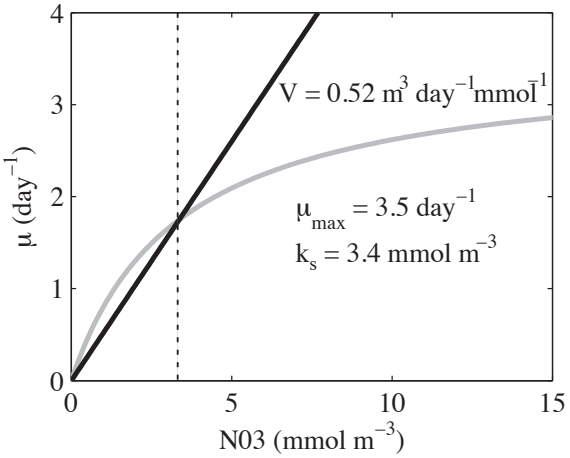

Figure 3.14: Growth rate (μ, d^{-1}) versus NO_3 ($mmol\,m^{-3}$) for linear uptake (V = 0.52 $m^3\,d^{-1}\,mmol^{-1}$, black line) and a Michaelis-Menten function (μ_{max} = 3.5 d^{-1}, $K_s = 3.4\,mmol\,m^{-3}$, gray line). 89% of the non-zero observed $NO_{3,T} < K_s$ (dashed vertical line), indicating that for the majority of the observed NO_3 concentrations (and according to these parameter choices), the Michaelis-Menten curve was roughly linear.

where $V = \mu_{max}/(2K_s)$ is chosen so that when $NO_3 = K_s$, $\mu_V = \mu_{MM}$. The non-zero (temperature-derived $NO_{3,T}$ were less than $K_s = 3.4\,mmol\,m^{-3}$, a nominal K_s for diatoms and dinoflagellates, 89% of the time (vertical dashed line, Fig. 3.14). Below this K_s threshold, μ_{MM} (gray line, Fig. 3.14) and μ_V (black line, Fig. 3.14) are similar. The more simple uptake function μ_V has an advantage of one fewer parameter over the more complex μ_{MM}, simplifying the task of model investigation and testing. Relatively little is known about *in situ* phytoplankton mortality rates m, and therefore, the simplest form for m, a constant, is chosen.

3.7.2 NP model-data comparison

Both functional forms μ_{MM} and μ_V were explored with the NP model to determine optimal parameter choices. The NP model was initialized with zero NO_3 and near-zero

P on day 1 of the $NO_3 flux_{tot}$ record and 8 days prior to the start of the Chl$a$ record. The 24-hr averaged observed $NO_3 flux_{tot}$ was used as a model input and the model was run for the 120 day record with 10-min time-steps. The modeled NO_3 and P were subsequently averaged back into 24 hr intervals. For model-data comparison, the observed Chl$a$ time-series (*e.g.,* Fig. 3.1) is assumed representative of the Chl$a$ in the entire euphotic layer and is converted to observed P via (3.11).

The NP model's ability to reproduce the observed P ($P^{(\mathrm{obs})}$) is investigated with the linear uptake function μ_V over a range of V and m parameters. The ability of $P^{(\mathrm{m})}$ to reproduce $P^{(\mathrm{obs})}$ (superscripts "(m)" and "(obs)" denote modeled and observed quantities, respectively) is quantified with skill $=1-\langle(P^{(\mathrm{m})}-P^{(\mathrm{obs})})^2\rangle/\langle(P^{(\mathrm{obs})})\rangle^2$, where $\langle\rangle$ represent a time-average of the 4-month record, and correlation r^2 (contours and colors in Fig. 3.15, respectively). The range in $V=\mu_{\max}/(2K_s)$ and m were chosen to encompass the maximum in both skill and r^2 (Fig. 3.15).

Both the NP model skill and r^2 have a single maxima ridge over a narrow V and m range. This ridge of high skill is tilted so that a larger mortality m is compensated by increased uptake V, *i.e.,* there is a trade-off between growth and mortality. The skill and r maxima overlap at V = 0.52 $\mathrm{m^3\,d^{-1}\,mmol^{-1}}$ (hence the choice of V in Fig. 3.14) and $m=0.55$ $\mathrm{d^{-1}}$ (see asterisk in Fig. 3.15) at $r^2=0.49$ and the skill of 0.61. The mean $NO_{3,\mathrm{T}}=0.73$ $\mathrm{mmol\,m^{-3}}$, yielding from (3.15) a mean growth rate $\mu=0.38$ $\mathrm{d^{-1}}$.

The tilt of the model skill contours (Fig. 3.15) also indicate stronger sensitivity to μ than to the mortality rate m. For example, the skill $=0.5$ contour spans a $\Delta\mu$ range of 0.18 $\mathrm{d^{-1}}$, when scaling the V axis by the mean $NO_{3,\mathrm{T}}$. In contrast, the model skill contours are elongated so that the skill $=0.5$ contour spans a $\Delta m=0.6$ $\mathrm{d^{-1}}$ range, much wider than the $\Delta\mu$ range. This result is encouraging because phytoplankton growth rates are much better understood and more easily parameterized than the mortality.

Using the linear μ_V and the best-fit V and m, the timing, magnitude and duration of the 3 observed blooms are generally well reproduced by the model (compare thin and thick green curves in Fig. 3.16a). For bloom 1, the $P^{(\mathrm{m})}$ peak overpredicts the observed

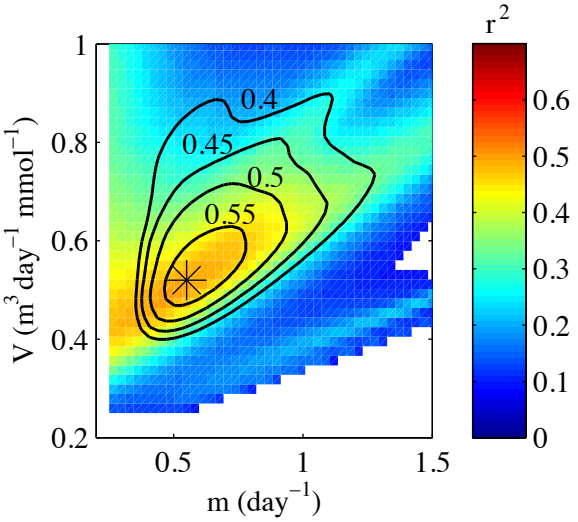

Figure 3.15: Correlation coefficient (r^2, colors) and model-data skill (contours) between $P^{(\mathrm{m})}$ and $P^{(\mathrm{obs})}$ over a range of the linear uptake parameter (V, $\mathrm{m^3\,d^{-1}\,mmol^{-1}}$) and mortality rate ($m$ $\mathrm{d^{-1}}$). The asterisk indicates the optimal choice of $V = 0.52$ $\mathrm{m^3\,d^{-1}\,mmol^{-1}}$ and $m = 0.55$ $\mathrm{d^{-1}}$ based upon the maximum correlation ($r^2 = 0.49$, $p < 0.001$) and skill (0.61).

$P^{(\mathrm{obs})}$ by approximately 50% and the timing of the model peak is a little early. The model reproduces the $\approx$ 15 day duration of bloom 1. For blooms 2 and 3, the model reproduces magnitude and timing of the P peaks, as well as the P reduction as the bloom decays. With bloom 2, the elevated $P^{(\mathrm{obs})}$ prior to the maximum is not well reproduced by the model. During non-bloom periods (*i.e.,* white background in Fig.3.16a), $P^{(\mathrm{m})}$ is usually near zero while $P^{(\mathrm{obs})}$ can be elevated, near 0.5 mmol m^{-3}. Similar, low background Chl a (or P) often are present in field records (*e.g.,* SIO pier Chl a, SCCOOS.org).

Several biological and physical factors are likely to be responsible for the differences between $P^{(\mathrm{m})}$ and $P^{(\mathrm{obs})}$. The NP model assumes constant V and m, which is not necessarily appropriate. In particular, if during non-bloom time-periods the phytoplankton community composition changes to phytoplankton with a different growth response, then the nitrate and Chl a dynamics will be different. The NO_3 flux is parameterized and may have noise. The NP model is driven only by new production and neglects the recycling of nutrients, whereas the observed Chl a reflects the total (new and recycled) production. The NP model neglects advection and spatial patchiness, and finally the "depth-averaged" $P^{(\mathrm{m})}$ prediction is compared to a point measurement of Chl a. Nevertheless, the fact that the model generally reproduces 3 independent bloom events being driven only by temperature and current based observations indicates that the $O(1)$ processes governing phytoplankton dynamics is being captured.

3.7.3 Modeling of individual blooms

Approximately half of the Chl a variability in the 4 month record was described by a 2 parameter NP model driven by the estimated vertical NO_3 flux. However, the model assumes that the phytoplankton community within each of the three bloom events have identical growth and mortality rates. Seasonal phytoplankton successions are frequently observed in the Southern California Bight between spring and fall, and a succession of dominant plankton communities among blooms also is likely at HB06. Different phyto-

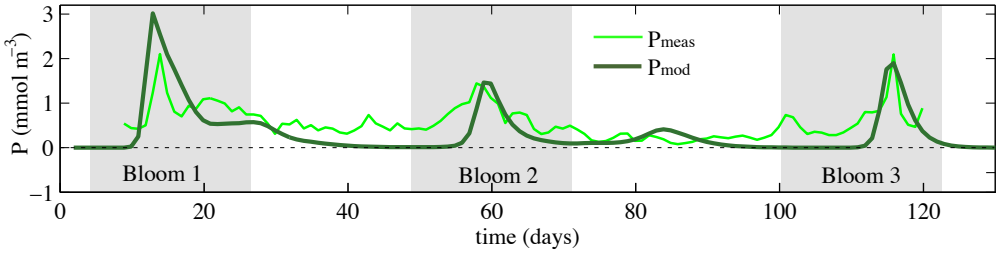

Figure 3.16: Timeseries of 24 h averaged $P^{(\mathrm{obs})}$ (mmol m^{-3}, light green line) and $P^{(\mathrm{m})}$ (mmol m^{-3}, dark green line). The gray shaded regions indicate the time periods of the 3 bloom events.

plankton communities will have different growth and mortality rates. Independent investigation of the optimal V and m parameters for each bloom provides some insight into the potential differences between these communities.

The $NO_3 flux_{tot}$ and P_{meas} estimates were divided into three segments (see gray shaded regions in Figs. 3.1 and 3.16), each encompassing an NO_3 flux and bloom event. For each bloom event, the model was run with a range of V and m for the full 4-month record with same initial conditions as described in Section 3.7.2. For each bloom, the model-data skill and correlation squared were calculated for the bloom event time period over a range of V and m. The skill and r^2 were not aligned (as in Fig. 3.15), and so the optimal V and m were selected at the maximum skill + r^2 (Fig. 3.17a-c). For each bloom, the individual optimizations improved both the skill and r^2 over that obtained from the entire timeseries (Table 3.2). The optimal m ranged between 0.4 and 0.84 d^{-1}, spanning the value 0.55 d^{-1} found for the entire timeseries fit. Optimal V for bloom 1 and 2 were similar (~ 0.6 m^3 d^{-1} mmol^{-1}), whereas V for bloom 3 was lower, at 0.31 m^3 d^{-1} mmol^{-1}. The model P timeseries with the best-fit V and m demonstrate that the timing, rise and declines of P (*i.e.,* Chl *a*) are well captured by the individual bloom fits (Fig. 3.17d). Very little is known about the mortality rates of phytoplankton, and the r^2 values indicate that a broad range of m will give a high correlation for all three blooms. However, analysis of V variations with each bloom may provide insight into the potential differences among these

Table 3.2: Dates of the timeseries segments selected for bloom modeling, optimal V ($m^3\,d^{-1}\,mmol^{-1}$), optimal m (d^{-1}), r^2 and skill for the optimal V and m. The optimal parameters were selected at the maximum of the sum of the model-data r^2 and skill.

	date	V	m	r^2	skill
Bloom 1	22 June to 22 July	0.59	0.84	0.58	0.68
Bloom 2	27 July to 31 Aug	0.65	0.40	0.62	0.70
Bloom 3	25 Sept to 18 Oct	0.31	0.70	0.53	0.72
All	18 June to 25 Oct	0.52	0.55	0.49	0.61

bloom communities. Only the range of r^2 where $p < 0.001$, and skill 0.6 is shown. This range does not extend below $V = 0.35\ m^3\,d^{-1}\,mmol^{-1}$ for blooms 1 or 2. During bloom 3, $r^2 > 0.5$ and skill is maximum near $V \approx 0.3\ m^3\,d^{-1}\,mmol^{-1}$, indicating that bloom 3 may have a different growth response to the NO_3 flux.

3.8 Discussion

3.8.1 Inferring bloom composition variation from uptake parameters

A year-long record (June 1972 - May 1973) of weekly phytoplankton counts and taxonomy taken from water samples off of a pier in 2.0 m water depth was reported by *Briand* [1976] at Seal Beach, CA (near Huntington Beach, CA) in an attempt to identify the community successions and seasonal variation of phytoplankton near Los Angeles. The dominant diatoms and dinoflagellates observed in the summer and fall were similar to those observed at HB06 (Table 3.1): predominantly *Lingulodinium*, *Ceratium*, *Prorocentrum*, *Asterionella*, and *Skeletonema* species. The maximum dinoflagellate concentration observed was 3.5×10^5 cells L^{-1} on 16 August 1972 during a red tide bloom of *L. polyedrum*. The bloom timescale and cell concentration are comparable to the bloom 3 observations, where the maximum *L. polyedrum* concentration was 3.9×10^4 cells L^{-1} on 12 October, 2006. *Briand* [1976] also observed a dominance of 80% diatoms during summer, with a shift to dinoflagellate (such as *L. polyedrum*) dominance during the fall. The observed seasonal

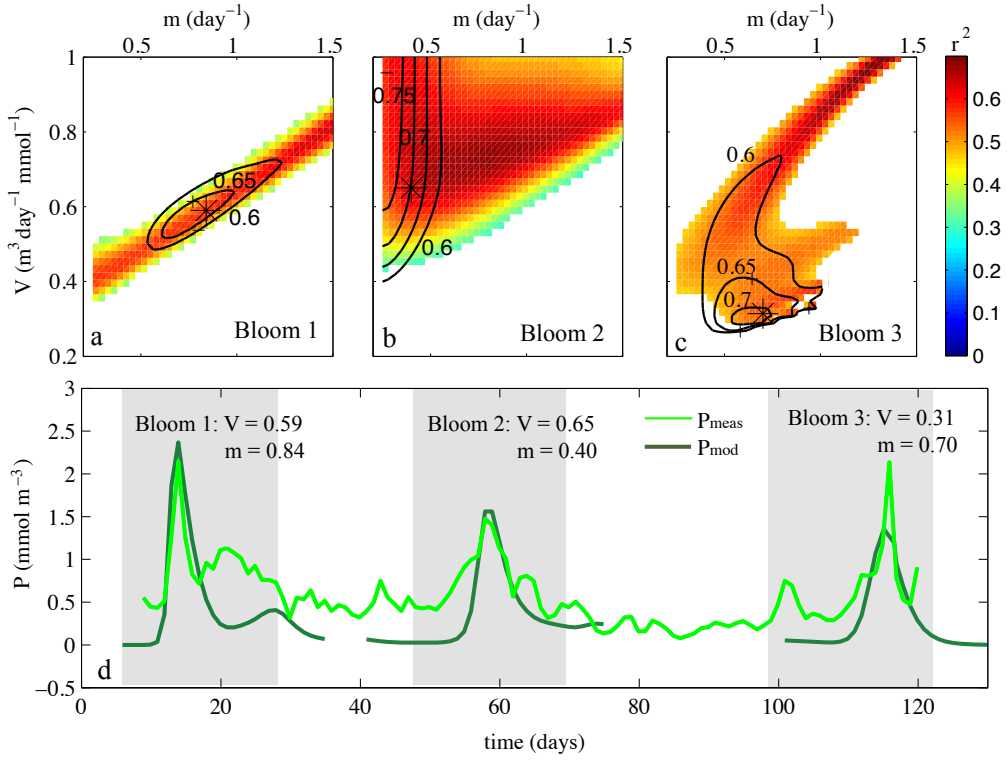

Figure 3.17: Panels (a) to (c): Correlation coefficient (r^2, colors) and model-data skill (contours) over a range of the linear uptake parameter (V, $\mathrm{m^3\,d^{-1}\,mmol^{-1}}$) and mortality rate ($m$, $\mathrm{d^{-1}}$) for each bloom event. The asterisk indicates the parameter pair chosen for each bloom based on the maximum correlation and skill. (d) 24 h averaged timeseries of $P^{(\mathrm{obs})}$ (thick green line) and (with the optimal parameters selected in panels (a) to (c)) $P^{(\mathrm{m})}$ for each of the blooms. The maximum correlation and skill for each bloom are listed in Table. 3.2.

phytoplankton succession at Seal Beach CA was consistent with the observed Southern California Bight progression of diatom domination during the spring (March-May) upwelling season, evolving to a combination of diatoms and dinoflagellates in summer and fall.

Diatoms in general have lower K_s than dinoflagellates. For example, *S. costatum* has a K_s of 0.4 to 3.6 mmol m^{-3} whereas *L. polyedrum* has a K_s of 5 to 8 mmol m^{-3} [*Eppley et al.*, 1969b]. Therefore, according to the scaling $V \propto K_s^{-1}$, diatom-dominated blooms will have a higher V than dinoflagellate blooms. Although the community composition of bloom 1 and 2 are not known, previous observations [*e.g., Briand*, 1976] and the apparently different optimal growth parameters indicate that blooms 1 and 2 may have been composed of a greater percentage of diatoms than the dinoflagellate-dominated bloom 3.

3.8.2 Mortality rates

Assuming that Chl a variations due to advection are small, the net growth rates ($\mu - m$) during the positive growth stages of each bloom may be inferred directly from logrithmic fits of measured Chl a (see Fig. 3.18). The net growth rate is highest during bloom 1 (0.57 d^{-1}) and lower during bloom 2 (0.17 d^{-1}) and 3 (0.22 d^{-1}). The actual growth rate μ of each bloom may be estimated by adding the optimal m obtained from the model for each bloom (Fig. 3.17) to the net growth rate, yielding μ of 1.41, 0.57, 0.92 d^{-1} for blooms 1 to 3, respectively. These growth rates are high compared to range anticipated from $\mu_V = V\mathrm{NO}_{3,T}$, and possibly reflect an overestimate in m during the positive growth phases of the blooms.

Although the NP model uses a constant m, the actual community m depends upon a variety of factors that are not constant with time (*e.g.,* nutrients, predators, light). For example, dinoflagellate m is related to the cell's ability to swim, counteracting their negatively buoyant cell bodies [*Cox*, 1980]. In nutrient-depleted conditions (potentially after the growth phase of a large bloom), swimming in cultures of *Lingulodinium polyedrum*

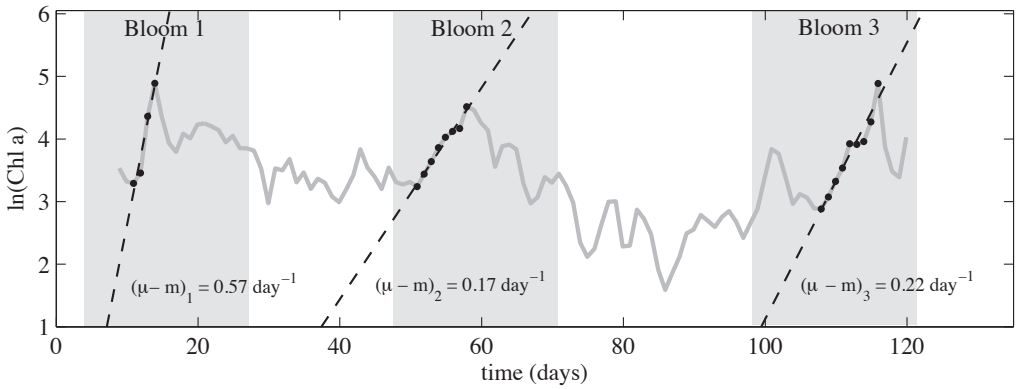

Figure 3.18: 24 h averaged timeseries of ln(Chl *a*) (gray line) with linear fits (black dashed lines) to the days (black points) with positive net growth ($(\mu - m) > 0$) during the three blooms.

becomes weak and cells sink at ≈ 6 m d^{-1} [*Holmes et al.*, 1967]. A sinking-dependent mortality (m_{sink}) could be scaled according to

$$m_{\text{sink}} = \frac{w_{\text{sink}}}{z_{\text{eu}}}, \tag{3.16}$$

where w_{sink} is the cell sinking speed and z_{eu} is the euphotic depth. With $w_{\text{sink}} = 6$ m d^{-1}, and $z_{\text{eu}} = -14$ m, $m_{\text{sink}} = -0.43$ d^{-1}, similar to model fit estimated $m = 0.40$ to 0.84 d^{-1}. This indicates that (at least for dinoflagellates) sinking during nutrient-depleted periods may constitute a large portion of the observed Chl *a* declines after blooms. For example, the *L. polyedrum*-dominated bloom 3 declined to pre-bloom Chl *a* levels within 2 days of the maximum on day 116 Chl *a* (Fig. 3.18). If the *L. polyedrum* all began sinking at 6 m d^{-1}, the disappearance of the entire bloom from the euphotic zone within 2 days is reasonable.

3.8.3 Other factors influencing phytoplankton blooms

The Chl$a$ rate of change reflects of the net growth rate of the local phytoplankton community, representing a bulk average of the individual cell growth rates of a diverse population. In the Southern California Bight, at first order the growth rate is controlled by NO_3 and may be inferred from parameters such as $\mu_{\max}$, K_s, V or m. However, these parameters vary among different phytoplankton species, and there are a variety of other environmental and physiological factors which may also have significant impacts.

For example, in addition to the role of turbulence-driven nutrient fluxes, small-scale turbulence influences phytoplankton growth and mortality. Motile dinoflagellates have the ability to combat enhanced sinking rates in low turbulence, and to cross isopycnals and access deeper nutrient pools in strongly stratified water [*Margalef*, 1978]. Conversely, in high turbulence, dinoflagellates may experience mechanical damage or gyrotactic disorientation [*Durham et al.*, 2009]. Reduced growth rates for *L. polyedrum* occur when the turbulent dissipation rate $\varepsilon > 2 \times 10^{-5}$ W kg^{-1} [*Thomas and Gibson*, 1990] and depend on the turbulence duration [*Juhl and Latz*, 2002]. However, these results are also not always reproduced. For *L. polyedrum* in the laboratory, an enhanced growth rate $\mu = 0.37$ d^{-1} was observed with stirring-induced ε of $O(10^{-4})$ W kg^{-1} relative to $\mu \approx 0.231$ d^{-1} during unstirred conditions [*Sullivan and Swift*, 2003]. Currently, investigation of the turbulence-growth rate relationship is restricted to laboratory studies, and extrapolation to *in situ* phytoplankton communities remains a challenge.

In addition, red tide-forming dinoflagellates (which represent 75% of HAB species) are particularly challenging to model with a simple nutrient-dependent growth function. These species possess complex life histories and unique physiological characteristics that may encourage the rapid formation of dense blooms despite their high K_s [*Smayda*, 1997]. For example, during nutrient-deplete conditions, many dinoflagellates form negatively buoyant cysts and remain dormant on the seafloor until environmental conditions improve. Motility may allow enhanced light exposure or access to deep nutrient pools, and many dinoflagellates produce allelochemicals that may enhance survival by inhibiting intraspe-

cific competition [*Guisande et al.*, 2002] and grazers [*Huntley*, 1982], implying a density dependant mortality. These traits encourage the ephemeral, often rapid, and opportunistic growth response, dense cell concentrations and sudden declines that are characterized by red tides, and may induce deviations from a simple NP model framework.

3.9 Summary

A 4-month long timeseries, spanning summer to fall (June-October) of Chl a was measured in $\approx$ 15 m water depth. During this time, 3 distinct Chl a blooms were observed. Each bloom lasted for approximately 10-20 days where 24-hr averaged Chl $a > 3\ \mu g L^{-1}$. Analysis of moored and boat-sampled observations collected in conjunction with the Chl a observations are used to understand the mechanisms driving the growth and decay of each bloom. During the experiment period, the overall stratification in $H = 18$ m depth was strong in June and decreased steadily throughout. The currents were dominated by unidirectional subtidal currents with the additional presence of by mode-1 diurnal and semidiurnal currents.

Although, a continuous nitrate observations are lacking, a temperature derived proxy for NO_3 is used in estimating the vertical flux of NO_3 into the euphotic zone. The vertical NO_3 flux is decomposed into two components: the advective and turbulent fluxes, where the advective flux is estimated from the vertical isotherm displacements and from the temperature-derived nitrate. This advective vertical NO_3 flux was only significant in the time period of the first bloom.

The turbulent vertical NO_3 flux requires a NO_3 diffusivity κ which is derived from both a IW-based and logarithmic BBL-based parameterizations. Each parameterizations require assumptions that are not totally accurate. These methods give κ that are correlated but the BBL κ is a factor of $4\times$ bigger than the IW-κ, as the BBl method neglects the effects of stratification that suppress turbulence. The resulting turbulent NO_3 flux estimate (based on the temperature-derived vertical NO_3 gradient) is elevated during 3 bloom time

periods. The total flux (advective+turbulent) has roughly equal contributions during the 1st bloom event, but is dominated by the turbulent flux at later times (blooms 2 and 3). A lagged-correlation between Chl$a$ and the total NO_3 flux was maximum when Chl$a$ lagged the estimated the NO_3 flux at 8 days, indicating that the vertical NO_3 flux was the dominant factor controlling the 3 blooms

The phytoplankton species composition, Chl$a$, and nutrients (NO_3, etc.) were bottle-sampled *in situ* during the time period of the 3rd bloom in October. This bloom (days 110-116) was mostly comprised of *L. polyedrum*. Although temporally and spatially aliased, the stages of bloom evolution were clearly observed from the bottle-sampled nutrients and Chl$a$. At first (day 100), Chl$a$ and NO_3 were low. Subsequently (day 108), NO_3 (and other nutrients) was elevated as it was fluxed into the euphotic zone while Chl$a$ remained low. Over the period of 3-7 days (days 109-116), phytoplankton (*L. polyedrum*) growth increased Chl$a$ and reduced NO_3. A few days after NO_3 was depleted, Chl$a$ began to decline as phytoplankton were consumed or sank from the euphotic zone.

Below the euphotic zone, the DSi:NO_3 and NO_3:PO_4 were consistent with Redfield ratios. In the euphotic zone during the bloom, the relative ratios of DSi:NO_3 departed significantly from Redfield as NO_3 was consumed whereas DSi was not, supporting the nutrient dynamics anticipated for dinoflagellate blooms. The euphotic zone NH_4:NO_3 ratio was slightly enhanced during the estimated flux event, and then became enhanced as NO_3 was depleted and NH_4 was produced through biological recycling during the bloom.

The estimated NO_3 flux is used to drive simple Nitrate-Phytoplankton (NP) model that neglects the effects of advection and spatial variability. Instead of using a more complex NO_3 uptake function, for the low range of observed NO_3, a linear uptake function works equally well. The resulting model has two parameters V and morality rate m that are explored, and revealed a maximum skill (and correlation) for $m = 0.55$ d^{-1} and $V = 0.52$ m^3 d^{-1} mmol^{-1}. With these parameters, the timing, duration, and (more or less) the magnitude of the 3 observed Chl$a$ blooms were reproduced using the only estimated vertical NO_3 flux to force the model.

Optimizing the model parameters over each bloom event, showed that the uptake parameter V differed between blooms 1 and 2 ($V \approx 0.6$ $m^3\,d^{-1}\,mmol^{-1}$) and bloom 3 $V = 0.31$ $m^3\,d^{-1}\,mmol^{-1}$. As dinoflagellates typically have lower V than diatoms, this suggests that bloom 1 and 2 may have been diatom dominated, whereas bloom 3 was *in situ* observed to be dinoflagellate dominated. This trend also consistent with the typical progression of the species that dominate in phytoplankton blooms from spring/summer to fall.

Vertical NO_3 flux into the euphotic zone is the sum of the advected ($NO_3 flux_{adv}$) and turbulent ($NO_3 flux_{mix}$) components, and depends on 4 locally-measured or estimated factors: 1) the NO_3 concentration, 2) the NO_3 gradient, 3) the vertical isotherm displacements, and 4) the vertical eddy diffusivity. We have shown that all are critical in governing the total vertical flux, but the relative importance of these factors may change over time. For example, if only $NO_3 flux_{adv}$ was estimated (as would be predicted if $NO_{3,T}$ were used as an index of available NO_3), only bloom 1 would be explained. We have shown that the turbulent NO_3 is also important, and for bloom 2 and 3, was the dominant NO_3 source. Because $NO_3 flux_{mix}$ is uncorrelated with T, this observation may help to explain the lack of correlation between nearshore Chl a and T [*Kim et al.*, 2009; *Santoro et al.*, 2010]. The success of a very simple 2 parameter NP model in reproducing the fundamental features of all three blooms (when both $NO_3 flux_{adv}$ and $NO_3 flux_{mix}$ are included) highlights the strong connection between the fluxes and the lagged Chl a response, and may assist the design of future nearshore programs identify the critical physical parameters and timescales to gain a potentially predictive insight into bloom dynamics in Southern California.

Bibliography

Agrawal, Y. C., E. A. Terray, M. A. Donelan, P. A. Hwang, A. J. Williams, W. M. Drennan, K. K. Kahma, and S. A. Kitaigorodskii, Enhanced dissipation of kinetic-energy beneath surface-waves, *Nature*, *359*(6392), 219–220, 1992.

Alonso-Rodrgueza, R., and F. Pez-Osuna, Nutrients, phytoplankton and harmful algal blooms in shrimp ponds: a review with special reference to the situation in the Gulf of California, *Aquaculture*, *219*, 317–336, 2003.

Anderson, D., Turning back the harmful red tide, *Nature*, *388*, 513–514, 1997.

Armstrong, F., and J. Strickland, Delineation of an upwelling patch using the autoanalyzer, *Annual Progress Report University of California Institute of Marine Resources*, pp. 55–58, 1965.

Backer, L., et al., Recreational exposure to aerosolized brevetoxins during florida red tide events, *Harmful Algae*, *2*, 19–28, 2003.

Beach, R., and R. Sternberg, Suspended-sediment transport in the surf zone: Response to breaking waves, *Continental Shelf Research*, *16*, 1989–2003, 1996.

Boehm, A., S. Grant, J. Kim, L. Mowbray, C. Mcgee, C. Clark, D. Foley, and D. Wellman, Decadal and shorter period variability of surf zone water at Huntington Beach, California, *Environmental Science and Technology*, *36*(18), 3885–3892, 2002.

Bretherton, F. P., R. Davis, and F. C.B., A technique for objective analysis and design of oceanographic experiments applied to mode-73, *Deep Sea Research*, *23*, 559–582, 1976.

Briand, F., Seasonal variations and assosciations of Southern Californian nearshore phytoplankton, *Journal of Ecology*, *64*(3), 821–, 1976.

Bricelj, V. M., J. Lee, A. Cembella, and D. M. Anderson, Uptake kinetics of paralytic shellfish toxins from the dinoflagellate Alexandrium fundyense in the mussel Mytilus edulis, *Mar. Ecol. Prog. Ser.*, *63*, 177–188, 1990.

Buskey, E., Behavioral components of feeding selectivity of the heterotrophic dinoflagellate protoperidinium pellucidum, *Mar. Ecol. Prog. Ser.*, *153*, 77–89, 1997.

Chavez, F. P., Forcing and biological impact of onset of the 1992 el nio in Central California, *Geophys. Res. Let.*, *23*(3), 265–268, doi:10.1029/96GL00017, 1996.

Clark, D. B., F. Feddersen, M. Omand, and R. T. Guza, Measuring fluorescent dye in the bubbly and sediment laden surfzone, *Water, Air and Soil Polution*, *204*, 103–115, doi:10.1007/s11270-009-0030-z, 2010.

Cloern, J., and R. Dufford, Phytoplankton community ecology: Principles applied in San Francisco Bay, *Mar. Ecol. Prog. Ser.*, *285*, 11–28, 2005.

Cloern, J., C. Grenz, and L. Vidergar-Lucas, An empirical model of the phytoplankton chlorophyll: Carbon ratio-the conversion factor between productivity and growth rate, *Limnol. Oceangr.*, *40*(7), 1313–1321, 1995.

Conversi, A., and J. McGowan, Natural versus human-caused variability of water clarity in the Southern California Bight, *Limnol. Oceangr.*, *1*, 632–648, 39.

Cox, E., Phytoflagellates, *Elsevier/North-Holland, New York.*, 1980.

Csanady, G., Turbulent diffusion in the environment, *D. Reidel, New York*, 1973.

Csanady, G. T., The free surface turbulent shear layer, *J. Phys. Oceanogr.*, *14*(2), 402–411, 1984.

Cullen, J., E. Stewart, R. Renger, and C. Winant, Vertical motion of the thermocline, nitracline and chlorophyll maximum layers in relation to currents on the Southern California shelf, *J. Mar. Res.*, *41*(2), 239–262, 1983.

Deane, G., and M. Stokes, Air entrainment processes and bubble size distributions in the surf zone, *J. Phys. Oceanogr.*, *29*, 1393–1403, 1999a.

Deane, G., and M. Stokes, Air entrainment processes and bubble size distributions in the surf zone, *J. Phys. Oceanogr.*, *29*(7), 1393–1403, 1999b.

Denman, K. L., and T. M. Powell, Effects of physical processes on planktonic ecosystems in the coastal ocean, *Oceanography and Marine Biology : An Annual Review*, *22*, 125–168, 1984.

Dewey, R. K., and W. R. Crawford, A microstructure instrument for profiling oceanic turbulence in coastal bottom boundary layers, *J. Atmos. and Ocean. Tech.*, *4*(2), 288297, 1987.

Dortch, Q., The interaction between ammonium and nitrate uptake in phytoplankton, *Mar. Ecol. Prog. Ser.*, *61*, 183–201, 1990.

Dubinsky, Z., P. Falkowski, and K. Wyman, Light harvesting and utilization by phytoplankton, *Plant and Cell Physiology*, *27*(7), 1335–1349, 1984.

Dugdale, R., C. Davis, and F. Wilkerson, Assessment of new production at the upwelling center at Point Conception, California, using nitrate estimated from remotely sensed sea surface temperature, *J. Geophys. Res.*, *102*(C4), 8573–8585, 1997.

Durham, W., J. Kessler, and R. Stocker, Disruption of vertical motility by shear triggers formation of thin phytoplankton layers, *Science*, *323*(5917), 1067–1070, 2009.

Eppley, R., and B. Petersen, Particulate organic matter flux and planktonic new production in the deep ocean, *Nature*, *282*, 677–680, 1979.

Eppley, R., J. Coatsworth, and L. Solorzano, Studies of nitrate reductase in marine phytoplankton, *Limnol. Oceangr.*, *14*, 194–205, 1969a.

Eppley, R., E. Renger, and W. Harrison, Nitrate and phytoplankton production in Southern California coastal waters, *Limnol. Oceangr.*, *23*(3), 483–494, 1979.

Eppley, R. W., J. N. Rogers, and J. J. McCarthy, Half-saturation constants for uptake of nitrate and ammonium by marine phytoplankton, *Limnol. Oceangr.*, *14*, 912–920, 1969b.

Falkowski, P., and D. Kiefer, Chlorophyll-a fluorescence in phytoplankton: relationship to photosynthesis and biomass, *Journal of Plankton Research*, *7*, 715–731, 1985.

Falkowski, P., and J. Raven, Aquatic photosynthesis, *Blackwell Science*, 1997.

Franks, P., Sink or swim: Accumulation of biomass at fronts, *Mar. Ecol. Prog. Ser.*, *82*, 1–12, 1992.

Franks, P., Spatial patterns in dense algal blooms, *Limnol. Oceangr.*, *4*, 1297–1305, 1997.

Franks, P., Planktonic ecosystem models: perplexing parameterizations and a failure to fail, *J. Plankton Res.*, *31*(11), 1299–1306, 2009.

Gill, A., *Atmosphere-Ocean Dynamics*, Academic Press, New York, 1982.

Grant, S. B., et al., Generation of enterococci bacteria in a coastal saltwater marsh and its impact on surf zone water quality, *Environmental Science and Technology*, *35*, 2407–2416, 2001.

Grant, W., A. Williams III, and S. M. Glenn, Bottom stress estimates and their prediction on the Northern California continental shelf during CODE-1: The importance of wave-current interaction, *J. Phys. Oceanogr.*, *14*(3), 506–527, 1984.

Grant, W. D., and O. S. Madsen, Combined wave and current interaction with a rough bottom, *J. Geophys. Res.*, *84*(C4), 1797–1808, 1979.

Gregg, M., Scaling turbulent dissipation in the thermocline, *J. Geophys. Res.*, *94*, 9686–9698, 1989.

Guisande, C., M. Frangpulos, I. Maneiro, A. Vergara, and I. Riveiro, Ecological advantages of toxin production by the dinoflagellate alexandrium minutum under phosphorus limitation, *Mar. Ecol. Prog. Ser.*, *225*, 169–176, 2002.

Haury, L., and E. Shulenberger, Surface nutrient enrichment in the California Current off Southern California: Description and possible causes, *Deep Sea Research Part II: Topical Studies in Oceanography*, *45*(8-9), 1577 – 1601, doi:10.1016/S0967-0645(98)80007-6, 1998.

Hayward, T., and E. Venrick, Nearsurface pattern in the california current: coupling between physical and biological structure, *Deep Sea Research Part II: Topical Studies in Oceanography*, *45*(8-9), 1617–1638, 1998.

Helfrich, K., Internal solitary wave breaking and run-up on a uniform slope, *Journal of Fluid Mechanics*, *242*, 1333–1543, 1992.

Henhey, F., J. Wright, and S. Flatte, Energetics of bore-like internal waves, *J. Geophys. Res.*, *102*, 3323–3330, 1986.

Hodges, B., On the distribution of oceanic chlorophyll, *Phd Dissertation*, 2006.

Holmes, R., The secchi disk in turbid coastal waters, *Limnol. Oceangr.*, *15*, 688–694, 1970.

Holmes, R. W., P. M. Williams, and R. W. Eppley, Red water in La Jolla Bay, 1964-1966, *Limnol. Oceangr.*, *12*(3), 503–512, 1967.

Horner, R., D. Garrison, and F. Plumley, Harmful algal blooms and red tide problems on the u.s. west coast, *Limnol. Oceangr.*, *42*(5), 1076–1088, 1997.

Huntley, M., Yellow water in La Jolla Bay, California, July 1980. II. Suppression of zooplankton grazing, *Journal of Experimental Marine Biology and Ecology*, *63*(1), 81–91, 1982.

Huyer, A., Coastal upwelling in the California current system, *Progress In Oceanography*, *12*(3), 259 – 284, doi:10.1016/0079-6611(83)90010-1, 1983.

Jeong, Y., B. Sanders, K. McLaughlin, and G. S. B., Treatment of dry weather urban runoff in tidal saltwater marshes: A longitudinal study of the talbert marsh in Southern California, *Environmental Science and Technology*, pp. 3609–3614, 42.

Johnson, A., D. R. Weidemann, and W. S. Pegau, Internal tidal bores and bottom nepheloid layers, *Continental Shelf Research*, *21*, 1473–1484, 2001.

Juhl, A., and M. Latz, Mechanisms of fluid-shear-induced inhibition of population growth in a red-tide dinoflagellate, *Journal of Phycology*, *38*, 683–694, 2002.

Kamykowski, D., Possible interactions between phytoplankton and semidiurnal tides, *J. Mar. Res.*, *32*, 67–89, 1974.

Keifer, D., Chlorophyll a fluorescence in marine centric diatoms: Responses of chloroplasts to light and nutrient stress, *Marine Biology*, *23*, 1432–1793, 1973.

Kim, H., A. Miller, J. McGowan, and M. Carter, Coastal phytoplankton blooms in the Southern California Bight, *Progress In Oceanography*, *82*(2), 137–147, 2009.

Kudela, R., and W. Cochlan, Nitrogen and carbon uptake kinetics and the influence of irradiance for a red tide bloom off southern california, *Aquatic Microbial Ecology*, *21*, 31–47, 2000.

Lamb, K., Particle transport by non-breaking, solitary internal waves, *J. Geophys. Res.*, *102*, 18,641–18,660, 1997a.

Lamb, K., A numerical investigation of solitary internal waves with trapped cores formed via shoaling, *Journal of Fluid Mechanics*, *451*, 109–144, 1997b.

Legaard, K., and A. Thomas, Spatial patterns of intraannual variability of chlorophyll and sea surface temperature in the California Current, *J. Geophys. Res.*, *111*, doi: 10.1029/2005JC003282, 2006.

Legaard, K., and A. Thomas, Spatial patterns of intraseasonal variability of chlorophyll and sea surface temperature in the California Current, *J. Geophys. Res.*, *112*, doi: 10.1029/2007JC004097, 2007.

Lennert-Cody, C., and P. Franks, Plankton patchiness in high-frequency internal waves, *Mar. Ecol. Prog. Ser.*, *186*, 59–66, 1999.

Lennert-Cody, C., and P. Franks, Fluorescence patches in high-frequency internal waves, *Mar. Ecol. Prog. Ser.*, *235*, 29–42, 2002.

Lerczak, J., Internal waves on the Southern California coast. phd dissertation,, *Phd dissertation, University of California, San Diego.*, 2000.

Lerczak, J., M. Hendershott, and C. Winant, Observations and modeling of coastal internal waves driven by a diurnal sea breeze, *J. Geophys. Res.*, *106*(C9), 19,71519,730, 2001.

Lewis, J., and R. Hallett, Lingulodinium polyedrum Gonyaulax polyedra. a blooming dinoflagellate, *Oceanography Marine Biology Annual Review*, *35*, 97–161, 1997.

Longuet-Higgins, M., Longshore currents generated by obliquely incident sea waves, *J. Geophys. Res.*, *75*(33), 6778–6789, 1970.

Lucas, A., The physical control of phytoplankton dynamics over the Southern California Bight continental shelf, *Phd. Thesis, University of California San Diego*, 2009.

Lucas, A., C. Dupont, V. Tai, J. Largier, B. Palenik, and P. Franks, The green ribbon: Multi-scale physical control of phytoplankton productivity and community structure over a narrow continental shelf, *Limnol. Oceangr.*, in press, 2011.

Mackinnon, J. A., and M. C. Gregg, Mixing on the late-summer New England Shelf - solibores, shear, and stratification, *J. Phys. Oceanogr.*, *33*, 1476–1492, 2003.

Mackinnon, J. A., and M. C. Gregg, Spring mixing: Turbulence and internal waves during restratification on the New England Shelf, *J. Phys. Oceanogr.*, *35*(12), 2425–2443, 2005.

Mahoney, J., and J. E. Steml, A mass mortality of marine animals associated with a bloom of ceratium tripos in the New York Bight, *In Toxic Dinoflagellate Blooms: Proceedings of the 2nd International Conference. London: Elsevier*, 1979.

Margalef, R., Life-forms of phytoplankton as survival alternatives in an unstable environment, *Oceanologica Acta*, *1*(4), 493–509, 1978.

Mayali, X., P. Franks, Y. Tanaka, and F. Azam, Bacteria-induced motility reduction in lingulodinium polyedrum dinophyceae, *Journal of Phycology*, *44*, 923–928, 2008.

McManus, M. A., R. Kudela, M. Silver, G. Steward, and J. Sullivan, Cryptic blooms: Are thin layers the missing connection?, *Estuaries and Coasts*, *312*, doi:10.1007/s12237-007-9025-4, 2008.

Michaelis, L., and M. Menten, Die kinetik der invertinwirkung, *Biochem. Z.*, *49*, 333–369, 1913.

Muller, P., X. Li, and K. Niyogi, Non-photochemical quenching. a response to excess light energy, *Plant Physiology*, *125*, 1558–1566, 2001.

Nam, S., and U. Send, Sea/land breeze-driven diurnal oscillations in the coastal southern california bight, *Geophysical Research Letters*, in press, 2011.

Noble, M. A., B. Jones, P. Hamilton, J. Xu, G. Robertson, L. Rosenfeld, and J. Largier, Cross-shore transport into nearshore waters due to shoaling internal tides in San Pedro Bay, CA, *Continental Shelf Research*, doi:10.1016/j.csr.2009.04.008, 2009.

Olivieri, R., and F. Chavez, A model of plankton dynamics for the coastal upwelling system of Monterey Bay, California, *Deep-sea research. Part 1. Oceanographic research papers*, *47*(5), 1077–1106, 2000.

Omand, M. M., J. J. Leichter, P. J. S. Franks, A. J. Lucas, R. T. Guza, and F. Feddersen, Physical and biological processes underlying the sudden appearance of a red-tide surface patch in the nearshore, *Limnol. Oceangr.*, in press, 2011.

Osborn, T., Estimates of the local rate of vertical diffusion from dissipation measurements, *J. Phys. Oceanogr.*, *10*, 83–89, 1980.

Parsons, T., P. Harrison, and R. Waters, An experimental simulation of changes in diatom and dinoflagellate blooms, *Journal of Experimental Marine Biology and Ecology*, *32*(3), 285–294, 1978.

Pfister, C., J. Wootton, and C. Neufeld, Relative roles of coastal and oceanic processes in determining physical and chemical characteristics of an intensely sampled nearshore system, *Limnol. Oceangr.*, *52*(5), 1767–1775, 2007.

Rainville, L., and R. Pinkel, Wirewalker: An autonomous wave-powered vertical profiler, *J. Atmos. and Ocean. Tech.*, *18*(6), 1048–1051, 2001.

Redfield, A., The biological control of chemical factors in the environment, *American Scientist*, *46*(3), 206–226, 1958.

Reeves, R., S. Grant, R. Mrse, C. Copil Oancea, B. Sanders, and A. Boehm, Scaling and management of fecal indicator bacteria in runoff from a coastal urban watershed in Southern California, *Environmental Science and Technology*, *38*(9), 26372648, 2004.

Santoro, A., N. Nidzieko, G. van Dijken, K. Arrigo, and A. Boehm, Contrasting spring and summer phytoplankton dynamics in the nearshore Southern California Bight, *Limnol. Oceangr.*, *55*(1), 264–278, 2010.

Sayce, K., and R. Horner, Pseudo-nitzschia spp. in willapa bay, washington, 1992 and 1993, *In Harmful and toxic algal blooms. Proc. 7th Int. Conf. on Toxic Phytoplankton. Intergov. Oceanogr. Comm. UNESCO*, 1996.

Sharples, J., C. M. Moore, and E. R. Abraham, Internal tide dissipation, mixing, and vertical nitrate flux at the shelf edge of NE New Zealand, *J. Geophys. Res.*, *106*(C7), 14,069–14,081, 2001.

Shaw, W., Mechanisms of turbulent mixing in the continental shelf bottom boundary layer, *Phd. Thesis, MIT and WHOI*, 1999.

Smart, P., and I. Laidlaw, Evaluation of some fluorescent dyes for water tracing, *Water Resource Research*, *13*, 15–33, 1977.

Smayda, T. J., Harmful algal blooms: Their ecophysiology and general relevance to phytoplankton blooms in the sea, *Limnol. Oceangr.*, *42*(5), 1137–1153, 1997.

Souza, A. J., and J. Pineda, Tidal mixing modulation of sea-surface temperature and diatom abundance in Southern California, *Continental Shelf Research*, *21*(6-7), 651 – 666, doi:10.1016/S0278-4343(00)00105-9, 2001.

Stramski, D., E. Boss, D. Bogucki, and J. Voss, The role of seawater constituents in light backscattering in the ocean, *Progress in Oceanography*, *61*, 27–56, 2004.

Sullivan, J., and E. Swift, Effects of small-scale turbulence on net growth rate and size of ten species of marine dinoflagellates, *Journal of Phycology*, *39*, 83–94, 2003.

Sverdrup, H., and M. Johnson, *Oceans*, New Jersey; Prentice-Hall, 1942.

Tennekes, H., and J. L. Lumley, *A First Course in Turbulence*, MIT Press, 1972.

Terrill, E. J., W. K. Melville, and D. Stramski, Bubble entrainment by breaking waves and their influence on optical scattering in the upper ocean, *J. Geophys. Res.*, doi: 106:1681516823, 2001.

Tester, P. A., and B. Mahoney, Implication of the diatom, Chaetoceros convolutus, in the death of red king crabs, Paralithodes camtschatica, Captains Bay, Unalaska Island, alaska, *In Harmful Marine Algal Blooms*, *1*, XX–YY, 1995.

Thomas, W., and C. Gibson, Quantified small-scale turbulence inhibits a red tide dinoflagellate, *Gonyaulax polyedra* [stein], *Deep Sea Research Part A. Oceanographic Research Papers*, *37*(10), 1583–1593, 1990.

Todd, R. E., D. Rudnick, and R. Davis, Monitoring the greater san pedro bay region using autonomous underwater gliders during fall of 2006, *J. Geophys. Res.*, *114*, doi: 10.1029/2008JC005086, 2009.

Traganza, E. D., D. G. Redalije, and R. W. Garwood, Chemical flux, mixed layer entrainment and phytoplankton blooms at upwelling fronts in the california coastal zone, *Continental Shelf Research*, *7*(1), 89 – 105, doi:10.1016/0278-4343(87)90066-5, 1987.

Turner, R., N. Qureshi, N. Rabalais, Q. Dortch, D. Justic, R. Shaw, and J. Cope, Fluctuating silicate:nitrate ratios and coastal plankton food webs, *Proceedings of the National Academy of Science*, *95*(22), 13,048–13,051, 1998.

Wang, P., B. Ebersole, E. Smith, and B. Johnson, Temporal and spatial variations of surfzone currents and suspended sediment concentration, *Coastal Engineering*, *46*, 175–211, 2002.

Winant, C., The vertical structure of coastal currents, *Deep Sea Research*, *23*, 925–936, 1974.

Winant, C., and J. Olsen, Internal surges in coastal waters, *J. Geophys. Res.*, *79*, 4523–4526, 1976.

Yu, Y., R. Sternberg, and R. Beach, Kinematics of breaking waves and associated suspended sediment in the nearshore zone, *Continental Shelf research*, *13*, 1219–1242, 1993.

Zaneveld, J., R. Spinrad, and R. Bartz, Optical properties of turbidity standards., *SPIE 208*, 1979.